Lappeenranta
University of Technology

Marko Rilla

DESIGN OF SALIENT POLE PM SYNCHRONOUS MACHINES FOR A VEHICLE TRACTION APPLICATION – ANALYSIS AND IMPLEMENTATION

Thesis for the degree of Doctor of Science (Technology) to be presented with
due permission for public examination and criticism in the Auditorium 1383
at Lappeenranta University of Technology, Lappeenranta, Finland on
the 8th of December, 2012, at noon.

Acta Universitatis
Lappeenrantaensis 497

Supervisor Professor Juha Pyrhönen
Department of Electrical Engineering
Institute of Energy Technology
Lappeenranta University of Technology
Lappeenranta, Finland

Reviewers Associate Professor Pavol Rafajdus
University of Žilina
Slovak Republic

D.Sc., Adjunct Professor Janne Väänänen
The Berggren Group
Helsinki, Finland

Opponent Associate Professor Pavol Rafajdus
University of Žilina
Slovak Republic

D.Sc., Adjunct Professor Janne Väänänen
The Berggren Group
Helsinki, Finland

ISBN 978-952-265-336-9
ISBN 978-952-265-337-6 (PDF)
ISSN 1456-4491

Lappeenrannan teknillinen yliopisto
Yliopistopaino 2012

Abstract

Marko Rilla

Design of salient pole PM synchronous machines for a vehicle traction application – Analysis and Implementation

Lappeenranta 2012

157 p.

Acta Universitatis Lappeenrantaensis 497

Diss. Lappeenranta University of Technology

ISBN 978-952-265-336-9, ISBN 978-952-265-337-6 (PDF), ISSN 1456-4491

This doctoral thesis presents a study on the development of a liquid-cooled frame salient pole permanent-magnet-exited traction machine for a four-wheel-driven electric car. The emphasis of the thesis is put on a radial flux machine design in order to achieve a light-weight machine structure for traction applications. The design features combine electromagnetic and thermal design methods, because traction machine operation does not have a strict operating point. Arbitrary load cycles and the flexible supply require special attention in the design process.

It is shown that accurate modelling of the machine magnetic state is essential for high-performance operation. The saturation effect related to the cross-saturation has to be taken carefully into account in order to achieve the desired operation.

Two prototype machines have been designed and built for testing: one totally enclosed machine with a special magnet module pole arrangement and another through-ventilated machine with a more traditional embedded magnet structure. Both structures are built with magnetically salient structures in order to increase the torque production capability with the reluctance torque component. Both machine structures show potential for traction usage. However, the traditional embedded magnet design turns out to be mechanically the more secure one of these two machine options.

Keywords: Permanent magnet synchronous motor, radial flux, PMSM, salient pole, traction, thermal analysis.

UDC 621.313/.333:629.028

Acknowledgements

The preparation for the doctoral dissertation started in August 2006 right after the Masters degree in Electrical engineering. The actual work for the dissertation was carried out during 2009 – 2012. I would like to thank Professor Juha Pyrhönen, and Sami Ruotsalainen of Metropolia University of applied sciences for the possibility to work with such a leading edge topic in electrical engineering.

I would like to express my gratitude to Doctors Janne Nerg and Markku Niemelä. Nergs advices in scientific methods during the years and his contribution in the development of the prototype machines is highly appreciated. The long-term guidance of Nerg and Niemelä, especially during this last candidate year, has made the completion of the thesis possible.

I also need to express my gratitude to Associate Professor Pavol Rafadjus and D.Sc Adjunct professor Janne Väänänen for the thorough pre-examination work and the valuable comments which have helped me to improve the scientific level of the dissertation.

Special thanks goes also to Jouni Ryhänen and Martti Lindh for the technical implementation of the test setups.

I'm also in gratitude to Hanna Nimelä for the proofreading of the thesis and the improvement of the English language to make the dissertation fluently readable.

I also appreciate the financial support of South–Karelian Fund of Finnish Cultural Foundation, Lauri and Lahja Hotinen Fund, Finnish Foundation for Technology Promotion and Research Foundation of Lappeenranta University of Technology during the candidate years.

I would also like to thank all the friends and colleagues that I have met along the years for the prolonged coffee breaks, late nights and early mornings☺.

And to my Family, Thank You for the support and understanding during the years.

Lappeenranta November 25, 2012

Marko Rilla

Contents

Abstract

Acknowledgements

Contents

Nomenclature

Nomenclature

Greek variables

α	coefficient
β	absorptivity
δ	air gap
ε_r	relative permittivity
ε	emissivity
η	efficiency
κ	coefficient
μ_r	relative permeability
ν	number of harmonic order
ρ	electrical resistivity [Ωm]
σ	electrical conductivity [S]
τ	pitch factor
ω	angular velocity [rad/s]
Ω	mechanical angular velocity [rad/s]
Φ	magnetic flux [Vs]
Θ	current linkage [A]
Ψ	magnetic flux linkage [Vs]
υ	specific loss
Γ	bearing load
ζ	constant friction coefficient

Roman variables

a	number of parallel branches
A	linear current density [A/m]
a_v	acceleration [m/s^2]
B	flux density [Vs/m^2]
b	breadth [m]
C	friction coefficient
d	depth [m]
D	diameter [m]
E	back electromotive voltage [V]
f	frequency [1/s]
h	height [m]
H	magnetic field strength [A/m]
I	current [A]
k	thermal conductivity [°C/W]
k_C	Carter coefficient
k_d	winding distribution factor
k_p	winding pitch factor
k_{sq}	winding skew factor
k_{w1}	winding factor of fundamental wave
L	inductance [H]
l	length [m]
m	mass [kg]
n	rotating speed [min^{-1}]
N_s	phase turn number
Nu	Nusselt number

p	pole number
P	power [W]
q	slots per pole and phase
Q	slot number
r	radius [m]
S	area [m^2]
T	torque [Nm]
U	voltage [V]
w	width [m]
z_Q	parallel conductors in a slot

Subscripts

eq	equivalent
δ	air gap
σ	leakage
avg	average
B	bearing
d	tooth
e	eddy current
f	fluid (convection)
Fe	iron
h	hysteresis
L	line
LL	line-to-line
m	magnetizing
max	maximum
n	nominal
p	pole
q	quadrature
r	radial, relative, rotor, relative
rr	rolling
s	stator
tan	tangential
u	slot
v	drag
w	wheel,winding
ins	insulation
impr	impregnation
w1	fundamental frequency

Acronyms

AC	alternating current
DC	direct current
EM	embedded manget
EMF	electromotive force
E-RA	Electric-Race About
ICE	Internal combustion engine
IEA	International Energy Agency
IM	Induction machine
MM	magnet module
p.u.	per unit

PM	permanent magnet
PWM	pulse width modulation
RC	radio controlled
RMS	Root-mean-square
SRM	Switched reluctance machine
SMC	Soft magnetic composite
SynRaPM	Synchronous-reluctance-assisted PM machine
SynRM	Synchronous reluctance machine
TE	totally enclosed

Natural constants

g	specific gravity ~9.81 [m/s^2]
π	relation of circle perimeter to diameter ~3.1416
ε_0	permittivity of vacuum ~ $8.854 \cdot 10^{-12}$ [F/m]
μ_0	permeability of vacuum ~$1.256 \cdot 10^{-6}$ [Vs/Am]

1 Introduction

Electromechanical energy conversion processes are among the key elements in the development of modern society. There are two kinds of primary energy sources: renewable and non-renewable. The majority of the current primary energy consumption is still satisfied with non-renewable energy sources. According to the International Energy Agency (IEA), 13.2 % of the total 12 717 Mtoe (1 Mtoe ≈ 42GJ ≈ 11.7 MWh) of primary energy supply was produced with renewable sources in 2010 (IEA, 2012). The renewable primary energy supply consists mainly of hydro energy and energy from combustible renewables and waste. The rest, 0.9 % units of the renewable primary energy supply, come from geothermal, wind, solar and similar energy sources. A comparison of the primary energy supply in 1973 and 2009 is presented in Fig. 1.1.

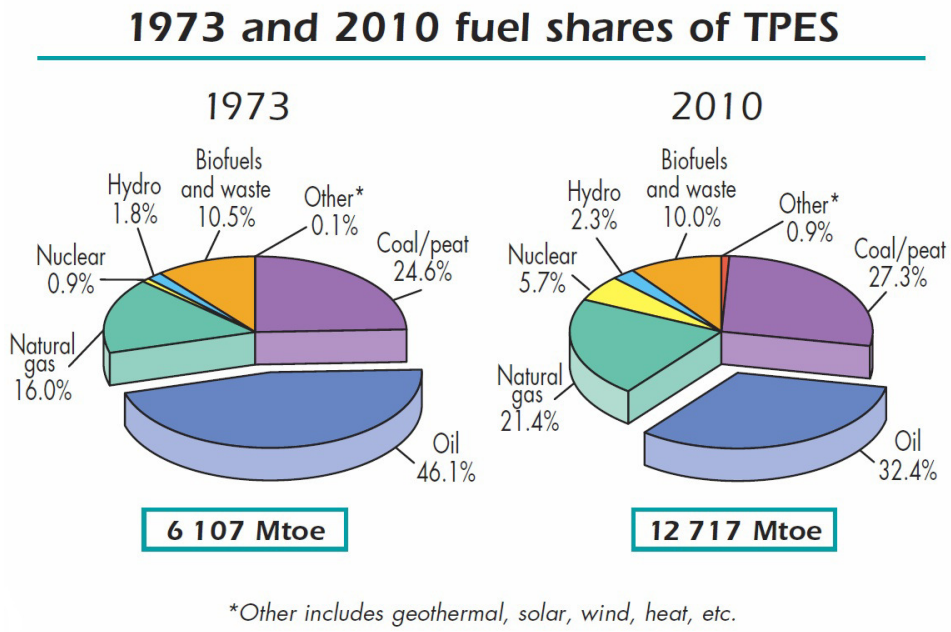

Fig. 1.1. World primary energy supply in 1973 and 2010 (IEA, 2012).

Globally, the estimated final energy consumption is about 8677 Mtoe, which is about 8677/12150 ≈ 68 % of the total primary energy supply. About 1536 Mtoe of this energy is consumed as electricity, of which the industry takes about 41.5 % and transportation only about 1.6 %. The rest is left for residential use, non-specific other use and commercial and public services. On the other hand, 3570 Mtoe of energy is consumed as oil, of which 61.5 % is consumed in transportation. As a result of the increasing oil price and awareness of environmental issues, the development of transportation systems is heading towards cleaner propulsion technologies with electrical machines in vehicles. The consumption of primary energy in transportation can be significantly reduced with electric traction systems, because the energy conversion efficiency is significantly higher in large power plants running at steady-state power compared with varying load cycle efficiencies of

individual internal combustion engines (ICE) in vehicles. In the case of hybrid drives, the ICE unit can be downsized and used in a more efficient way to significantly increase the overall performance. Thus, the research and development of electric traction machine technology is still highly important, even though it already has a history of more than hundred years. New technologies such as high energy product permanent magnets and efficient power electronics give rise to the development of electric traction systems.

Electrical machine drives make it possible to change the direction of energy conversion between electric energy and mechanical work, depending on the need. Electrical machine drives can be divided into several different categories according to the torque and speed range characteristics of the load. Some applications, such as conveyor belt systems and compressors, require constant torque output over the speed range. Pump and fan systems, on the other hand, require the torque output to be directly proportional to the second power of the rotating speed. Thirdly, there is a load type that requires a large breakaway torque and a constant torque range up to a certain base speed and a broad constant power range beyond this point. Load characteristics of this kind are typical for traction applications, such as high-speed gearless elevators, high-performance conveyors and mobile vehicles, which is the application field focused on in this thesis.

1.1 Objectives of the study

This doctoral thesis presents a study on the development of a liquid-cooled frame salient pole permanent-magnet-exited traction machine for a four-wheel-driven electric car in the Electric Race About (E-RA) project of Helsinki Metropolia University of Applied Sciences (later referred to as Metropolia).

Fig. 1.2. E-RA concept car of Helsinki Metropolia University of Applied Sciences (Metropolia, 2009).

The study concentrates on promoting a machine design for vehicle traction, the key features and advantages of which are light weight and high performance over a broad rotating speed range

within the boundaries of the given application. One of these is the direct drive principle, which is not very common in electric vehicles.

The key target of the machine design, besides the direct drive, is to achieve a light structure with an enhanced torque output capability with inherent saliency by a suitable pole design. The reluctance torque helps in the pull-out torque production and boosts the machine torque properties throughout the speed range. The main part of the torque is still produced by permanent magnet excitation. Hence, the machine is here designated as a synchronous, reluctance-torque-assisted permanent magnet (SynRaPM) machine in contrast to synchronous reluctance machines with an additional PM excitation. Further, the design process includes certain thermal endurance aspects. A thermal analysis is essential in these kinds of machine structures where the loss distribution is dominated by Joule losses.

The rated power of 25 kW per motor at a rotating speed of 1000 min^{-1} in constant operation was originally set as a basis for the machine design according to the known race car track data provided by Metropolia. The constant operation at 25 kW for the rotating speed of 1000 min^{-1} yields a torque of 240 Nm. The target set for the peak torque of the machine was 1000 Nm. The drive propulsion system consists of an accumulator connected to four three-phase inverter bridges with each one driving a PM traction motor connected to a wheel via a drive shaft. Thus, the combined continuous power of the traction system is 100 kW at 1000 min^{-1}. The motors are, however, also capable of producing 200 kW of combined continuous power at 2000 min^{-1} because of the low iron loss generation and improved cooling of the through-ventilated design. The accumulator package consists of two sets of 143 series-connected cells resulting in a 100 Ah capacity. The individual battery cell cut-off voltage as a function of cell charge is presented in Fig. 1.3.

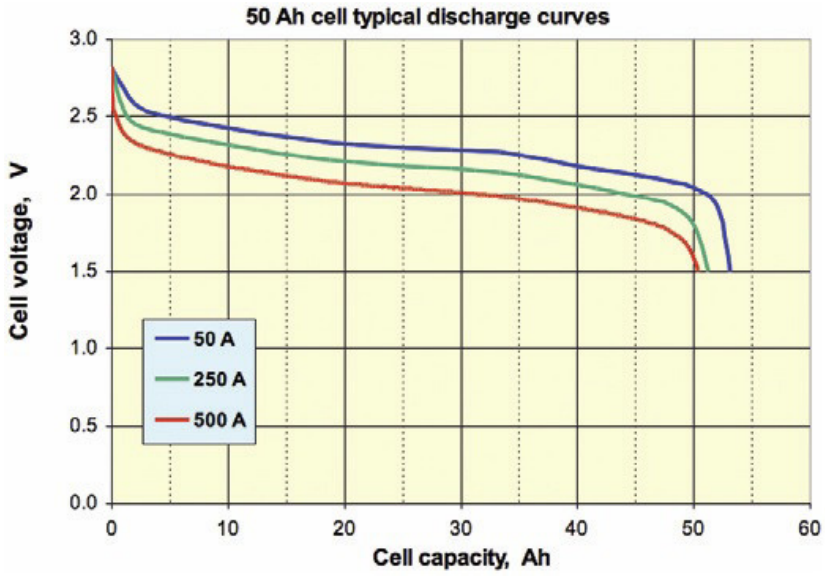

Fig. 1.3. Individual cell cut-off voltage levels of Altairnano 50 Ah Lithium titanate battery cell as a function of cell charge for charge currents of 50 A, 250 A and 500 A (Altairnano, 2009).

According to the manufacturer data presented in Fig. 1.3, the cell cut-off voltages are ~1.5 V_{DC} at the lower limit and ~2.9 V_{DC} at the upper limit. Thus, the battery package is capable of producing voltage levels between 143·1.5 V_{DC} = 214.5 V_{DC} and 143·2.9 V_{DC} = 414.7 V_{DC}. Before the 80 % depth of the discharge level is reached, the normal maximum operating voltage is around 374 V_{DC}, which leads to a maximum AC line-to-line voltage of 264 V_{RMS}. The cut-off line-to-line AC voltage level is 151.6 V_{RMS}. The available voltage is intended to be used at the top speed without entering deeply into the field weakening region. With this voltage level, the machine is capable of achieving a maximum speed of 2000 min^{-1} in normal operation, which allows top speeds beyond 200 km/h with a suitable wheel configuration. With the cut-off voltage, the motor can achieve 1150 min^{-1} without entering the field weakening region. Nevertheless, field weakening operation is mandatory at higher speeds, since the accumulator voltage drops with the increasing load current and the decreasing charge as presented in Fig. 1.3.

1.2 Traction machine for vehicle propulsion

Common for traction applications is the high torque requirement over a broad operating speed range. Traction applications usually require a torque to speed curve that resembles the curves presented in Fig 1.4.

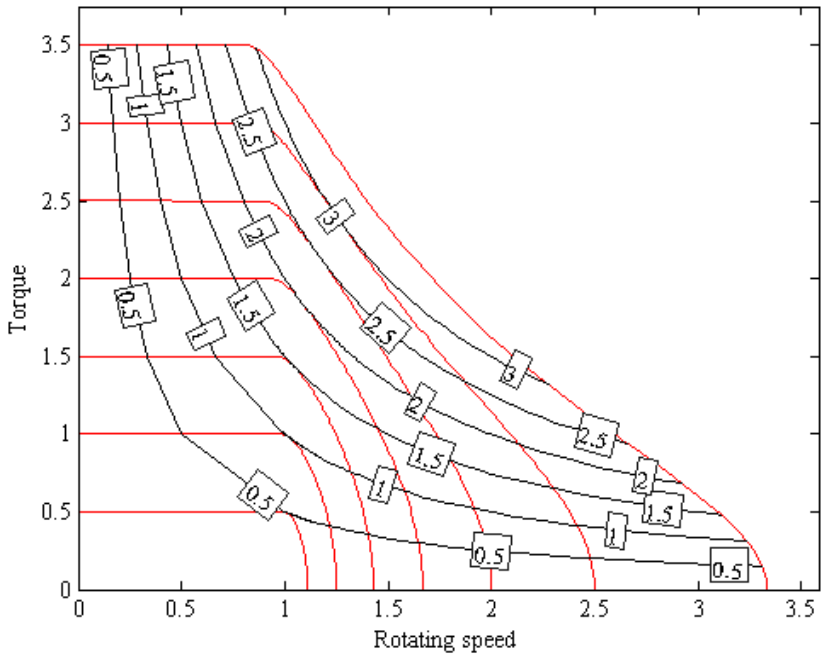

Fig. 1.4. Examples of per unit torque to speed curves of PMSMs (red) and per unit constant power curves (black) for traction applications. L_d=L_q=0.2 pu. The permanent magnet flux linkage is ψ_{PM}=1 p.u.

The requirements for electrical machine performance can be evaluated by comparing the acceleration force with the force required to maintain a constant operating speed. The torque acting on a wheel forms a force parallel to the surface. There are three forces acting against this force. They are rolling friction, air friction and the force required to alter the momentum. With no elevation taken into account, the force balance equation takes the form

$$\frac{T}{r_w} = ma + C_{\mathrm{rr}} mg + \frac{1}{2}\rho_{\mathrm{air}} v^2 S C_{\mathrm{v}} \qquad 1.1$$

where

- m is the total mass of the vehicle [kg],
- a is the acceleration [m/s^2],
- g the gravitational constant [m/s^2],
- ρ_{air} is the air density [kg/m^3],
- S is the vehicle cross-sectional area towards moving direction,
- C_{rr} is the rolling friction factor,
- C_{v} is the drag coefficient,
- T is the wheel torque [Nm],
- r_{w} is the wheel radius [m] and
- v is the velocity of the vehicle [m/s]

To maintain a constant speed, the machine wheel must produce torque equal to the drag and rolling friction. The desired acceleration rate determines the required maximum torque output.

With a practical example, the proportions of different drag types are easier to perceive. An average passenger car weighs about 1500 kg, and with a carrying capacity of 450 kg, the total mass equals 1950 kg. A typical drag coefficient is around 0.3 (varying between 0.2 and 0.6) and a typical rolling friction coefficient is around 0.01, varying between 0.007 and 0.014 (TRB, 2006). The tyre radius for a common 205-55-R16 wheel is around 0.316 m. The driving direction cross-sectional area of a typical car can be approximated to be 2.16 m^2. With these assumptions, a passenger car requires

$$T = \left(0.01 \cdot 1950 \cdot 9.81 + \tfrac{1}{2} \cdot 1.225 \cdot 27.8^2 \cdot 2.16 \cdot 0.3\right) \cdot 0.316 = 157.2 \text{ [Nm]}$$

of the total torque to maintain a speed of 100 km/h with the specified wheel arrangement, which equals an average power of 13.8 kW yielding an energy consumption of 0.138 kWh/km. This is close to the measured results of the E-RA car presented in Fig. 1.5.

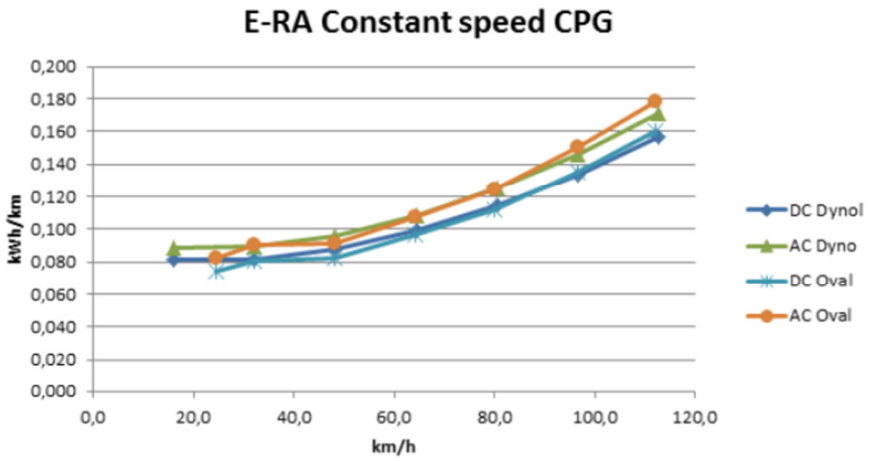

Fig. 1.5. E-RA constant speed energy consumption measurement results from the Chelsea Proving Ground (CPG) test area (E-RA report, 2012).

With the same assumptions, the required torque for a constant speed of 200 km/h would be 447.5 Nm. When the effect of acceleration is taken into account, the need for torque rapidly increases. A ten-second constant acceleration to 100 km/h requires a total wheel torque of 1712 Nm in addition to the constant speed torque requirement. The torque required for the acceleration is almost 11 times the torque of the constant speed operation requirement. This example sets the basis for the machine performance in traction applications. It should be beneficial to use a motor, the efficiency of which is high in constant speed operation, and which is capable of producing a high torque during acceleration. To achieve a high efficiency in constant speed operation, the machine should not be heavily overdimensioned. This means that the machine should be designed closer to the needed average power instead of the peak power requirement.

In synchronous machines, the torque is about inversely proportional to the synchronous inductance (see Eq. 1.2) if the voltage is kept constant. Therefore, a machine with a low synchronous inductance is suitable for acceleration. This favours a permanent magnet machine design with a large magnetic air gap. The field weakening performance instead takes advantage of the high synchronous inductance values. High inductance values do not necessarily cause a problem, because the torque production can be improved with the available voltage reserve at low speeds, where the highest acceleration rates are needed.

If the constant operating speed torque of 100 km/h is selected as the rated value and there is a limited voltage reserve in the system, the synchronous inductance should be less than 0.1 per unit to achieve the 11 times per unit peak torque for the 10 s acceleration to 100 km/h. Depending on the application, the required maximum torque may lead to a significantly larger machine construction than the constant operation would require. This is the case in ICE-powered vehicles, where the engine is overdimensioned to get good acceleration, because the engine overload capability is poor. This generally results in poor efficiency in partial loads required for constant operation. In electric drives, however, it is possible to achieve peak torques several times the rated

torque level for high acceleration and still achieve a small and efficient machine for normal operation.

In our application, the torque production task is divided between all four wheels. The torque required per wheel is about 40 Nm at 100 km/h. The rated torque of 240 Nm per motor would yield a synchronous inductance around 240/428 = 0.56 to achieve the 1712/4 =428 Nm torque for the 10 s acceleration from 0 to 100 km/h if considering a non-salient pole permanent magnet machine with a back electromotive force 1 per unit and a constant U/f =1 control up to the desired speed. Low per unit values of direct-axis synchronous inductances are typical for permanent magnet machines. In field-current-controlled synchronous machines, the L_d can be as high as 2.0 per unit.

The next task is twofold. To accomplish the desired performance, the supply voltage and current ratings have to be selected appropriately. The industrial voltage level (690 V line-to-line) would favour smaller machine dimensions and significantly smaller cabling dimensions than the voltage levels used in the E-RA. The higher voltage ratings lead to a smaller coil turn cross-sectional area, which allows a better control of the end winding overhang in the machine design. Smaller cabling dimensions help to reduce the drive system overall weight.

The industrial voltage level would require a 1000 V DC voltage level in battery-supplied applications. Owing to the stability issues related to the battery management system and the availability of battery capacity values, these voltage levels are avoided in systems of this kind. The reason lies mainly in the lithium ion battery technology used in the study. Lithium-ion batteries require the battery management systems to prevent individual cell charge differences, that is, a State-of-Charge (SoC) mismatch, which is a common problem in series-connected lithium-ion cells. Thus, lower voltage levels are preferred in lithium-ion battery solutions. Still, lithium-ion batteries are practically the standard solution for energy storages in moving electric vehicles because of their high energy storage capability compared with other cell types available. The lithium ion battery also has quite a low self-discharging rate, which supports the usage of this battery technology in vehicle applications. The practical upper limit of the DC voltage seems to settle around 750–800 V, but ratings of 300–400V are much more common. The lower voltage rating requires more current handling capability, which, on the other hand, requires heavier power electronics.

The voltage, flux linkage and rotating speed have to be matched together. In practice, the machine nominal operating speed has to be selected according to the highest rotating speed at which the loading capability is needed. The end of the operating speed range depends on the field weakening region. If the field weakening of the machine is not allowed, the usable voltage should be consumed in this point. Permanent magnet machines require extra attention in the field weakening operation because of the demagnetizing armature reaction from the stator and the temperature sensitivity of the magnet material.

The speed range of the maximum torque should also be considered, because the torque production is proportional to the cross product of the stator flux linkage and current vectors. With a suitable reserve at the supply voltage level, the torque can be boosted by forcing additional flux into the machine. At low speed and high torque, the available voltage reserve can be used to increase the

stator flux linkage. A constant flux operation in traction systems is not a necessity. Especially in battery-powered applications, the machine should be designed to a suitably low voltage level to ensure torque output in conditions where the battery voltage decreases under load. A high current supply makes possible an increase in the flux linkage as the voltage reserve is consumed. The higher flux level can also enhance reluctance torque production. Nevertheless, the use of a flux linkage boost requires suitably loose dimensioning of the magnetic iron circuit in order to fully exploit the voltage reserve in the torque production.

1.2.1 Field of traction applications

As the basis of this doctoral thesis is application specific, the work concentrates on the permanent magnet machine technology. The direct connection to the wheels requires a large torque output as presented in the previous section.

With a flat battery, the field weakening operation requires about 50 % of the stator flux linkage level.

Deep field weakening operation was not required in the machine performance characteristics. This leads to the selection of a PM machine design with a suitable synchronous inductance level. No other machine type has the efficiency and torque capability of the permanent magnet machine. Even more importantly, when comparing for instance with an induction machine, the PMSM machine offers more freedom in machine parameters, such as pole number, dimensions and slots.

Nevertheless, other machine topologies have successfully been applied to hybrid and full electric propulsion systems. Depending on the required performance characteristics and cost issues, there are numerous alternatives for the propulsion machine.

In general, electrical machines represent well-known technology. Currently, the discussion is intense on the suitability of different machine topologies for hybrid and fully electric propulsions. There are several types of electrical machines that can be harnessed to the needs of hybrid and electric systems. The main categories are asynchronous and synchronous AC machines, even though DC machines are also used in low-level applications. The DC technology is not suitable for modern higher-level propulsion applications, but in the transition period toward cost-efficient AC drive systems, the low cost and easy control of the DC machines have favoured the structure in small vehicle propulsion, such as motorcycles, mopeds and all-terrain vehicles (ATVs). One of the problems of the DC system is the need for frequent maintenance because of the mechanical commutator circuit. The same problem also affects the traditional AC synchronous machine even though it probably has the best properties for high torque output and field weakening. Because of its complicated structure and high cost, it has to be left out of the comparison.

The control of frequency converter AC drives is, in theory, more complicated than the control of DC machines, but the efficiency of the AC machines is much higher compared with brushed DC machine drive systems. As the volumes increase, the AC drive systems will be more appealing as the costs will decrease. As a result, the options for hybrid and full electric drive systems are down

to four different machine types and their variations. These are the permanent magnet synchronous machine (PMSM), synchronous reluctance machine (SynRM), induction machine (IM) and the switched reluctance machine (SRM). The basic ideas of these machine structures are presented in Fig. 1.6.

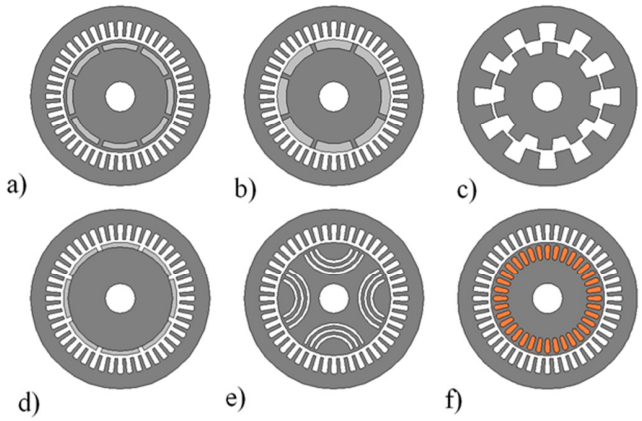

Fig. 1.6. Radial flux machine principle topologies where a) and b) represent salient pole PM synchronous machines, c) switched reluctance machine (SRM), d) non-salient pole PM synchronous machine, e) SynRM machine and f) asynchronous squirrel cage machine.

Considering the synchronous machine types, the permanent magnet synchronous machine (PMSM) and the synchronous reluctance machine (SynRM) are good rivals. A benefit of a synchronous reluctance machine is its low cost structure, although its torque density is not as high as that of a PM machine. The efficiency of the SynRM structure competes head-to-head with that of the IM. The suitability of SynRMs for (H)EV applications has been studied for instance in (Arkadan et al., 2007). The drawback is that the most effective topology in SynRMs is the four-pole design, because this arrangement guarantees a high inductance difference in the SynRMs. This feature makes the machine type suitable for geared high-speed operation and, therefore, inappropriate for direct-drive applications requiring a light machine construction. Some studies about the suitability and design aspects of the SRM technology have been reported in (Qionghua et al, 2003), (Wu et al., 2002), (Ramamurthy, 2001) and (Ohyama et al., 2006). An SRM requires a control of its own, but the structure of the machine is as robust as with the IM and SynRM technology. Both the SRM and SynRM structures are based on reluctance torque production, but the difference is that the SRM has always different pole arrangements in the rotor and the stator. Thus, the torque quality produced in the SRM structure is poor compared with actual AC machines.

An asynchronous machine could be a good choice because of its robust and low-cost structure. The problem is that the use of an asynchronous machine in a propulsion drive system requires the use of gears. The reason for this is that asynchronous machines are more suitable for higher-speed applications, because the favourable pole number of these machines is two or four. In asynchronous machines, increasing the pole number causes a reduction in the power factor. The

power factor decreases along with the magnetizing inductance, which is inversely proportional to the second power of the pole pair number [Heikkilä, 2002]. The total cost of the systems can usually be kept at a reasonable level, because industrial gears are typically inexpensive.

At the moment, the PM technology is the most studied of all machine types. A PM machine does not suffer from a high pole number, which allows a design of lightweight multiple pole arrangements even for direct traction drives.

The PM technology provides the highest torque density compared with any other machine type. This results in smaller and lighter machine structures. There is not necessarily a need for a gear or a complex transmission arrangement, which makes the drive system simple and more robust. The direct connection also helps in reducing noise, as high-speed drive gears are usually not very quiet. A direct drive also requires a high motor torque, which results in a large rotor volume and high magnet material consumption compared with high-speed motor drives.

Thus, a weak point of any direct drive arrangement is the high material cost caused by the high price of rare-earth-based PM materials. The operating speed range is also limited, because the magnets are typically sensitive to temperature and demagnetization. The interest in radial flux PM machine optimization and suitability for (H)EV purposes is demonstrated in numerous articles (Jung et al., 2007), (Xingming et al., 2009), (Faiz, 2006), (Barcaro et al., 2008), (Chau et al., 2007), (Xia, 1998), (Chan, 1996) and (Chau et al., 2008). The proposed machine topologies are mainly radial flux machines, but some approaches to the PM axial flux technology have been proposed for instance in (Cvetkovski et al., 2006) and (Caricchi et al., 1994).

Different propulsion systems have been compared in (Zeraoulia et al., 2005), (IEEE Coll., 1993), (Neudorfer et al., 2008) and (Xiong et al., 2008) with IM, SRM and PM. The main conclusion is that induction machines are competing head-to-head with PM machines; both solutions have their advantages over another. Usually, the factors tipping the scales are the IM cost versus the PM machine torque density. Although the energy storage system is the major issue in the market penetration of the hybrid and electric systems, the electrical machine is still the key factor in the production of energy efficient propulsion systems to replace the current internal combustion engine (ICE) technology.

1.2.2 Electric traction systems

The main categorization of electric traction systems is based on the division between hybrid and full electric traction systems. The common point of the systems is the application of the electrical machine drive in the drive system. The term ‘machine’ refers both to the generating and motoring capability of an electrical machine. Hybrid drive systems as well as full electric drives can be divided into several subcategories. The hybrid drive systems can be divided into series and parallel topologies and the combination of these two according to the electrical machine position in the drive train.

Hybrid electric systems are slightly more complicated than fully electric systems. A hybrid system combines an internal combustion engine with an electrical machine. The focus in the hybrid electric systems is to increase the system efficiency and improve the overall performance of the system. In most cases, both targets are reached, but the weighing between the targeted properties varies depending on which characteristic is emphasized by the application.

Hybrid electric solutions can be divided into two categories or topologies; series and parallel hybrids. The series hybrid solution is closest to a fully electric drive, because the required mechanical work is always produced through an electric motor. Usually, these hybrid electric systems include an energy storage (battery), in addition to a fuel tank.

Systems with a combination of these two are also possible. Full electric propulsion systems can be divided into two subcategories. Compared with the direct connection applications, the difference in an indirect connection is a transmission or a reduction gear included in the system. The subcategories of the hybrid electric systems can also be divided into categories similar to the full electric applications.

The full electric and hybrid solutions can be presented in a component block chart as shown in Fig. 1.7.

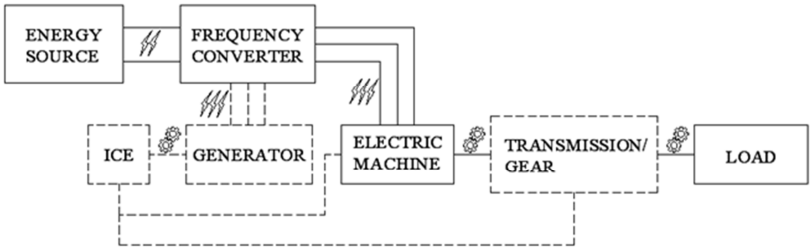

Fig. 1.7. Schematic of a hybrid and full electric propulsion system. Depending on the application, the units presented by a dashed line are optional. Lightning bolts denote electric coupling and cogwheels mechanical coupling.

In general, a full electric or hybrid propulsion system usually includes a combination of an energy source or a storage, a frequency converter, at least one electrical machine and a load. Depending on the system, other parts are optional. Without the ICE and generator blocks, the schematic represents a full electric system with or without a gear coupling. If the ICE and generator blocks are included in the system, we have a series hybrid topology. Again, if the generator block is omitted, the system represents a parallel hybrid solution. It is also possible to have a combined series parallel system containing all of the blocks of Fig. 1.7.

A vast majority of modern efficient drive systems are three-phase systems with frequency converters implemented by advanced control methods. Modern permanent magnet electrical machines in this power range can reach up to 96 % efficiency ratings in constant operation. The energy source, usually a battery or a fuel cell, provides the power for the electric motor through a frequency converter. Some systems are designed with a super capacitor in parallel connection with the battery to absorb or discharge fast and powerful energy pulses.

Modern lithium ion batteries have reported efficiencies up to 95 % in the discharge mode, and the same efficiency can also be applied to the recharge operation (Shidore et al., 2007). The efficiency ratings of frequency converters are also high, usually up to 97 % and above in static operation (WEG, 2009). (Rooks, 2004). The use of a frequency converter is mandatory since it enables a fast response and controllability of the electrical machine in varying load conditions and makes it possible to have different operation modes depending on the application.

The efficiency of an electrical machine is considerably higher compared with internal combustion engines. A modern ICE unit (diesel) can reach up to 40 % efficiency at best, but this only applies to a very limited range of speed and load. Higher efficiencies can be achieved, but only with very large engine sizes and sophisticated auxiliary systems. A study (TRB, 2006) of the passenger car fuel economy indicates that energy flows in a standard-sized passenger car are divided as shown in Table 1.1.

Table. 1.1. Energy loss of an ICE-powered medium sized passenger car (TRB, 2006)**.**

Loss type	Loss percentage [%] of total 100	
	Urban driving	Highway driving
Engine	62	69
Standby	17	4
Drive line	6	5
Braking	6	2
Rolling	4	7
Aerodynamic loss (Air friction)	3	11
Accessories	2	2

According to Table 1.1, only 7 % of the total energy is used in the actual moving process (aerodynamics, rolling) in urban driving conditions and 18 % in highway driving. The ICE units consume most of the energy available. The average ICE efficiency rating in constant operation, including standby losses, is thus 21 % in urban driving and 27 % in highway operation.

When comparing the efficiency of an electric traction system with that of an ICE unit (Table 1.1), the difference is clear. In order to achieve the total efficiency of the system, the individual efficiencies of the drivetrain have to be multiplied with each other.

When considering constant operation and neglecting additional drive line mechanical losses, the efficiency in the motoring mode for a full electric drive system with efficiencies of 0.95 for the motor, 0.98 for the frequency converter and 0.95 for the battery package would be

$$\eta_{\text{Motoring}} = 0.95 \cdot 0.98 \cdot 0.95 = 0.88$$

The total efficiency decreases significantly even though the individual efficiencies are high. If the system has a simple reduction gear, the system efficiency is slightly lower. A simple reduction gear may have an efficiency up to 0.98. According to the values given in Table 1.1, the efficiency of a transmission in an average passenger car is around 0.94. By introducing this to the previous equation, the total efficiency reduces to

$$\eta_{\text{Motoring,gear}} = 0.95 \cdot 0.98 \cdot 0.95 \cdot 0.94 = 0.83$$

Consequently, the efficiency of a hybrid system is significantly lower because of the ICE unit in the system. In some applications, the parallel hybrid solution makes it possible to drive the system without an ICE similarly as in series hybrid applications. Here, the efficiencies are theoretically equal to full electric systems. In series hybrids, the ICE is run at a constant load when power generation is needed. In this situation, the ICE unit achieves its maximum efficiency, assumed here 40 %. Thus, the efficiency in a series hybrid drive system with and without a reduction gear, considering the efficiencies of 0.95 for the generator, 0.98 for the frequency converter, 0.95 for the battery package, 0.95 for the motor, 0.345 for the ICE unit and 0.94 for the transmission, would be

$$\eta_{\text{Motoring}} = 0.345 \cdot 0.95 \cdot 0.98 \cdot 0.95 \cdot 0.98 \cdot 0.95 = 0.28$$

$$\eta_{\text{Motoring,gear}} = 0.345 \cdot 0.95 \cdot 0.98 \cdot 0.95 \cdot 0.98 \cdot 0.95 \cdot 0.94 = 0.27$$

Parallel hybrids can also be operated this way, but usually, the ICE load varies according to the rotating speed, and thus, the ICE efficiency is lower than at a constant load. According to the efficiency evaluation, the full electric application seems to be the most energy efficient solution even though only 40 % of the electric production efficiency and 96 % of the transmission efficiency are taken into account. When comparing the efficiencies, it has to be noted that the production of electric energy in power plants is not lossless. The benefit in full electric applications is the localization of emissions, which are easier to handle than pollution that is scattered.

The introduction of a reduction gear or a transmission in the drive system should also be carefully inspected. The use of a gear depends more on the total cost of the drive system than on the total efficiency or machine size in the drive system. The gear also makes a difference in the machine type selection. Naturally, actual systems are much more complicated by nature; however, the examples give an idea of differences in the traction systems.

1.2.3 History of electric traction

As an introduction to hybrid and full electric applications in moving machinery, a brief glance is taken at the history of these applications. The history of hybrid electric and electric systems is actually quite long. The spur for the development of these systems is the need to travel fast and efficiently. The driving force was – of course – the automotive industry.

At the beginning of the history of automotive technology, the electric, hybrid electric and internal combustion engine technologies were competing on equal terms with each other. The Voltaic cell was developed by Alessandro Volta in 1800, which was the stepping stone for the moving electrical machinery as it enabled a portable energy storage. The first electric vehicles have been reported to be built around 1830s. After that, the development was so rapid that electric vehicles were preferred in taxi and private cars (Larminie, 2003). Even though the internal combustion engine was designed in 1806 by I. Rivaz, the production of petrol started only fifty years later. The

first petrol-powered ICE was used in an automobile by Karl Benz in 1885, and he is usually considered the father of the petrol-powered automobile. A short while later, in 1901, one of the first hybrid electric cars was built by Ferdinand Porsche, the later creator of Volkswagen Beetle (Eckermann, 2001).

The development of the hybrid electric and electric technology stopped because of the invention of the electric starter motor at the beginning of the 20th century and the invention of car mass production by Henry Ford. The electric and hybrid electric systems could not compete with the ICEs because of the slow progress in the energy storage systems. Only after the oil crisis, at the beginning of the 1970s, the interest in hybrid and electric technology has been arising because of the increasing cost of oil, and nowadays, also because of environmental reasons.

There are many hybrid and full electric solutions that often remain unnoticed. Nowadays, most of the railway locomotives have either hybrid or full electric propulsion systems. Local trams are usually full electric as are underground trains. Intercity trains without an electrical line supply are usually equipped with series hybrid technology, which applies a diesel generator that provides power for the wheel motors of the railway engine, which are located in the engine or railcar axles. Modern vessels are also more and more often equipped with similar solutions, the difference being that the electric motor drives the propeller.

The need for high energy efficiency and control over emissions has led to mushrooming of hybrid and full electric solutions in industrial and automotive vehicles. Nowadays, almost every leading manufacturer of automotive and industrial solutions has introduced hybrid or full electric models besides the traditional solely internal combustion engine (ICE) powered units. The alternative topologies are numerous.

So far, no branch of development in hybrid and full electric systems has provided superior performance over others. The push towards cleaner propulsion inevitably leads to petrol-free operation, but substitute fuels are emerging strongly. Bio diesel, ethanol, hydrogen and natural gases are rival substitutes for petrol. The idea of full electric propulsion is thus a faraway dream. Hybrid and full electric systems will develop together, and it seems that no propulsion system will take over the transportation market similarly as ICEs have done.

1.3 Synchronous reluctance-torque-assisted PM machine

As presented in Section 1.2.1, a permanent magnet machine belongs to the synchronous machine category of electrical machines. This means that the rotor follows the stator field with a synchronized speed without sustained slip. The machine excitation is inherent because of the permanent magnets in the rotor. Usually, PM machines are inner rotor machines, but external rotor structures are also found. Permanent magnet machines can be divided into two different categories: salient and non-salient pole machines. The difference is illustrated in Fig. 1.8.

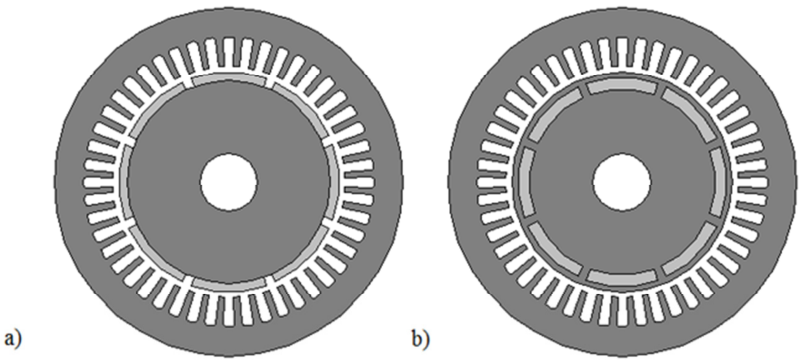

Fig. 1.8. a) Non-salient and b) salient pole (embedded magnets) PM structure

The non-salient pole design is more efficient in the permanent magnet usage. The non-salient pole composition usually means that the magnets are placed in the surface position in the rotor geometry as shown in Fig. 1.8a. The salient pole design (Fig. 1.8b) with embedded magnets loses some of the PM energy as a result of the short-circuiting of the PM poles in the rotor. The salient pole structure is, on the other hand, mechanically more stable. The non-salient pole design is usually more beneficial in low-speed applications, but the magnet poles can be retained with fibre or steel banding.

1.3.1 Fundamentals of electrical machine torque production

The high torque output capability of permanent magnet machines is a result of the long equivalent air gap in the pole direction, which is due to the low permeability of the PM material. Depending on the dimensioning of the machine, the pull-out torque can, in practice, be even 3–4 times the nominal torque. The low inductance may also cause problems in the machine control in frequency-converter-operated systems. From the industrial point of view, the PM technology is quite new. The full potential of the PM technology could not have been reached without modern IGBT switches, which were first developed in the late 1980s. After that, the PM technology gained ground in servo drive applications. This technology has also enabled the use of the PM machine technology in traction applications. The rotor in salient pole PM structures is normally of embedded magnet type.

The principle of the pole arrangement comes usually from the four-pole SynRM type, as presented in Fig 1.9.

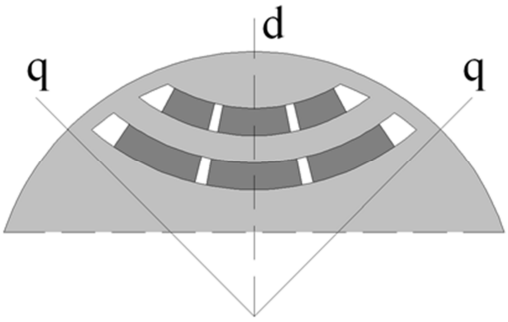

Fig. 1.9. Synchronous reluctance-assisted permanent magnet topology with an embedded magnet structure. The notation d refers to the direct axis and q to the quadrature axis.

Fig 1.9 presents a typical starting point of the machine performance evaluation. The torque output of an electrical machine can be estimated by a two-axis model, which observes the machine behaviour in the direct and quadrature components. The direct-axis component is aligned with the direction of the permanent magnet main flux path.

The principle of saliency is to create flux barriers with embedded air gaps and to enhance flux orientation with permanent magnet patterns to achieve a maximum reluctance difference between the direct and quadrature axes. The flux is forced to travel in the q-axis direction, as will be shown later in this work. In a permanent magnet construction, the reluctance of the direct axis is greater compared with the quadrature-axis reluctance, because the PM material is magnetically close to air. Thus, the direct-axis inductance is low compared with the quadrature-axis inductance. The deduction is quite simple because the inverse product of reluctance, the magnetic conductivity called permeance, has the same unit as the inductance. The effect of the difference in inductances can be evaluated by a per unit value examination. The torque equation to be used is the load angle equation for synchronous machines, based on the two-axis theorem

$$T = 3p\frac{UE}{\omega_s^2 L_\mathrm{d}}\sin\delta + 3pU^2\frac{L_\mathrm{d} - L_\mathrm{q}}{\omega_s^2 2L_\mathrm{d}L_\mathrm{q}}\sin 2\delta \qquad 1.2$$

where

- $L_{\mathrm{d,q}}$ are the synchronous inductances in the direct and quadrature axes, respectively,
- U is the RMS value of the supply phase voltage,
- E is the RMS value of the back electromotive phase voltage and
- δ is the load angle between phasors $\underline{U}$ and $\underline{E}$.

Fig. 1.10 shows a characteristic load angle equation curve for the inductance ratio $L_\mathrm{d}/L_\mathrm{q} = 0.5$. The supply voltage U, the back electromotive force (EMF) E and the rotating speed ω_s are set to 1 p.u.

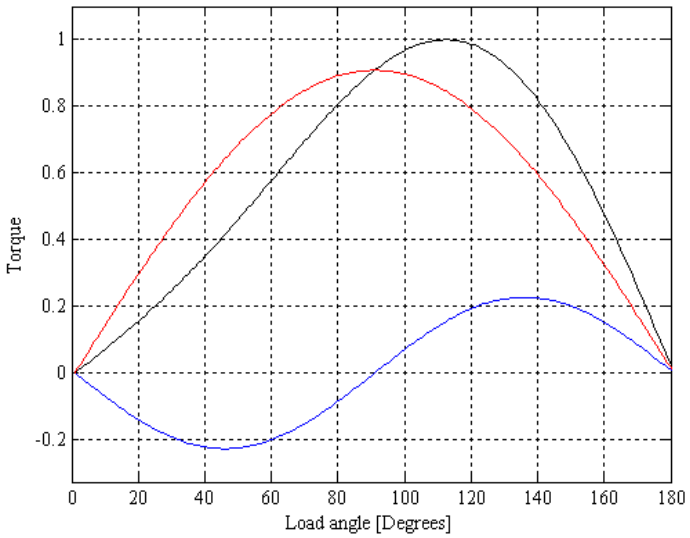

Fig. 1.10. Torque production according to the load angle equation with L_d/L_q = 0.5 and scaled to the peak torque of 1 p.u. The red curve illustrates the synchronous torque part and the blue curve the reluctance part. The black curve is the superposition of these two. The low inductance ratio (<1) results in breakover values above 90 degrees.

By considering a nominal operation at $E = U$ = 1 p.u. and ω_s= 1 p.u., the proportion of reluctance torque T_{rel} to total torque T_{tot} can be reducd to a form

$$T = \frac{\sin 2\delta}{\gamma_{rel}\sin\delta + \sin 2\delta} \tag{1.3}$$

where

$$\gamma_{rel} = \frac{2}{\frac{L_d}{L_q} - 1}. \tag{1.4}$$

The equation also applies to torque production. The percentage value of the reluctance torque compared with the total torque T at different load angles is presented in Fig. 1.11. The normal operation of salient pole PM machines is found in the upper left corner because a low inductance ratio (<1) results in breakover torque values at load angles above 90 electrical degrees.

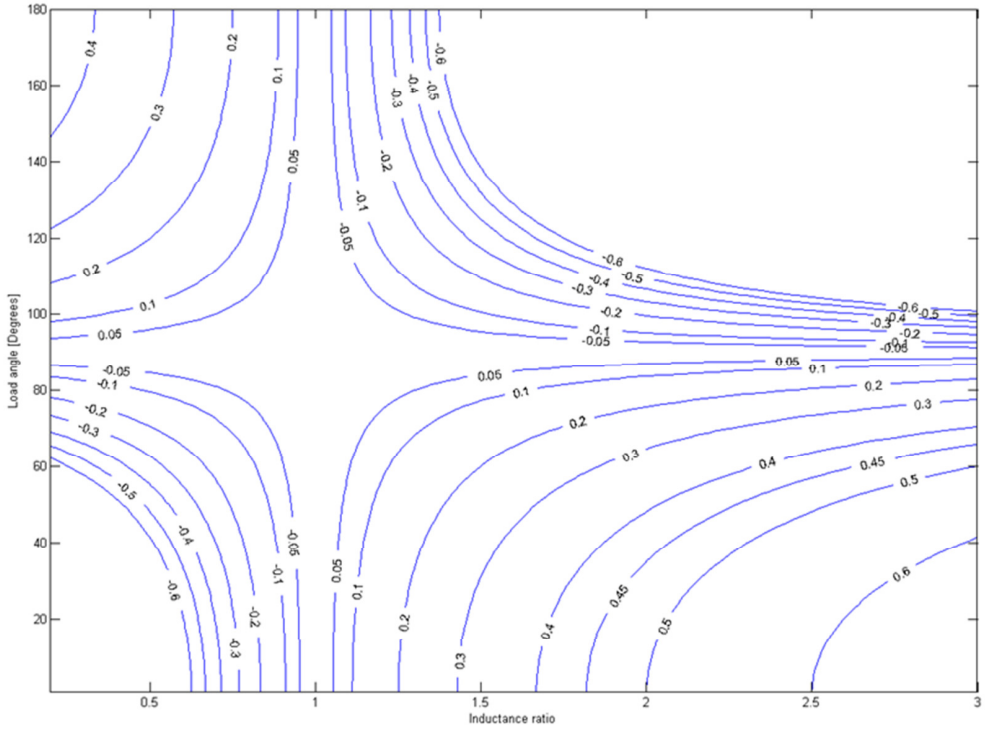

Fig. 1.11. Reluctance torque T_{rel} to the total torque T_{tot} according to the load angle equation for synchronous machines. The horizontal axis refers to the inductance ratio $L_{\mathrm{d}}/L_{\mathrm{q}}$ and the vertical axis to the load angle in degrees. The blue contour line values represent the $T_{\mathrm{rel}}/T_{\mathrm{tot}}$ with $E = U = 1$ per unit.

With the set boundaries $E = U = 1$ per unit, the ratio of the reluctance torque to the total torque produced at a certain load angle depends only on the inductance ratio between the direct- and quadrature-axis inductances. With further modification of Eq. 1.4, the inductance ratio γ_{rel} is let to grow to infinity. Thus,

$$\gamma_{rel} = \lim_{\frac{L_{\mathrm{d}}}{L_{\mathrm{q}}} \to 0} \frac{2}{\frac{L_{\mathrm{d}}}{L_{\mathrm{q}}} - 1} = -2$$

the maximum proportion of reluctance torque is achieved in the point where $\cos\delta$ reaches the minimum, which is – 1 at $\delta = \pi$. Equation 1.3 transforms to

$$T_{\%} = \frac{1}{1 - \left(\frac{1}{\cos\delta}\right)}$$

which yields

$$T_{\mathrm{rel}} = \frac{1}{1 - \left(\frac{1}{\cos\pi}\right)} = 0.5$$

Relying on the theory of the load angle equation 1.2 for electrical machines, the proportion of the maximum reluctance torque of the total torque T at the given boundaries of $E = U = 1$ p.u. is 50 % of the total torque output T.

1.3.2 Pull-out torque maximization

Hybrid and full electric propulsion systems require high pull-out torque capability, which is usually considerably higher than the average rating at which the machine is usually thermally dimensioned. The analytical evaluation of machine performance provides numerous variables to be manipulated in order to affect the machine torque output. Eq. 1.2 gives a good start for the maximization of the machine pull-out torque.

The pull-out torque production can be divided into two categories. According to Eq. 1.2, the torque production depends on the machine inductances and the supply.

The torque in a salient pole structure consists of two parts. The first part in Eq. 1.2 is the synchronous part, which applies to all synchronous machines. The maximum torque $\hat{T}$ for the first part is

$$\hat{T} = \frac{UE}{L_\mathrm{d}} = \frac{U}{\omega_\mathrm{s}} \frac{\psi_\mathrm{PM}}{L_\mathrm{d}}$$

which shows that the maximum torque can be increased by raising the voltage to speed ratio $U/\omega_\mathrm{s} \approx \psi_\mathrm{s}$ or by decreasing the direct-axis synchronous inductance L_d. In traction applications where the voltage reserve is high at the lowest speeds, it is easier to increase the voltage to speed ratio, within the limits of saturation, which makes the minimization of the direct-axis synchronous inductance less important and allows a potential increase in the field weakening performance.

The second term forms the reluctance torque part, which is a special feature for salient pole machines. The reluctance part responds to the excess voltage because of the second power term. The allowable amount of excess voltage has to be confirmed by finite element methods because of the saturation of the inductances. Loose dimensioning of the iron circuit with the excess supply voltage assists in pull-out torque generation, although it increases the machine dimensions and thereby the weight.

To build up the machine reluctance torque, the machine dimensions can be adjusted to favour reluctance torque generation. The analytical determination of synchronous inductances facilitates the design task of increasing the difference between the direct- and quadrature-axis magnetic conductivity. According to (Vogt, 1983) the equation

$$L_\mathrm{m} = \frac{m}{2} \frac{2}{\pi} \mu_0 \frac{1}{2p} \frac{4}{\pi} \frac{\tau_p}{\delta} l' (k_\mathrm{ws1} N_\mathrm{s})^2 \qquad 1.5$$

where

- m is the phase number,
- μ_0 is the permeability of vacuum,
- p is the pole pair number,
- τ_p is the pole pitch,
- δ is the air gap length,
- k_{ws1} is the fundamental winding factor,
- N_s is the winding turn number of a phase and
- l' is the effective length of the machine stack,

shows that the inductance is directly dependent on the second power of winding turns N_s^2, and inversely proportional to the equivalent air gap diameter and the second power of the pole pair number, since

$$\tau_p = \frac{\pi D_s}{2p} \tag{1.6}$$

where D_s is the stator inner diameter. By comparing Eqs. 1.2 and 1.5, the method to maximize the torque output of a PM synchronous machine is easier to understand. Nevertheless, finding an optimal solution is a more complicated task. Eq. 1.5 is for the magnetizing inductance only and does not include the leakage term. The direct- and quadrature-axis synchronous inductances in Eq. 1.2 consist of the magnetizing inductance and the leakage term according to the equation

$$L_{d,q} = L_{md,mq} + L_\sigma \tag{1.7}$$

in which $L_{md,mq}$ refers to the direct- or quadrature-axis magnetizing inductance and L_σ to the leakage component. The leakage affects the inductance ratio between the direct- and quadrature-axis components. A lower leakage component results in a higher inductance ratio, which is more beneficial both to the reluctance torque production and the synchronous torque production. However, leakage can be useful in extending the machine operating speed range to the field weakening region in the PM machine case.

The direct-axis synchronous inductance of a PM machine is inherently low because of the long effective air gap in the direct-axis direction, caused by the low-permeability magnet material. To obtain a lower inductance ratio, the use of tall and narrow magnets in the flux path is preferable to a thin and wide magnet shape.

Based on Eq. 1.2, the decrease in the direct-axis synchronous inductance increases the breakover power output of the machine. The use of the reluctance part requires different actions. According to Eq. 1.2, the inductance of the q-axis has to be maximized in order to increase the reluctance torque component. The inductance in the q-axis direction is increased by adding iron to the q-axis flux path. This is the reason why embedded magnet topologies have inherent saliency.

The above-described idea can be extended by observing Eq. 1.5. The equivalent air gap value can be adjusted between the direct and quadrature axis. The inductance ratio would benefit from a smaller equivalent air gap in the q-axis direction. The direct-axis inductance can also be kept low

by a low phase turn number. This leads to longer machines, but because of the second power of the winding turns, the significance of the winding turn number is greater than the machine length in order to obtain low inductance values.

The pole pitch and the pole pair number are strongly connected to the physical size of the machine along with the machine length. A low pole pitch value can be achieved by increasing the pole pair number. This is good also for decreasing the machine size.

The problem with a small pole pitch and a large pole pair number is that the direct and quadrature axes are geometrically close to each other. If the pole dimensions are scaled down equivalently, the inductance difference should be close to the original pole arrangement. The difference comes from the air gap length. When the pole dimensions are scaled down in multiple pole arrangements, the air gap should also be decreased equivalently. The minimum value of the air gap is within a few millimetres for mechanical and electric reasons. Too short an air gap may cause manufacturing problems as well as increased friction losses and harmonic losses on the rotor surface.

Depending on the design case, the degrees of freedom in changing the machine dimensions vary. The machine outer dimensions can be strictly specified, which causes restrictions to the machine design. The operating speed range and machine performance requirements also affect the allowed dimensions. Because of the large number of variables and multiplier effects in the machine design, the applied solutions have to be weighed very carefully to achieve an optimal machine structure for the given application.

Rough estimates on the machine performance can be obtained by swift analytical calculations, but the feasibility of the decisions has to be tested in a finite element environment.

1.3.3 Effect of saliency and leakage on the drive performance

To obtain a broad field weakening speed range, the direct-axis inductance has to be designed large enough. With a large direct-axis inductance, the field weakening requires less demagnetizing I_d current at the same operating speed compared with a small direct-axis inductance. The drawback in large L_d values is the reduction in the pull-out torque as the pull-out torque of a PM machine is inversely proportional to the electrical machine direct-axis inductance as presented in Eq. 1.2. A suitable amount of leakage helps achieving higher speeds in field weakening operations.

Depending on the application, the weighing between the power factor, the operating speed range and the torque output characteristics have to be altered according to the desired behaviour.

A phasor diagram presentation gives more information about the machine operation in different conditions. This section concentrates on the effect of leakage and saliency on the electrical machine performance.

An $I_d = 0$ control is good for rotor surface permanent magnet applications as it does not stress the magnets with a counter-magnetizing field. This control method also gives the highest torque to

current ratio in non-salient pole machine designs. With salient pole structures, a small amount of negative d-axis current is required for the maximum torque output.

Figures 1.12 and 1.13 represent salient and non-salient pole designs, respectively. In addition, the power factor curve is presented in the first quadrant of the coordinate system, and the specific power factor corresponding to the presented phasor arrangement is highlighted with a vertical line crossing the power factor curve. Both of the phasor diagrams are presented for motor operation, where the rotation direction of the machine is counterclockwise. Both cases represent under-magnetized machine operation, which results in a lagging power factor, that is, an inductive connection to the supply. To show the difference between salient and non-salient pole machines, the inductance values for Figs. 1.12 and 1.13 are selected as $L_d = L_q = 0.2$ p.u. for the non-salient pole design and $L_d = 0.2$ p.u. $L_q = 0.4$ p.u. for the salient pole case. The permanent magnet flux and the supply current I_s are 1 p.u. The leakage component is 0.1 p.u in both cases.

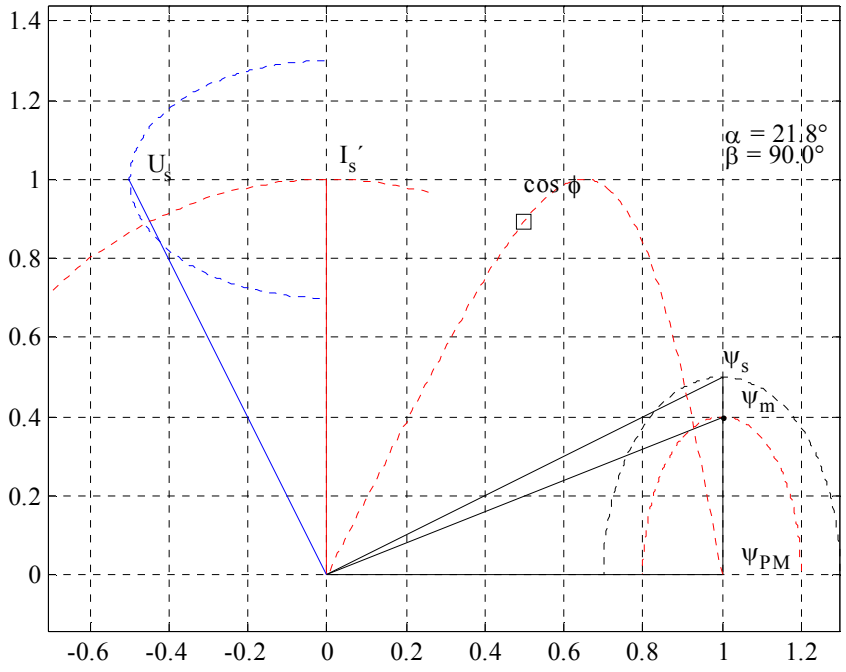

Fig. 1.12. Phasor diagram presentation of the steady-state operation of a non-salient pole machine; $I_d = 0$. The stator resistance is neglected. The power factor is presented as a function of per unit current angle from 0 to 180 degrees.

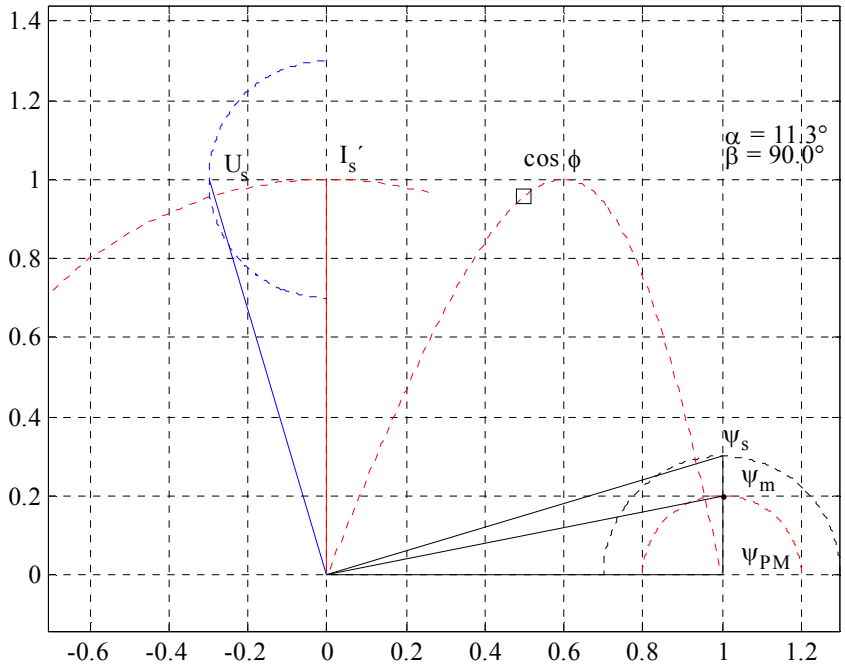

Fig. 1.13. Phasor diagram presentation of the steady-state operation of a salient pole machine; $I_d = 0$. The stator resistance is neglected. The power factor is presented as a function of per unit current angle from 0 to 180 degrees.

The diagrams are based on the torque production equation

$$T \sim \psi_{sd} i_{sq} - \psi_{sq} i_{sd} \qquad 1.8$$

The current angle is denoted by α. The stator flux linkage is an integral of the supply voltage and is lagging the voltage phasor by 90 degrees. The leakage term is lost in the energy transfer process and results in a magnetizing flux phasor that represents the magnetic tension affecting the rotor surface. The pole follows the magnetizing flux by an angle β. The strength of the magnetic coupling is presented with the direct- and quadrature-axis flux linkages.

Modification of the current angle causes the phasors to travel along circular paths, indicated by a dashed line, the radius of which is determined by the supply current and the direct- and quadrature-axis inductances. The increase in current produces larger constant operating circles, and vice versa. The phasors rotate along the circles in a counterclockwise direction as the current angle increases. The non-salient pole design operates in the same way, but the phasor paths are elliptical as a result of the inductance difference in the direct and quadrature axis. This applies to constant inductance terms, but in reality, the inductances depend on the magnetization state of the machine. Non-salient pole machine inductances are quite steady until the machine reaches saturation and the

inductances decrease rapidly. The salient pole design is more complicated because the sheet metal provides alternative flux paths depending on the rotor saturation state. The machine inductances in salient pole designs have to be determined by a careful analysis based on a finite element method. The purpose of the analysis is to assess the inductance behaviour in order to predict the machine performance in varying load conditions. This was clearly shown in the design process of the prototype machines.

Field weakening is problematic in PM machine designs, especially in non-salient pole structures. In order to extend the machine operating speed range beyond the supply voltage limits, the machine PM excitation has to be weakened to enter the 'overspeed' region. At high temperatures, the PM material *BH* curve is not linear at low B_r values. If the PM machine is not designed for field weakening purposes, it is possible that the countermagnetization shifts the operating point below the permanent magnet demagnetization point resulting in irreversible demagnetization.

Traditional machine design usually aims to minimize the leakage, because it degrades the power factor of the machine and decreases the load capability of the machine. This is true for industrial machine designs with a fixed operating point. Since the propulsion system requires operation over a large rotating speed range, the effect of the leakage term on the machine performance has to be analysed through the speed range. The benefit from the leakage is found in the field weakening region.

By further manipulating Eq. 1.8 to a form

$$T \sim \psi_{\mathrm{PM}} i_{\mathrm{sq}} + \left(L_{\mathrm{d}} - L_{\mathrm{q}}\right) i_{\mathrm{sd}} i_{\mathrm{sq}} \qquad 1.9$$

it is possible to investigate the effect of the saliency and the leakage component on the machine performance characteristics. The results are presented in Figs. 1.14 and 1.15.

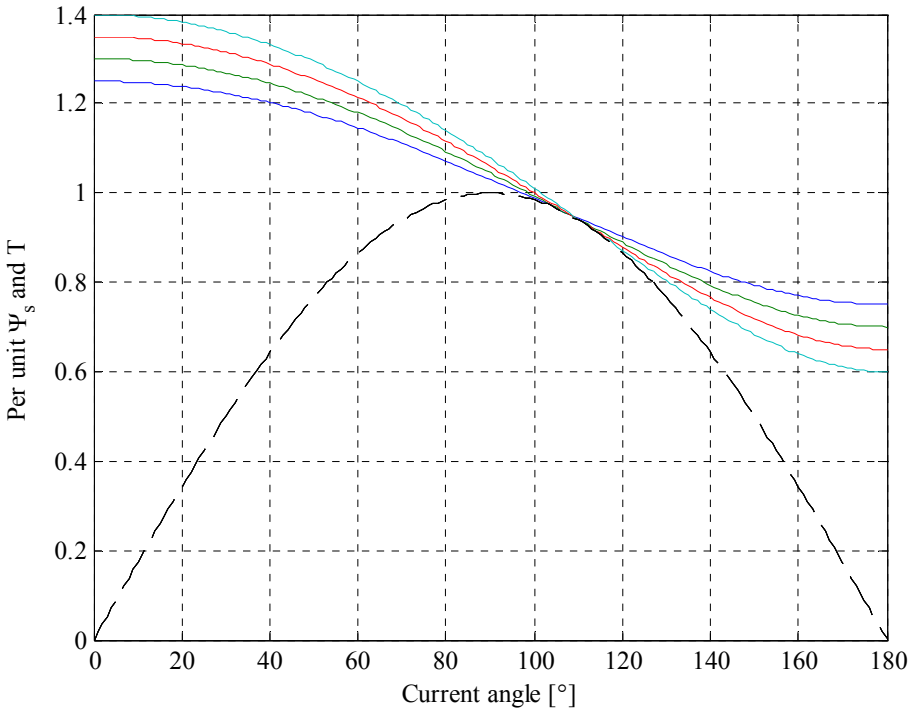

Fig. 1.14. Non-salient pole machine (L_d = 0.2 p.u. L_q=0.2 p.u.) torque production as a function of current angle. The dashed lines indicate the torque production curve with a 1 p.u. current. The leakage components are 0.05, 0.10, 0.15 and 0.20 p.u. The coloured lines from top to bottom on the right side of the figure depict the respective armature fluxes in p.u. PM flux is 1 p.u.

The armature flux curve in Fig. 1.14 is inversely proportional to the rotating speed of the machine. As the leakage component increases, the field weakening region deepens with the same countermagnetizing current. A suitable amount of leakage in the machine design seems to favour the field weakening characteristics of a PM machine. The power factor peak also shifts further to the field weakening region as the leakage component increases.

The saliency itself does not have an influence on the field weakening range. This can be seen in Fig. 1.15.

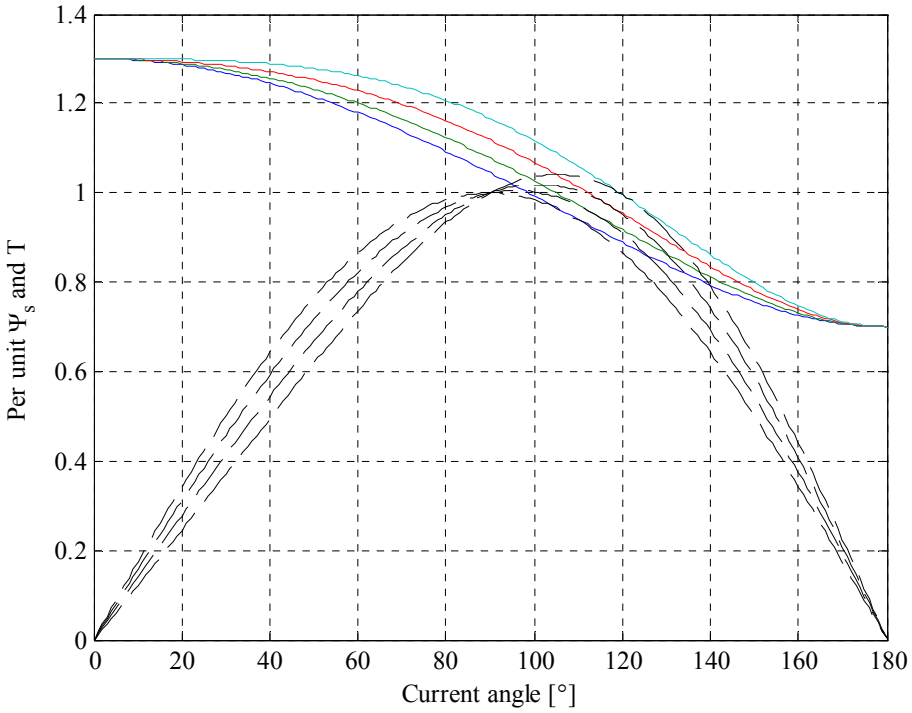

Fig. 1.15. Salient pole machine (L_d = 0.2 p.u.) torque production as a function of current angle. The dashed lines are the torque production curves with a 1 p.u current. The coloured lines indicate the corresponding armature fluxes in p.u. from top to bottom with the L_q values of 0.2, 0.3, 0.4 and 0.5 per unit, respectively. PM flux is 1 p.u.

The field weakening speed range in Fig. 1.15 is the same regardless of the q-axis inductance component, but the torque curves are different. The saliency is beneficial for the torque output capability in the field weakening region compared with non-salient pole designs. As with the leakage component, the increase in saliency shifts the power factor peak deeper to the field weakening region as presented in Fig. 1.13.

1.3.4 Permanent magnet materials

Permanent magnetism is a unique feature achievable only in ferro- and ferrimagnetic solid substances. These materials are called hard magnetic materials because the coercive force to oppose any change in the magnetizing direction is high compared with soft magnetic materials.

The scientific work of William Gilbert, *De Magnete* (1600), gave rise to the modern theories on magnetism. However, large-scale industrial use of different permanent magnet materials started only in the late 1960s. This is because the relationship between electricity and magnetism was

discovered by Oersted in 1820, but it took more than 100 years to produce the first industrial permanent magnets materials in the early 20th century (Elliot, 1993).

Magnets are nowadays widely used in different everyday devices. Most of these applications are so common that the utilization of permanent magnet materials remains unnoticed. Permanent magnets can be found for example in RC cars, refrigerator door seals, computer hard discs, household blenders, washing machines, X-ray equipment, hybrid vehicles, credit cards, compasses and loudspeakers, just to mention but a few.

Particle accelerators can also be built with permanent magnets. The largest particle accelerator in the world is located in CERN, France, which has 8 T superconducting niobium-titanium dipole electromagnets in the Large Hadron Collider. The permanent magnets are needed to keep the particle beam inside the accelerator (Russenschuck, 2010).

Modern transportation techniques have also advanced the use of permanent magnets. The Indutrack technology, which uses a Hallbach array for permanent magnet levitation, is a completely passive technology that operates on rare earth NdFeB magnets (Post, 2000). Prototypes have been built, and NASA in the USA has considered the Indutrack technology also for a rocket launching application.

Besides their usefulness in commercial products, the main advantage of permanent magnets is found in industrial energy conversion solutions.

The relative ability of a magnet material to produce work is measured by the maximum energy product value [J/m^3]. The magnetic material usually operates in the second quadrant of the *BH* curve, which illustrates the magnet capability to oppose demagnetization. In order to efficiently use the magnet potential, the magnet operating point should be close to the maximum energy product. With a suitable magnet material, the operating range of the material can also be extended to the third quadrant of the *BH* curve. A characteristic magnetization curve of a modern NdFeB magnet Neorem 493a/593a (Neorem Magnets) is presented in Fig. 1.16.

The magnetism in ferromagnetic materials occurs when the small magnetic domains are aligned in the same direction. The non-magnetized materials have their elementary magnets arranged in arbitrary directions. In hard magnetic materials, the orientation of the elements is difficult because of the coercive force. However, if the field is strong enough, the Bloch areas deform and the elementary magnets orient according to the field.

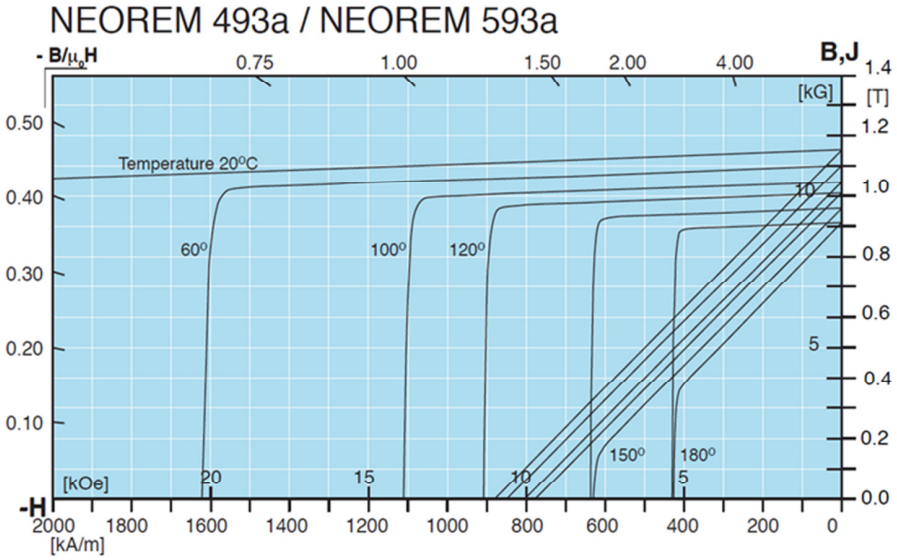

Fig. 1.16. Characteristic magnetization curve of the NdFeB 493a grade magnet by Neorem Magnets data sheet (Neorem, 2008).

As it can be seen, the demagnetization *BH* curve of Neorem 493a in the second quadrant is linear in temperatures below about 150 °C. The maximum energy product is reached in the middle of the linear demagnetization curve. Because the magnetization curve is linear in the second quadrant, the maximum energy product can be calculated easily with the co-energy since it is equal to the energy stored into the system. Thus, the maximum energy product W is

$$W = \int \frac{1}{2}\mu H^2 dV \qquad 1.10$$

Figure 1.16 shows also the material *HJ* (polarization) curve, which illustrates the magnetization of the material in different temperatures. The line crossings on the *B*-axis are for the corresponding temperatures for both *H* and *J*.

At present, the NdFeB material is the most popular permanent magnetic material because of its high energy product. Values as high as 450kJ/m^3 have been listed (Pyrhönen et al., 2008). The drawback of this material is its poor heat endurance, and therefore, the operating temperature must be low to get the most out of the magnet material. The second best option is the SmCo material, according to the energy product, but its heat endurance is significantly better compared with neodymium magnets. Depending on the compound, the SmCo magnets can be used in temperatures well beyond 200 °C. The third major magnet type is the AlNiCo magnet, which has the highest heat endurance of the important industrial magnet materials. Nevertheless, its energy products are below 100 kJ/m^3. In electrical engineering applications, the usable brands are not the state-of-the-art compounds, and thus, the energy products of NdFeB, SmCo and AlNiCo magnets in industrial usage are in the range of 250–400, 100–200 and below 80 kJ/m^3, respectively.

Hard ferrimagnetic compounds are also useful in some applications. The ferrite compounds are not very strong compared with rare earth and AlNiCo magnets, but their advantage is the low cost. Ferrites can also be used to produce complex magnetic shapes and structures by a modern molding technique. The energy products do not reach 30 kJ/m^3 in industrial grades, but the material is applicable to loudspeakers, magnetic pickup of different instruments, small-scale electric motors and magnetic holding systems. The physical parameters of different hard magnetic materials are listed in Table 1.2.

Table. 1.2. Typical material parameters for common hard magnetic materials (Miller, 1994) (Pyrhönen et al., 2008).

Property	SmCo	NdFeB	AlNiCo	Ferrites
H_c [kA/m]	493–1590	800–1990	40–130	180–400
B_r [Vs/m2]	0.7–1.35	1.0–1.4	0.6–1.35	0.35–0.43
α_T [%/°C]	–(0.03–0.05)	–(0.08–0.15)	–(0.01–0.02)	–0.2
ρ [g/cm3]	8.2–8.4	7.4–7.6	7.3	4.5–5.1
Curie point [°C]	700–800	310–350	850	450
σ [MS/m]	1.16	0.55–0.9	2.13	0.01
μ_r	1.02–1.07	1.04–1.1	1.9–7	1.05–1.15

Common to all major permanent magnet compounds is the brittleness of the materials. The bending and tensile strengths are usually far lower than a couple of hundred Newtons per square millimetre. In return, the compression strength of the magnets is good. The strength of the materials must be carefully taken into account in the design process when the magnet fixing procedure is determined. Densities are quite equal when comparing rare earth and AlNiCo magnets. The ferrites are a somewhat lighter, which is due to their porous structure, but on the other hand, the resistivity is significantly higher than in the ferromagnetic magnets.

In electrical machines, the permanent magnet technology has evolved quickly along with the new permanent magnet materials. Permanent-magnet-assisted motors have several advantages over traditional induction and synchronous machines. PM machines have a high efficiency and torque product, especially in low-speed applications. In current domestic applications, the NdFeB magnet is the most common magnet type among the PM machine types. Although it has some physical drawbacks, as mentioned above, it still has two significant benefits: a high energy product and a low price. The drawbacks can be avoided by a careful machine design; the most important aspect in the design is the correct determination of the operating point of the magnet. Fortunately, there are numerous different brands of NdFeB magnets, which can be selected according to the desired characteristics.

The operating point of the magnet can be examined analytically, but the method is rather arduous. A more convenient engineering approach is achieved with finite element method programs. Under load operation, the flux density of the magnet and the corresponding coercive force are solved, and the operating point at a certain temperature-dependent *BH* curve can be drawn in the

demagnetization curve. This usually requires several calculations at different temperatures, but it is a relatively fast and straightforward task to perform. The load line determination is very important already at the beginning of the machine design.

1.3.5 Torque quality

Torque quality is one of the concerns in the discussion of the traction machine performance. In ICE-powered systems, the torque is pulsating but the mechanics, that is, the torque transmission line, filters the pulsating torque, which results in a smooth operation within the rotating speed limits of the CE unit. Electrical machines also suffer from the pulsating torque form to some extent. Slotting causes spatial reluctance differences in the flux path while the rotor is rotating, which yields a pulsating torque wave form called cogging. Another source is the electromagnetic distortion caused by the winding space harmonics resulting from the winding scheme and current wave form imperfections, which are generally described as torque ripple. A torque ripple that is less than 1–2 % of the rated torque can be considered low (Miller, 1994). There are multiple ways to minimize the cogging effect and torque ripple. A modern frequency converter control is usually fast enough to compensate the torque pulsation for a smooth output. This is due to the fact that the mechanical time constants are much larger compared with the control loop update speed. As mentioned above, winding arrangements with a low space harmonic content can be used to minimize the torque ripple in the machine design process. The cogging torque can be decreased with semi-magnetic slot sticks and skewing. Increasing the number of slots per pole also reduces cogging (Miller et al., 1994). The tooth geometry can also be modified to decrease variation in the magnetic conductivity in the air gap space for instance by using bifurcated tooth tips.

1.4 Outline of the work

This doctoral thesis studies the traction motor design for a performance-oriented road vehicle application with a direct four-wheel drive. In the literature study, no distinct pattern was found for the methods for traction machine design in hybrid and full electric driving systems. Although the history of electric traction development is long, the topic of directly connected permanent magnet traction machines is quite new, and numerous alternative approaches have been proposed. Despite the wide experience in different special machine designs, there is no previous experience in the traction motor development for a vehicle environment at the university, and therefore, a doctoral study on the traction machine design was considered an appropriate opening to this research field.

The structure and contents of the doctoral thesis are summarized as follows:

Chapter 1 introduces the topic and objectives of the thesis. The study starts with a presentation of the requirements set by the vehicle environment and the application-specific boundary values. A brief glance is also taken at the history and development of hybrid and full electric propulsion systems. Hybrid and full electric systems are categorized, and the differences and similarities between the propulsion systems are investigated including electrical machine type selection and

fundamental sizing. The causality between the key design features is presented to establish understanding between the machine dimensions and performance. The chapter draws the outlines of the thesis and describes the scientific contribution of the study.

Chapter 2 addresses the electrical machine design areas in more detail including the electromagnetic and thermal design and the evaluation of losses and efficiency.

Chapter 3 introduces the prototype machine design process. The machine structures are presented in detail, and a performance analysis is carried out with analytical and finite element models. Optimization of the machine structure is performed in order to determine the boundary values of the drive system. The developed thermal model is presented in addition to the model-specific details.

Chapter 4 introduces the measurement systems. The analytical and finite element results are verified by experimental studies. An analytical thermal model of the static and dynamic performance is applied to the measured data.

Chapter 5 provides conclusions on the doctoral thesis including the key contributions of the work, achieving of the objectives and recommendations for future work.

1.5 Scientific contribution of the work

The scientific contributions of the doctoral thesis are summarized in the order of importance:

- The doctoral thesis proposes a traction machine design sequence with combined electrical and thermal design methods for vehicle traction within the application-specific geometrical boundaries.
- The work demonstrates the importance of the cross-saturation effect in the traction machine design compared with the traditional two-dimensional approach. The work demonstrates the importance of the coupling of the electric and thermal design machine designs where joule losses are dominating.
- The thesis demonstrates the effect of the battery-package-related supply voltage variation on the machine performance over a certain speed range.
- The study proposes, by introducing a special magnet module design, a cost-efficient machine structure with improved saliency. The machine structure is designed for an increased speed range and torque density to meet the performance requirements in vehicle traction systems.
- The work promotes the benefits of a salient pole structure in vehicle traction.
- The study provides a comparison of a special magnet module machine design with a traditional embedded magnet machine design by a prototype machine of each structure.

1.6 List of publications

This section lists other publications in which the author of this doctoral thesis has been author or a co-author and which are relevant to the doctoral work. Other supporting publications related to the topic are listed separately.

1.6.1 List of related publications

- Nerg J., Rilla M. and Pyrhönen J., "Thermal Analysis of Radial-Flux Electrical machines With a High Power Density," *IEEE Transactions on Industrial Electronics*, Vol. 55, Issue 10, October 2008, pp. 3543–3554.

- Rilla M., Niemelä M. and Pyrhönen J., "Thermal Evaluation of the Effects of Dimensional Parameters on Low Speed Permanent Magnet Machine Design," In the *XI International Symposium on Electric Fields*, 2007.

- Lindh P., Rilla M., Jussila H., Nerg J., Tapia J.A. and Pyrhönen J., "Interior Permanent Magnet Motors for Traction Application with non-Overlapping Concentrated Windings and with Integer Slot Windings," *International Review of Electrical Engineering (I.R.E.E.)*, vol. 6, no. 4, August 2011.

- Nerg J., Rilla M., Ruuskanen V., Pyrhönen J., Ruotsalainen S., "Design of Direct Driven Permanent magnet Synchronous motors for an Electric Sports Car", In the *International Conference on Electrical Machines*, 2012.

- Lindh P., Nerg J., Pyrhönen J., Polikarpova M., Jussila H. and Rilla M., "Interior permanent magnet motors with non-overlapping concentrated windings or with integral slot windings for traction application", In the *XV International Symposium on Electromagnetic Fields*, September 1–3, 2011.

1.6.2 List of supporting publications

- Rilla M., Niemelä M., Pyrhönen J., Pekola J. and Jäppinen J., "Design of a 60 kW, 9000 rpm non-salient pole PM-machine," In the *18th International Conference on Electrical Machines*, Vilamoura, September 6–9, 2008.

- Immonen P., Laurila L., Rilla M. and Pyrhönen J., "Modelling and simulation of a parallel hybrid drive system for mobile work machines," In *EUROCON*, St. Petersburg, May 18–23, 2009, pp. 867–872.

- Pöllänen R., Nerg J., Rilla M. and Pyrhönen O., “Transient Thermal Model for Radial Active Magnetic Bearing,” In the *Tenth International Symposium on Magnetic Bearings*, 2006.

2 Key design areas of a traction machine

Traditional electrical machine design relies on experimental knowledge of suitable machine parameters based on data gathered from actual machines. Depending on the cooling arrangement, machine type and size, there are certain guidelines available to determine the thermal performance characteristics of the machine.

With permanent magnet traction machines, an additional set of design tools is required. Because of the sensitivity of the permanent magnet material and varying load conditions, more accurate knowledge of the machine thermal behaviour is needed for the performance analysis. The machine temperature behaviour in varying load conditions can be estimated by a lumped-parameter thermal model. The use of the model requires knowledge of the loss generation inside the machine and understanding of the mechanisms of heat transfer.

This chapter provides an analysis of the electrical dimensioning of a traction machine with an introduction to heat transfer mechanisms, lumped-parameter modeling and the evaluation of loss distribution in electrical machines.

2.1 Electromagnetic design

The design of an electrical machine starts from the dimensioning of the rotor, after the desired output torque has been decided. The application-specific dimensional boundary conditions should also be taken into account at this point. Analytical presentation of the machine structure and the electrical properties of an integral slot machine are easiest to provide by a single magnetic path presentation, which consists of one pole of the machine geometry.

2.1.1 Basic design rules

Designing an electrical machine for a mobile solution differs from the design process of a traditional industrial machine. According to the standard IEC 60034-1, there are industrial limits for the pull-out torque depending on the machine type. Synchronous motors with a salient pole structure should be capable of handling a 35 % excess torque. Non-salient pole structures have a higher peak torque requirement (50 %); the same as with cage induction machines with a starting current less than 4.5 times the rated current (otherwise 60 %). These limits are for direct-on-line machines and for a 15 s continuous load at required peak torque.

Power tool and traction applications may easily require several times the rated torque in transient operation. This cannot be reached by industrial-type machine dimensioning. Thus, it is challenging to optimize the machine structure according to the performance expectations.

First, it is important to determine the initial values with care. At least the following values are required:

- average and maximum torque, T_{avg} and T_{max}
- nominal and maximum rotating speed, n_n and n_{max}
- energy supply voltage and current, U_{LL} and I_L
- limits for the machine length and diameter, l_m and D_m and
- cooling method and maximum temperature of the cooling fluid.

Despite the requirement for a better total system efficiency, the optimization of the system is not entirely a matter of physics but rather an attempt to reach a tolerable cost efficiency without adversely affecting the drive performance.

The PM rotor can be made thin and long or short and large in diameter depending on the space limitations. With a low rotating speed, a large radius is preferable with a high pole number, since the PM rotor structure can be made light because of multiple flux paths.

The output torque of the machine depends on the active surface area of the rotor, the rotor radius, the air gap flux density and the linear current density. The rotor produces a certain force on the active surface area according to the tangential stress σ_{tan}, which is proportional to the product of the air gap flux density B_δ and the linear current density A. The force acting on the cylindrical surface area, depending on the pole effective area, produces an amount of torque directly proportional to the rotor radius r_r. The torque equation is thus written as

$$T = \sigma_{\tan} r_r 2\pi r_r l'_r = \sigma_{\tan} S_r r_r \qquad 2.1$$

where

- l'_r is the effective length of the rotor stack,
- r_r is the rotor radius,
- σ_{tan} is the tangential stress component and
- S_r is the rotor cylinder surface active area.

In traditional machines without cooling ducts, this equals the rotor stack geometrical length l_r plus two times the air gap length δ of the machine (Vogt, 1983). In PMSMs, however, the length is more complicated to determine (Pyrhönen et al., 2010).

In permanent magnet machines, the tangential stress produced by the armature winding has to be matched with the permanent magnets. The tangential stress is a multiple of the peak value of the air gap flux and the peak value linear current density. The average stress $\sigma_{\tan}$ is then calculated as

$$\sigma_{\tan} \approx \frac{1}{2} B_\delta \hat{A} \cos\varphi. \qquad 2.2$$

Because the flux density represents the voltage in the equation and the linear current density the current of the machine, the equation has to take the power factor cos φ into account, which in this

case has to be estimated and corrected later. Guidelines for the tangential stresses can be found in the literature. Some guidelines can be found in Tables 2.1 and 2.2.

Table. 2.1. Tangential stress values for different machine types in rated operation according to (Miller, 1994). The lower values are for naturally cooled machines and the higher ones for external cooling fan applications. TE stands for 'totally enclosed'.

Machine type	Tangential stress component [kPa]
Small TE motors (Ferrite)	3.4–6.9
TE motors (Sintered rare earth or NbFeB)	6.9–20.6
TE motors (bonded NdFeB)	10.3 typical
Aerospace machines	13.8–34.4
High-performance servomotors	6.9–20.6
Large liquid-cooled machines	69.0–103.4

Table. 2.2. Tangential stress and linear current density values for different machine types in rated operation according to (Vogt et al., 1983). The lower values are for machines with natural convection and the higher ones for external cooling applications.

	Salient pole	Non-salient pole		
Cooling method	**Air**	**Air**	**Water**	**Direct water**
A [kA/m]	35–65	30–80	90–110	150–200
$B_{\delta 1}$ [Vs/m^2]	0.8–1.05	0.8–1.05	0.8–1.05	0.8–1.05
$\sigma_{\text{tan, min}}$ [kPa]	12.0	17.0	51.0	85.0
$\sigma_{\text{tan, avg}}$ [kPa]	21.5	36.0	65.5	114.5
$\sigma_{\text{tan, max}}$ [kPa]	33.0	59.5	81.5	148.5

Tangential stress may momentarily have higher peak values than those presented in Table 2.1 and 2.2 depending on the synchronous inductances. Even though the torque depends on the surface pole area, the torque production favours larger rotor diameters. Typical current density limits for different cooling methods are presented in Table 2.3.

Table. 2.3. Typical current density values for different machine cooling methods. (Vogt, 1984) (Miller, 1994). TE stands for 'totally enclosed'.

Machine type	Current density [A/mm^2]
Air cooled (TE)	**3-5(1.5–5)**
Air-over Fan-cooled	**5–10**
Liquid cooled (direct water)	**7–10 (10–30)**

Figure 2.1 presents the dependence of the rotor diameter and length on the torque production, based on Eq. 2.1, at a 36 kPa tangential stress, applied to the rotor surface by varying the rotor diameter to the rotor length ratio in relation to the actual rotor diameter.

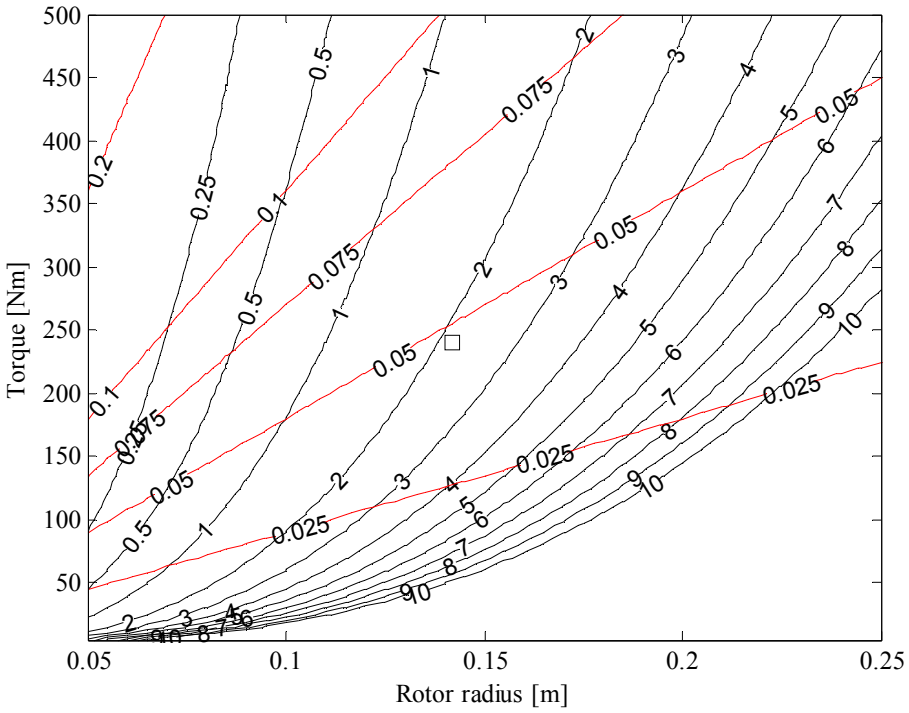

Fig. 2.1. Contour plot describing the effect of r_r/l as a function of rotor radius r_r and produced torque. The calculations are carried out with a 36 kPa tangential stress and cos φ = 1, and 80 % of the rotor air gap surface area is considered magnetically active. The red lines are contours for the constant rotor active area in square meters [m^2] and the black lines represent r_r/l proportions. The square markers indicate the design point of the developed machines with a 0.284 m rotor diameter, 0.065 m rotor length and 240 Nm of torque.

The rotor contour curve is of quadratic form. According to the slope shapes in Fig. 2.1, the machine torque production prefers an increase in the rotor radius to an increase in the rotor length. A 10 % increase in the rotor diameter results approximately in 5.8 % more torque compared with a 10 % increase in the rotor length. In both cases, the surface area of the rotor increases by the same amount, but the extra torque comes from the larger radius. This can also be verified by Table 2.4, which lists the recommended r_r/l' values for synchronous machines according to the pole number.

Table. 2.4. Recommended rotor radius to rotor length ratios (Vogt, 1983).

p	1	2	3	4	5	6	7	8	9	10
r_r / l'	0.33–1	0.90	1.10	1.27	1.42	1.56	1.68	1.80	1.91	2.10

According to Table 2.4, it is recommended to use a shorter rotor length in relation to the rotor diameter as the pole number increases (Vogt, 1983). The larger pole number most likely promotes low rotating speeds as the low values for one (1) and two (2) pole pair machines are intended for higher-speed machines.

2.1.2 Windings

Magnetic design complements the basic machine design and determines the machine active dimensions. After the definition of initial parameters, the desired air gap flux $\hat{\Phi}$ can be determined as

$$\hat{\Phi} = \alpha_i \hat{B}_\delta \frac{2\pi r_\delta}{2p} l' \qquad 2.3$$

where

- $(2\pi r_\delta / 2p)$ is the pole pitch τ_p
- α_i is the per unit average of the flux density on a pole,
- p is the pole pair number and
- l' is the effective stack length.

The flux concentration over the pole area is considered evenly distributed. α_i is $2/\pi$ for a sinusoidal flux density distribution, but in the surface PM case, α_i is replaced by α_{PM}, usually considered to be w_{pm}/ τ_p, which is normally enough for analytical dimensioning. The length of the machine is an important parameter, especially at low rotor length to rotor radius ratios. The peak value of the air gap flux density can be selected for example from Table 2.2. In the PM case, it is advisable to keep the maximum peak value below or equal to 0.9 T (Miller, 1994).

The pole number is an optimization issue. As noted above, the pole number itself does not determine the torque output of the machine, but it has a significant effect on the iron core dimensions and the pull-out torque characteristics, because synchronous inductance is inversely proportional to the square of the pole number which can be deduced by combining Eqs. 1.5 and 1.6 in Section 1.3.

Small pole numbers result in thicker iron passages as a result of larger flux components. A large pole number requires thinner iron passages, and thus, the rotor dimensions can be increased in the radial direction to enhance torque production. The stator yoke can be made thinner because of the

multiplication of the flux paths. The pole number is limited by the increasing supply frequency and the required rotating speed range.

With the magnitude of the magnetizing flux it is possible to determine the produced back EMF of the machine, which is needed to determine the motor supply current and voltage when the winding scheme is selected.

The rotating speed and the supply voltage have to be matched with the machine flux. The relation between the voltage E_m and the air gap flux linkage Ψ_m is

$$E_\mathrm{m} = \frac{1}{\sqrt{2}}\omega k_{\mathrm{w}1} N_\mathrm{s} \widehat{\Phi} = \frac{1}{\sqrt{2}}\omega \widehat{\Psi}_m \qquad 2.4$$

where

- ω is the electrical angular frequency $2\pi f$, where f is the supply frequency
- $k_{\mathrm{w}1}$ is the fundamental winding factor and
- N_s is the phase winding turn number.

With the selection of these parameters, the already fixed pole number and the winding turn number can be selected. Guidelines for integer slot machines can be found in Table 2.5, which gives the possible combinations for different slot and pole configurations and phase winding turns for a given slot conductor number.

Table. 2.5. Allowed winding turn number and slot number for a slots per pole per phase q=1 winding with a given slot conductor number z_Q and a pole pair number. N_s is the number of series-connected coil turns in one phase.

p	q	z_Q					
	1	1	2	3	4	5	6
	Q	N_s					
1	6	1	2	3	4	5	6
2	12	2	4	6	8	10	12
3	18	3	6	9	12	15	18
4	24	4	8	12	16	20	24
5	30	5	10	15	20	25	30
6	36	6	12	18	24	30	36
7	42	7	14	21	28	35	42
8	48	8	16	24	32	40	48
9	54	9	18	27	36	45	54
10	60	10	20	30	40	50	60

The slot and pole combination can also be selected to produce a fractional slot winding. The fractional slot design can be used to produce shorter end windings for less leakage. An additional feature is the decreased axial dimension, which is an attractive property of this winding

technology. Fractioning can also reduce the machine inherent cogging torque, which is a characteristic feature of all full pitch windings. The fractional slot design also gives much more freedom in the selection of the pole and slot configuration. The end winding is at shortest when the pitch to the next slot is at shortest. The most common solution is a pitch of one or two slots. Fractional slot windings of q = 0.75, 1.125, 1.5 or 2.25 meet these criteria (Miller, 1994). The fractional slot windings of this kind can also be wound cost effectively with automatic winding machines. The drawback of the fractional slot design is the subharmonics that cause additional rotor losses and unbalanced magnetic pull in certain fractional slot arrangements. With the full pitch winding, the risk of a faulty design is smaller, and the cogging torque can be reduced by appropriate skewing.

With the selected p, q, z_Q and Q it is possible to determine the winding factors of the machine. The machine harmonic content can be varied by a suitable selection of these values. In motors, the back EMF is usually slightly lower than the phase supply because of the resistive losses in the stator. Before this, the winding arrangement has to be known to calculate the first harmonic coefficient for effective winding turns. For integer slot windings, the calculation of the winding factor is a rather straightforward task. The equation for determining the winding factor $k_{\mathrm{w}\nu}$ for a PM machine is

$$k_{\mathrm{w}\nu} = k_{\mathrm{d}\nu} k_{\mathrm{p}\nu} k_{\mathrm{sq}\nu} \tag{2.5}$$

where $k_{\mathrm{d}\nu}$ is the distribution factor defined by the slot angle and the number of slots per pole per phase, k_{p} is the pitch factor for short-pitched windings, which requires a two-layer winding, and $k_{\mathrm{sq}\nu}$ is the skewing factor for the rotor or stator skewing. The calculation of winding factor can be, written open as

$$k_{\nu\mathrm{w}} == \left[\frac{sin\,\nu\frac{\alpha_u}{2}}{q sin\,\nu\frac{\alpha_{\mathrm{u}}}{2}}\right]\left[sin\,\nu\frac{W}{\tau_{\mathrm{p}}}\frac{\pi}{2}\right]\left[\frac{\sin(\nu\frac{\alpha_{\mathrm{sq}\nu}}{2})}{\nu\frac{\alpha_{\mathrm{sq}\nu}}{2}}\right] \tag{2.6}$$

where

- α_{u} is the slot angle $p2\pi/Q$
- ν is the harmonic order
- q is the number of slots pre pole per phase
- W is the coil pitch
- τ_{p} is the pole pitch and
- $\alpha_{\mathrm{sq}\nu}$ is the applied skew angle of rotor or stator

The winding scheme can be used to shape the harmonic content of the produced current linkage wave. As q increases, the coefficient of the fundamental wave decreases, but at the same time, the harmonic effects are suppressed. For example, q = 2 decreases the 5^{th} and 7^{th} harmonics by 74.1 % in the distribution factor compared with the slots per pole and phase factor of q = 1.

Short pitching can also be used to decrease the harmonic content of the supply voltage. Short pitching of 4/5 of the pole pitch removes the 7^{th} harmonic almost completely, and the short pitching of 4/7 of the pole pitch suppresses the 5th harmonic. But as Table 2.5 shows, the slot number of the machines increases as a multiple of six in integer slot machines, and thus, the short pitching has to be a fraction of three or its multiple depending on the zone width. Hence, the closest short pitches to reduce the 7^{th} and 5^{th} harmonics are 5/6 and 2/3, respectively. The pitching effect on the harmonic content of the current linkage wave is presented in Fig. 2.2.

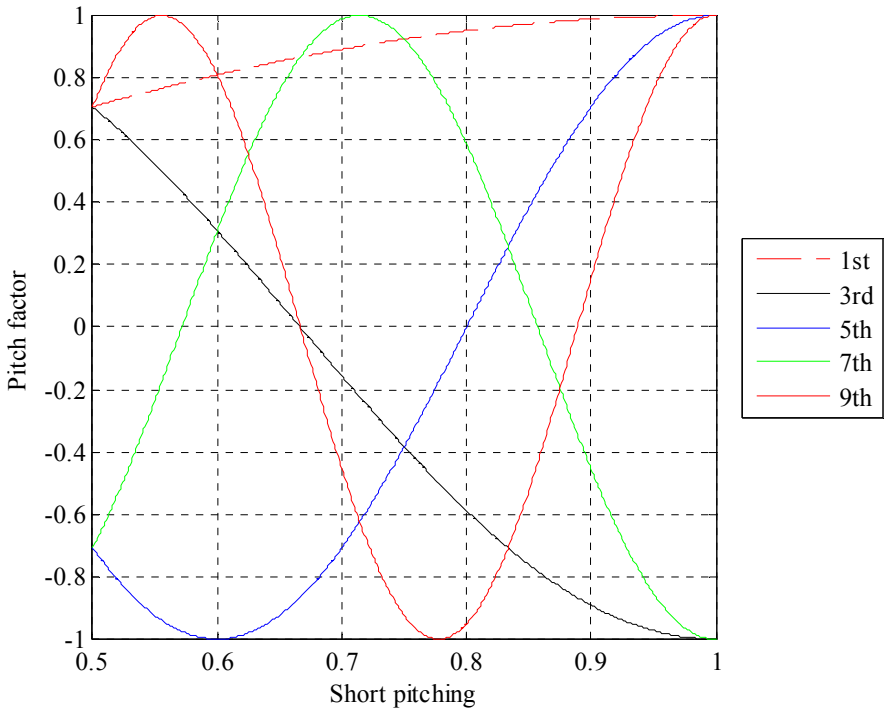

Fig. 2.2. Pitch factor as a function of short pitching for the 1^{st}, 3^{rd}, 5^{th}, 7^{th} and 9^{th} harmonics.

For scaling purposes, it is more beneficial to choose the slot number as a multiple of 12 for integer slot winding machines in order to have a larger selection of pole pairs. The right side of the table gives the winding turns per one phase of the machine with respect to the slot conductor number. However, as we can see, the selection for integer slot machines is quite limited. The skewing factor approaches unity when q increases and decreases as the slot number Q increases. The main function of the skewing is to alleviate the harmonic effects on the rotor surface.

Additional manipulation can be carried out with a parallel branching technique, which is especially useful in larger machines in order to provide low-voltage machine structures. With two parallel branches, the pole pairs can be separated to have the same number of slot conductors, which cuts

the required supply voltage to half and doubles the current drawn for the same rated power, or the slot per pole number can be increased to $2z_Q$ to maintain the original current rating. It has to be borne in mind that parallel connection may cause circulating currents as a result of geometrical asymmetries in the coils, which tend to be harmful to the machine. The principle of parallel branching technique is presented in Fig. 2.3.

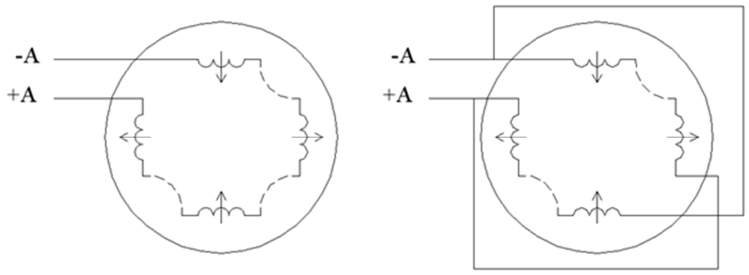

Fig. 2.3. Illustration of parallel branches. A series-connected winding (a=1) on the left; a winding with two parallel branches (a=2) on the right.

2.1.3 Magnetic circuit

After the determination of the winding scheme of the machine, the iron circuit dimensions have to be selected. The iron circuit dimensions also have an impact on the desired current density rating, since the determination of the yoke and teeth dimensioning has an effect on the slot area. The air gap flux density in Eq. 2.2 is used to determine the iron circuit dimensions.

The magnetic circuit, including the permanent magnet itself, has to consume the current linkage produced by the permanent magnet as Ampere's law states.

The flux density limit depends on the soft magnetic material used, but generally, the design limit for the electric sheet flux density is around 1.5 T or below the material-specific knee of the *BH* curve (Miller, 1994). Higher flux density values require a substantial increase in the current linkage because of the material saturation. However, to achieve the highest possible torque densities, the flux densities have to be brought to the material-specific limits.

Lower flux density values are advisable to gain head for flux boost in the iron circuit in order to enhance reluctance torque production. It is usually assumed that the flux flows completely through the tooth at a certain moment. Thus, the peak value of the flux density $\hat{B}_d$ in a tooth can be written, by neglecting the flux through a slot, which is a fair assumption if saturation does not occur, as follows

$$\hat{B}_{\mathrm{d}} = \frac{\tau_{\mathrm{u}} l'}{k_{\mathrm{Fe}} l' b_{\mathrm{d}}} B_{\delta} \tag{2.7}$$

where

- τ_{u} is the slot pitch and
- k_{Fe} is the filling factor of the iron core
- b_{d} is the tooth width
- l' is the effective stack length

which overestimates the flux density in the tooth area, because the flux is calculated for a surface limited by the slot pitch. The value must be corrected closer to the actual value by subtracting the flux flowing through the slot by assuming that the field strength at the boundary surface of iron is uniform with the slot opening area. Thus, the amount of flux density to be removed is

$$\hat{B}_{\mathrm{d,real}} = \hat{B}_{\mathrm{d}} - \left[\frac{\tau_{\mathrm{u}}}{k_{\mathrm{Fe}} b_{\mathrm{d}}} - 1\right] \mu_0 \hat{H}_{\mathrm{d}} \tag{2.8}$$

This can be solved with the *BH* curve of the electric sheet metal, or if the saturation limit is not close and the flux density is in the linear region of the *BH* curve, the field strength can be found by combining the two crossing lines as

$$\hat{H}_{\mathrm{d}} = \frac{\hat{B}_{\mathrm{d}}}{\mu_0 \mu_{\mathrm{r}} + \left[\frac{\tau_{\mathrm{u}}}{k_{\mathrm{Fe}} b_{\mathrm{d}}} - 1\right] \mu_0} \tag{2.9}$$

However, as stated above, this equation applies to flux densities below the knee of the *BH* curve. With the determined flux, the dimensions for the stator and rotor yoke can be calculated. The flux of the pole flows through two separate parts of the yoke, and thus, the thickness of the yokes can be determined

$$h_{\mathrm{y,rvs}} = \frac{\hat{\Phi}_{\mathrm{m}}}{2 k_{\mathrm{Fe}} l' \hat{B}_{\mathrm{y,rvs}}} \tag{2.10}$$

where the subscripts s and r denote stator and rotor, respectively. Now, to have a full description of the machine geometry, we only have to determine the slot dimensions of the machine. There are different geometries available depending on the winding types used. The exact dimensioning is easiest with technical drawing programs, but a wedge-type slot provides a practical choice for the initial guess. The wedge angle should be selected to get straight teeth in order to maximize the slot face area. Since z_{Q} and I_{s} are known, the slot height can be determined with the information about the desired current density J_{s} and the slot number Q_{s}.

$$h_{\mathrm{d}} = \frac{\left[\frac{I_{\mathrm{s}} z_{\mathrm{Q}}}{J_{\mathrm{s}} b_{\mathrm{u1}}} + \frac{b_{\mathrm{d}}}{2}\right] Q_s}{\pi} \tag{2.11}$$

The dimensions of the iron circuit can be determined backwards to fit the desired flux densities in the iron circuit by referring the magnetic voltages of one magnetic path to the current linkage of permanent magnets

$$U_{\mathrm{m}} = \oint \boldsymbol{H} \cdot d\boldsymbol{l} = H_{\mathrm{PM}} h_{\mathrm{PM}} \tag{2.12}$$

For the calculation of inductances and air gap magnetic voltages, the determination of the equivalent air gap is mandatory. The equivalent magnetic air gap length is somewhat larger in absolute value than the geometrical one, but since the air gap holds the greatest part of the magnetic energy of the magnetizing path, the evaluation of this parameter is important. The equivalent value of the air gap is necessary when determining the magnet height in the pole according to the desired air gap flux density fixed at the beginning of the machine design procedure. The Carter factor k_{C} can be expressed by

$$k_{\mathrm{C}} = \frac{\tau_{\mathrm{u}}}{\tau_{\mathrm{u}} - \kappa s} \tag{2.13}$$

where s is the slot opening width

and

$$\kappa = \frac{2}{\pi}\left[arctan\frac{s}{2\delta} - \frac{2\delta}{s}\log\sqrt{1 - \left(\frac{s}{2\delta}\right)^2}\right] \tag{2.14}$$

This gives an equivalent air gap length of

$$\delta' = k_{\mathrm{C}}\delta \tag{2.15}$$

This is the end of the basic design procedure as the basic geometry is fixed. The further development on the machine model is carried out by the finite element method to determine the magnet and pole area dimensions to achieve the desired flux.

2.2 Loss evaluation

The loss evaluation is one of the most difficult, if not the most difficult phenomenon to evaluate in a machine design process. The losses generated in an electrical machine can be divided into

- iron losses, which are a combination of hysteresis and eddy current losses,
- Joule losses, which are produced in the windings of the electrical machines,
- mechanical losses, which include friction losses, produced by the viscous forces acting on the rotor and stator surfaces, bearing losses and
- additional losses, which include for instance external fan losses and leakage losses.

In low- and medium-speed permanent magnet machines, the stator Joule losses are usually the most significant ones in size. In the normal speed range, the proportion of friction losses and stator core losses of the total losses vary in size depending on the machine size. Rotor losses are usually quite small, but as a result of the magnet sensitivity to temperature, this loss component is equal in importance to the stator Joule losses in order to achieve a safely operating machine structure.

2.2.1 Joule losses

The Joule losses in the stator copper are the easiest ones to predict as the only winding arrangement in a permanent magnet machine is the armature winding. The Joule losses follow the general rule for heat dissipation in a resistive medium affected by current as

$$P_{\text{Joule}} = R_{\text{AC}} I^2, \tag{2.16}$$

where R_{AC} is the alternating current resistance of the conducting circuit, and I is the RMS current affecting the conducting path.

The alternating current resistance depends on the winding arrangement and the supply frequency. The two different mechanisms that increase the AC resistance value are the skin effect and the proximity effect. In the skin effect, the increasing supply frequency causes the current to concentrate closer to the conductor surface, which increases the Joule losses as the effective conductor area decreases. In the proximity effect, the currents of adjacent coils repel or attract each other depending on whether the flow direction is the same or opposite, respectively.

According to (Vogt, 1983), the free-space skin effect can be evaluated by

$$\delta_{\text{skin}} = \frac{1}{\sqrt{\pi f \mu_{\text{r}} \mu_0 \sigma}}\ , \tag{2.17}$$

which determines the depth at which the current density is decreased to e^{-1} of the current density on the conductor surface. The skin effect for copper is presented in Fig 2.4.

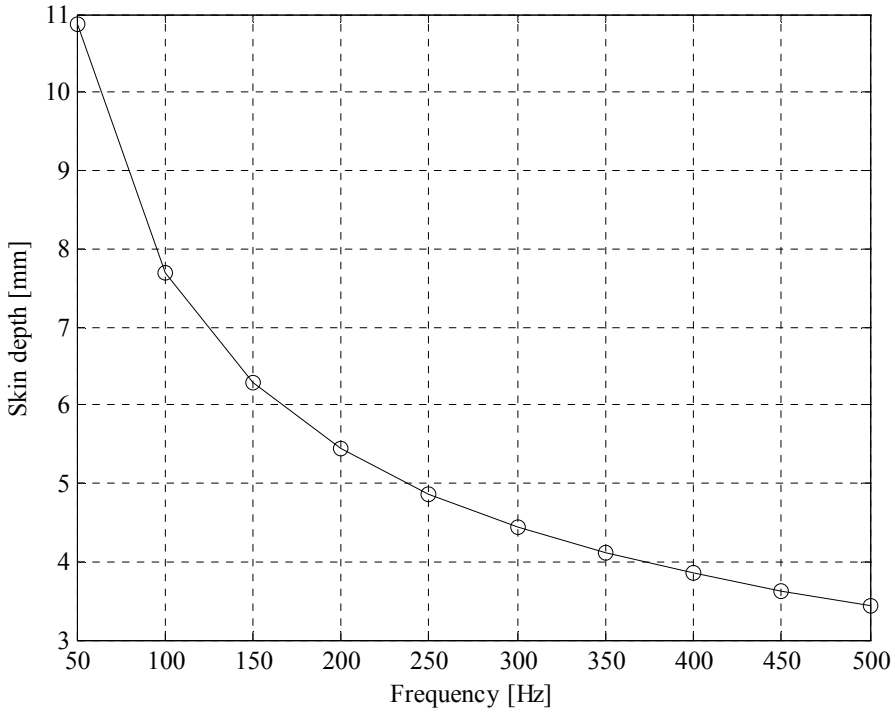

Fig. 2.4. Indicative copper skin depth as a function of frequency in free space. The copper conductivity is $5.97 \cdot 10^7$ S/m.

In an electrical machine, the coils are inside a high-permeability electric sheet, which causes the flux linkage path to travel differently compared with a free space. With a large coil cross-sectional area, the flux linkage tends to concentrate close to the slot opening area. The evaluation of the AC resistance level is more important in large form-wound machines and at high frequencies. Smaller machines benefit from random-wound coils, which naturally produce a thread mixing in the coils, and smaller coil cross-sectional areas. The AC resistance value can be decreased by special winding materials such as multi-threaded Litz wires or form-wound Roebel bars. Special winding techniques such as coil mixing and twisting are also useful (Hämäläinen, 2009).

Copper and aluminum are the most common conductor materials in electrical machine windings. Because of the heating of the material, the resistance value must be treated with a temperature-related coefficient α_T, which depends on the winding material, because the winding temperatures easily reach the value of 150 °C and above. Temperature coefficients of resistivity for different metals are presented in Table 2.6.

Table. 2.6. Temperature coefficients of resistivity for metals typically used in electrical machines.

Medium	ρ[Ωm]	α_T [%/°C]
Copper	$0.0168 \cdot 10^{-6}$	$3.9 \cdot 10^{-3}$
Aluminium	$0.028 \cdot 10^{-6}$	$4 \cdot 10^{-3}$

The corrected formula for the DC resistance is thus

$$P_{\text{Joule}} = R_{\text{DC},20°\text{C}}\big(1 + \alpha_{\text{T}}(T_2 - T_1)\big)I^2 \qquad 2.18$$

Since the temperature differences in electrical machines are moderate, a couple of hundred degrees at maximum, the use of a constant temperature coefficient is justified. In reality, the temperature coefficient is not linear, but the accuracy is nevertheless usually more than enough for engineering applications. For example, the resistivity temperature coefficient of copper follows the equation

$$R_{2\text{Cu}} = \frac{1}{233.54 + T_2} R_{1\text{Cu}} \qquad 2.19$$

Thus, the temperature coefficients for 273.15, 293.15 and 393.15 K are 0.00428, 0.00394 and 0.00300, respectively. Eq. 2.19 is valid for temperatures above 73.15 K.

Since the Joule losses are proportional to the second power of the current, the equation forms the basis for understanding how high-efficiency machines should be built. A good principle in electrical machine design, at least for moderate power ratings, is to keep the Joule losses less than or equal to the iron losses. It usually helps in keeping the efficiency high, even at low operating speeds.

Joule losses are also generated in permanent magnets, because of induced current harmonics. There are numerous approaches to analytically estimate Joule losses in a PM material; however, complex pole structures require a finite-element-based approach. Embedding of the magnets reduces the effects of current harmonics on the magnets, because rotor laminations damp the flux density variations before they reach the magnets. In the surface magnet design there is no such protection, and different techniques have to be applied if necessary. Magnet slicing has proved to be a useful technique (Polinder et al., 1997), and it can be implemented either in the axial or tangential direction.

2.2.2 Iron losses

Iron losses are probably the most complex loss component of all. The foundations of the loss evaluation in an iron core were laid originally by C.P Steinmetz in *On the law of Hysteresis* in 1892. According to (Steinmetz, 1984), iron losses can be evaluated by an analytical equation

$$W_{\mathrm{Fe}} = \kappa_{\mathrm{h}} \hat{B}^{1.6} + \kappa_{\mathrm{e}} f \hat{B}^2, \tag{2.20}$$

where

- κ_{h} is the hysteresis coefficient,
- κ_{e} is the eddy current coefficient,
- f is the affecting frequency and
- $\hat{B}$ is the peak value of flux density in the material.

The equation describes how much energy is lost per cycle in the material. The power loss can be obtained by multiplying the Eq. 2.20 by frequency. The equation implies that the losses are proportional to the area inside the hysteresis loop. The hysteresis loop defines the maximum flux density limits for given field strengths ending to a certain value in both of the odd quadrants, which are the saturation limits for the magnetic flux density. Although this equation is quite a robust approach, it gives a generalized idea of the phenomenon in the material. According to the Steinmetz equation, the hysteresis losses are proportional to a material-specific hysteresis constant, and the applied flux density to a certain power, which varies between 1.6 and 2 in the literature. The latter part presents the eddy current losses in relation to a certain eddy current factor and to the frequency of the phenomenon. Many other attempts to determine the magnitude of core losses have been presented ever since. A modernized version of iron loss hand calculation relies on the material data provided by electric sheet manufacturers. In (Vogt, 1983), the equation for iron losses is given in the form

$$P_{\mathrm{Core}} = m_{\mathrm{Fe}} \kappa_{\mathrm{u}} \upsilon_{\mathrm{u1.5}} \left(\frac{\hat{B}_1}{1.5} \right)^2, \tag{2.21}$$

where

- $\upsilon_{\mathrm{u1.5}}$ is the specific total loss of the material at 1.5 T and the frequency under observation [W/kg],
- m_{Fe} is the core mass and
- κ_{u} is the geometry-related coefficient given in Table 2.7.

The loss formulation $\kappa_{\mathrm{u}} \upsilon_{\mathrm{u1.5}}$ can be replaced by a more extensive formula, which describes the harmonic hysteresis losses and the eddy current losses separately

$$\kappa_{\mathrm{u}} \upsilon_{\mathrm{u1.5}} = \upsilon_{\mathrm{h1,5}} \kappa_{\mathrm{h}} \left(\frac{f_{\mathrm{s}}}{50} \right) + \upsilon_{\mathrm{e1,5}} \kappa_{\mathrm{e}} \left(\frac{f_{\mathrm{s}}}{50} \right)^2 \tag{2.22}$$

where

- κ_h is the hysteresis coefficient,
- κ_e is the eddy current coefficient,
- $v_{h1,5}$ is the hysteresis core loss component [W/kg] and
- $v_{e1,5}$ is the eddy current core loss component [W/kg].

Table. 2.7. Geometry-related core loss coefficients for Eqs. 2.21 and 2.22 (Vogt, 1983).

Machine type	Teeth	Yoke			
	κ_u	κ_h	κ_e	κ_e	κ_u
Synchronous machine	2.0	1.5	1.8 (p=1)	2-2.2 (p>1)	1.55-1.7
Asynchronous machine	1.8				
DC machine	2.5	1.5	2.5		-

In Eqs. 2.21 and 2.22, the specific total loss of the material is usually provided by the sheet manufacturer. However, the specific total loss can be fitted to the existing manufacturer data. For example, M270-35A by Surahammars Bruks has specific losses according to Table 2.8.

Table. 2.8. M270-35A specific loss data according to the Surahammars data sheet.

B	Specific loss [W/kg]			
	50 Hz	100 Hz	200 Hz	400 Hz
0.10	0.030	0.040	0.090	0.210
0.20	0.070	0.160	0.370	0.920
0.30	0.130	0.340	0.790	1.990
0.40	0.220	0.550	1.310	3.330
0.50	0.310	0.800	1.910	4.940
0.60	0.430	1.060	2.610	6.840
0.70	0.540	1.380	3.390	9.000
0.80	0.680	1.730	4.260	11.40
0.90	0.830	2.100	5.230	14.20
1.00	1.010	2.510	6.300	17.30
1.10	1.200	2.980	7.510	20.90
1.20	1.420	3.510	8.880	24.90
1.30	1.700	4.150	10.50	29.50
1.40	2.120	4.970	12.50	35.40
1.50	2.470	5.920	14.90	41.80
1.60	2.800	-	-	-
1.70	3.050	-	-	-
1.8	3.25	-	-	-

Equation 2.29 can be fitted to the existing data in Table 2.8 by selecting the hysteresis and eddy-current components $v_{h1.5}$ and $v_{e1.5}$ as 1.50 and 0.97 W/kg, respectively. The additional eddy current coefficient needs a value of its own for each frequency. The best fitting is achieved with the coefficient values 1.0, 0.7, 0.6, and 0.5 for the frequencies 50, 100, 200 and 400 Hz, respectively. The fitting results are presented in Fig. 2.5.

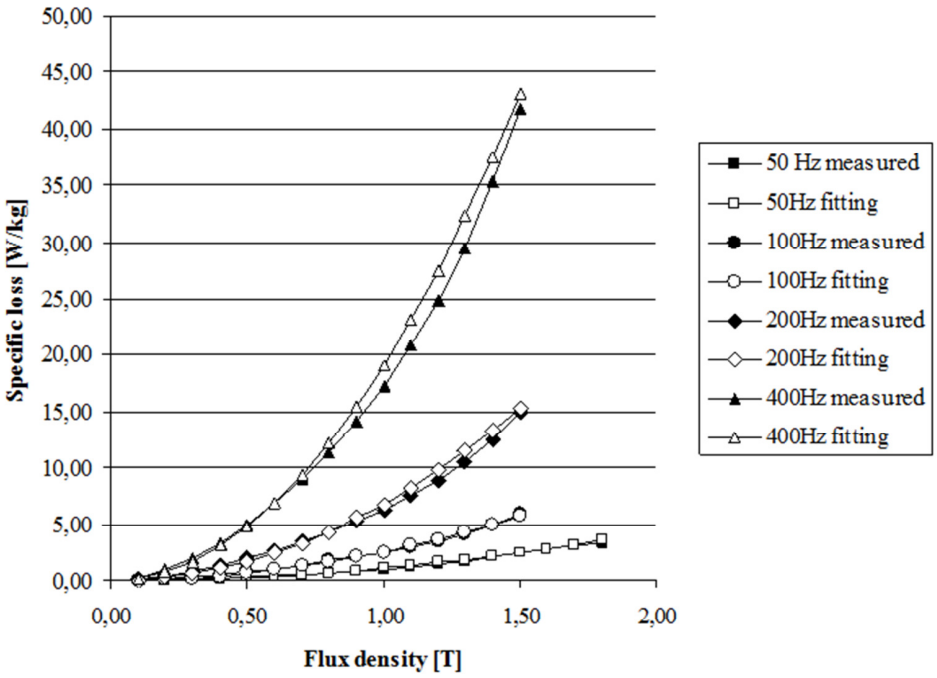

Fig. 2.5. Specific losses of M270-50A according to Table 2.8 data fitted with the core loss coefficients of Table 2.7.

In the case of known harmonic content in the flux density, the material-specific constants κ_e can be calculated more accurately by the equation

$$\kappa_e = \frac{\sum_1^\infty n\hat{B}_n^2}{\hat{B}^2} \qquad 2.23$$

Equation 2.23 can be used together with the finite-element-based design programs. A similar approach has also been presented in (Pyrhönen et al., 2008) for the total core losses by equation

$$P_{Fe} = \kappa_{h,e}\hat{B}^2 m_{Fe} \qquad 2.24$$

where $\kappa_{h,e}$ is the material-specific total loss per kg, including hysteresis and eddy currents, and m_{Fe} is the mass of the iron circuit. The equation can be used to determine losses in each individual part

of the machine, but the problem is that the value $\kappa_{h,e}$ determined by the material manufacturer is valid only for sinusoidally varying flux densities. This problem is usually solved by using empirically determined loss coefficients presented in Table 2.9.

Table. 2.9. Core loss coefficient $\kappa_{h,e}$ according to the machine type for Eq. 2.31.

Machine type	Yoke	Teeth
Synchronous machine	1.7–2.5	1.5–1.8
Asynchronous machine	1.7–2.5	1.5–1.8

Approaches to analytically solve eddy current and hysteresis losses are numerous. Common to all these is that the equations are more or less based on the classical definitions for eddy current and hysteresis losses presented above. The problem is that with the modern frequency-converter-fed systems, the loss evaluation and material properties are not accurate for classical equations. Experimental studies have shown a significant increase in core losses with the PWM excitation (Tutkun, 2002), (Boglietti et al., 1991), (Boglietti et al., 2003) . The actual power dissipation in frequency converter drives is considerably higher than for the pure sinusoidal waveform case owing to the harmonic waves in the supply current waveform. The current causes the same distortion to the flux produced in the coils, and thus, increases the amount of induced iron losses. To minimize the PWM effect, the modulation index should be close to unity and the switching frequency above 5 kHz (Boglietti et al., 1993), (Boglietti et al., 1995).

2.2.3 Contact friction losses in bearings

The bearing losses can usually be determined, depending on the application and bearing type, by the information provided by the manufacturer. Some manufacturers, such as SKF, provide analytical tools for the rotating loss evaluation of bearings. The following analysis of the bearing friction losses is based on ball bearing structures, because single-row deep groove ball bearings are the most common bearing type used in electrical machines.

For bearing loads less than 10 % of the allowed dynamical loading, in normal operating conditions and with sufficient lubrication, the rotating friction losses of a bearing can be estimated by

$$P_{\text{fricton}} = 0.5 \Gamma \zeta D_{\text{B}} \Omega \qquad 2.25$$

where

- Γ is the equivalent bearing load [N],
- D_{B} is the bearing bore diameter [m],

- ζ is the constant friction coefficient for bearing according to Table 2.10 and
- ω is the angular velocity of the bearing.

Table. 2.10. SKF friction coefficients for non-sealed bearings [SKF, 2012].

Bearing type	Friction coefficient ζ
Deep groove ball bearing	0.0015
Angular contact ball bearing single\ double row	0.0020 / 0.0024
Self-aligning ball bearings	0.0010

2.2.4 Additional losses

Additional losses are electromagnetic losses that are not included in the iron and Joule losses. The additional loss generation originates from the leakage terms, which cause second-order loss components in the machine structures. Depending on supply current and its harmonic content, additional losses can be grouped to

- Additional no-load losses that are caused by flux variations in the main flux caused by the stator and rotor permeance variations and
- additional load losses that result from the combined effect of the current linkage waveform and the machine leakage components.

Both groups generate high-frequency surface losses in the annulus area. The difference is that the majority of the no-load surface losses are concentrated on the rotor surface. Loss generation is strengthened by added skewing. The relative motion between the rotor and the stator also generates additional losses in the teeth iron as a result of the main flux pulsation. Load-oriented leakage fluxes react in the same way. Load-oriented losses are also generated in the stator windings because of the slot leakage component. In addition, the end-winding leakage component interacts with the stator core ends and the machine end space structural parts thereby generating losses.

There is no direct and accurate method to determine the additional losses of a machine. However, the IEC standard EN 60034-2 determines that the additional losses are from 0.1 to 0.2 % of the input power for salient pole synchronous machines and from 0.05 to 0.15 % for non-salient pole synchronous machines.

2.3 Heat transfer

Understanding of the heat transfer and the loss generation mechanisms is essential in electrical machine design. The increasing demand for high-efficiency electrical machines requires a careful design process to achieve low material consumption and a high torque density. The design process of high end electrical machines involves an increasing amount of consideration of the mechanical and thermal stresses in the machine. This development is emphasized by the fact that electrical drive systems are expanding to different applications. One major driving force has been the electrification of power transmission in moving machines, vehicles and vessels.

The design of the electrical circuit is a small part of the design process, even though it requires a complicated iteration process as electrical machines are nowadays designed to be application-specific rather than general purpose machines.

2.3.1 Fundamentals of heat transfer

The general theory recognizes three different heat transfer methods: radiation, convection and conduction. In electrical machines, the two latter methods are the most important ones. Heat transfer by radiation is usually neglected, but it should be taken into account if significant temperature differences are expected on the radiating surfaces, because the radiation heat transfer is proportional to the fourth power of the absolute body temperature. Conduction is probably the most important heat transfer method due to the fact that electrical machines are built mainly of metallic materials, which are known for their good heat transfer properties. However, the insulation materials limit the heat transfer from the electrical machine to the surrounding medium. The importance of convection in the total heat transfer process increases as the rotating speed grows and/or if a forced convection method is applied to the system.

The heat transfer is defined comprehensively by the four laws of thermodynamics. In the design of electrical machines, the first and second law are of most importance.

The first law of thermodynamics states that the energy of a system can be changed by work done on or by the system or by applying a heat flow through the system boundaries. The work done by the system can be divided into different parts: mechanical work and work done by the system boundaries (e.g. pressure change).

The second law, which states that entropy increases over time, means that the heat always flows from a hotter body to a colder body. The study of the thermal behaviour of materials is based on the heat transfer equation, which is known as the Fourier equation.

The usual method in the thermal modelling is to apply a thermal network to a specific geometry for steady-state operation. The model can be further improved by the introduction of a thermal capacitance matrix, which enables a dynamic study of the system. The networks are usually simple and fast to solve. This is mainly due to the simplification of the geometric parameters and composition of larger entities. Another method is to use commercial programs such as Flux™ or

MotorCad™ by Cedrat for the evaluation of the thermal behaviour of the machine. The commercial programs would be suitable for this purpose, but they are not always available and include some generalizations that cannot be changed.

Even though the commercial programs are more accurate than analytical models, at least to some extent, there are major simplifications in both of the methods.

- The orientation of the motor is usually in the axial direction in the 2D plane, because the main thermal path is considered to be radial.
- Heat transfer is considered uniform in the radial direction.
- Radiation is usually neglected.
- Physical properties of materials are considered isotropic.

Thermal networks are usually built such that the geometry is considered as a two-dimensional plane with the exception of the windings. The temperatures are thus averaged, and the total heat behaviour is generalized. To increase the resolution of the thermal behaviour, the node number has to be increased. Hence, the implementation of the grid and calculations become arduous. Some automated routines should thus be performed. When increasing the accuracy of the system, it is not reasonable to calculate the machine geometry as a whole. Similarly as in magnetic calculation, one pole pitch is usually enough for the determination of thermal properties. To understand the mechanism of heat transfer in more detail, it is necessary to know the basic laws of thermodynamics and the main heat transfer methods.

2.3.2 Conduction

Conduction is the heat transfer method that transfers energy from a higher potential to a lower potential in order to reach an equilibrium state of an equal potential level. On a microscopic scale, conduction is the heat transfer method inside solids, liquids and gases. The molecular motion causes a convection phenomenon in liquid and gaseous materials, but the heat transfer between individual particles takes place in the form of conduction heat transfer.

The conduction heat transfer can be expressed in numerous ways. An engineering approach is provided by rate equations, which are used to determine the amount of energy transferred in a certain time. For heat conduction this is known as Fourier's law. For one-dimensional heat flow it yields

$$q''_{\mathrm{x}} = -k\frac{dT}{dx} \tag{2.26}$$

where q''_{x} is the heat flux density [W/m^2], which is proportional to the thermal conductivity k and the temperature difference ΔT and inversely proportional to the travelled distance Δx in the x-

direction. Equation 2.32 is the basis of the heat conduction calculations. The equation can be extended to a more general form, but in engineering calculations, which usually involve a lumped-parameter technique in thermal conduction solutions, the one-directional plane equation is more useful. Table 2.11 presents thermal conductivities of common engineering materials.

Table. 2.11. Thermal characteristics of common engineering materials (Incropera, 2007).

Material		k [W/m^{2}K] (at 300K)	k [W/m^{2}K] (at 400K)
Carbon steels	Mn ≤ 1.0 % Si ≤ 0.1 %	60.5	56.7
	1.0% ≤ Mn ≤ 1.6 % 0.1 %< Si ≤ 0.6 %	51.9	49.8
	Mn ≤ 1.0 % 0.1 %< Si ≤ 0.6 %	41	42.2
Stainless steels	AISI 302	15.1	17.3
	AISI 316	13.4	15.2
Aluminium	2024-T6	177	186
Cold-rolled electric sheet		20-30	-
Copper	Industrial grade	360-386	-
Water		0.613	0.688 (2.445 bars)
Air		$22.3 \cdot 10^{-3}$	$33.8 \cdot 10^{-3}$
Silicon paste		1	-
Silver paste		> 220	-
Polyester resin		0.15–0.20	-
Epoxy resin		0.3–0.6	-
Glass fibre		0.2	-
Carbon fibre		0.5	-

2.3.3 Radiation

Radiation is the only heat transfer method that does not require any medium for heat transfer. The radiation heat transfer is electromagnetic radiation, the wavelengths of which vary between 0.1 and 100 μm. The wavelength range includes visible light and the infrared region, and additionally, the low-frequency ultraviolet region. The absorbed radiation heat depends on the material and the material surface properties. In electrical machines, the reflective surface can be assumed opaque, which means that part of the radiation is absorbed and part is reflected. The reason for this is that no real material can completely absorb radiation heat, but part of the heat is always reflected. Thus, there is an absorption factor β, which is a reference of the medium absorption to an ideal black body, which completely absorbs the heat exposed. The sum of radiation heat absorbed and reflected by an opaque medium is unity.

$$\beta + \eta = 1 \qquad 2.27$$

where

- β is the absorption factor and
- η is the reflection factor

Since absorptivity depends on the specific wavelength, it is not applicable to solid surfaces of electrical machines, which radiate in a wide frequency range. Thus, a wavelength independent coefficient called relative emissivity, denoted by ε_r, is introduced. This is a general engineering assumption and it is known as 'grey body assumption'. In addition to this, the surfaces are usually considered diffuse, which means that the absorptivity and emissivity do not depend on the angle of radiation.

With these assumptions, the radiation heat transfer between solid surfaces is given by the Stefan-Boltzmann equation

$$q = \varepsilon_r \sigma \left(T_{\text{emissive}}^4 - T_{\text{absorptive}}^4 \right) \tag{2.28}$$

where

- ε_r is relative emissivity and
- $\sigma = 5.67 \cdot 10^{-8}$ Wm^{-2}K^{-4} is the Stefan-Bolzman constant.

The relative emissivity is a combination of the absorptive surface and emissive surface emissivities and the surface areas according to

$$\varepsilon_r = \frac{1}{\frac{1}{\varepsilon_{\text{emissive}}} + \frac{S_{\text{emissive}}}{S_{\text{absorptive}}} \left(\frac{1}{\varepsilon_{\text{absorptive}}} - 1 \right)} \tag{2.29}$$

where

- $\varepsilon_{\text{ansorptive}}$ is the emissivity of the absorptive surface,
- $\varepsilon_{\text{emissive}}$ is the emissivity of the emissive surface,
- $S_{\text{absorptive}}$ is the area of the absorptive surface and
- S_{emissive} is the area of the emissive surface.

In the case of electrical machines, radiation can usually be neglected if the temperature differences between surfaces are within less than a couple of hundred degrees.

2.3.4 Convection

Convection is a special case of conduction heat transfer, since the heat transfer between particles takes place by conduction. Convection always needs a fluid medium. Without a fluid, convection cannot take place. The fluid can be either a gas or a mix of gases or liquids. The difference in

conduction is that the particles are moving. Convection can be divided into two subcategories, which are forced and natural convection. In forced convection, extra work is applied to move the fluid.

The mathematical description of fluid movement is challenging owing to the complex nature of fluid mechanics. Consequently, the equation used for convection heat transfer is usually a result of experimental studies. Experimental equations have to be used with care, because the equations only apply to a certain degree, and the boundary values are usually quite narrow. Inaccuracies in the system parameter definitions also have a significant effect on the results. The efficiency of convection is described by the Nusselt number *Nu*, the proportion of the convection heat transfer to the conduction heat transfer in a fluid, by equation

$$Nu = \frac{\alpha l}{k} \tag{2.30}$$

- where k is the thermal conductivity of fluid,
- α is the convection coefficient and
- l is the characteristic length of the surface affected by the convection.

The convection coefficient α describes the heat dissipation of a material for a unit area at a certain temperature difference. A higher Nusselt number indicates that heat is removed rather by convection than by conduction. Convection coefficients for different fluids and convection methods are presented in Table 2.12.

Table. 2.12. Thermal conductivities k and convection coefficients of typical engineering fluids. The lower values are for a 0.2 m/s velocity and the higher values for a 20 m/s velocity. The values are for flat plate convection and a 0.1 m long surface.

Fluid (280K)	k **[W/m·K]**	α **[W/m^{2}K]**
Water	0.680	400–28000
Air	0.0303	2–77
Ethylene Glycol	0.261	12–120
Engine oil	0.136	167–1700

As described above, convection can be divided into two categories. Independent of the method used, the flow type can also be divided into laminar and turbulent flow. These depend on the geometric properties of the surface and the speed of the fluid, but in any case, the distinction between laminar and turbulent flow is expressed by the Reynolds number, which describes the proportion of the fluid density to the viscosity of the fluid. Fluids with low viscosity and high density, such as water and other low-viscosity liquids, are susceptible to turbulent flow characteristics, and are therefore suitable for cooling applications.

Prandtl number is the third major dimensionless number in the convection heat transfer. Prandtl number describes the proportion of the speed boundary layer to the thermal boundary layer, which means that as the fluid advances along the surface, the temperature of the fluid rises at the same

height of examination. The thermal boundary layer stops in a point where no heat transfer occurs in the normal direction of the surface. The thickness h_t of this surface is determined by the equation

$$h_t = \frac{(T_s - T)}{(T_\infty - T_s)} \tag{2.31}$$

where T_∞ is the temperature of the terminal boundary layer that is considered to be the average temperature between the surface temperature and the ambient temperature in practical calculations. T_s is the temperature of the body surface, and T is the temperature of the boundary layer at the height h_t. The thickness at which the thermal gradients occur is usually considered $h_t = 0.99$.

2.3.5 Lumped-parameter model

Compared with the electrical and mechanical design methods, the thermal modelling is a rather recent approach in the machine design process. Some general guidelines for the thermal dimensioning of electrical machines have been given in the 1990s in (Saari, 1995), (Kylander, 1995), (Mellor, 1991) and (Lindström, 1999) with lumped-parameter models. A more detailed analysis of permanent magnet machines has also been given by (Liu, 1993), (Grauers, 2004) and (Mellor, 1991). The general method for the thermal evaluation of electrical machines is the lumped-parameter method, which can be described by the matrix equation

$$\mathbf{\Delta T = G^{-1} P}, \tag{2.32}$$

according to which the temperature difference $\mathbf{\Delta T}$ of the machine is directly proportional to the inverse of the thermal conductance square matrix **G** and the heat dissipation single-row matrix **P**. The matrix can be presented as a thermal network as shown in Fig 2.6.

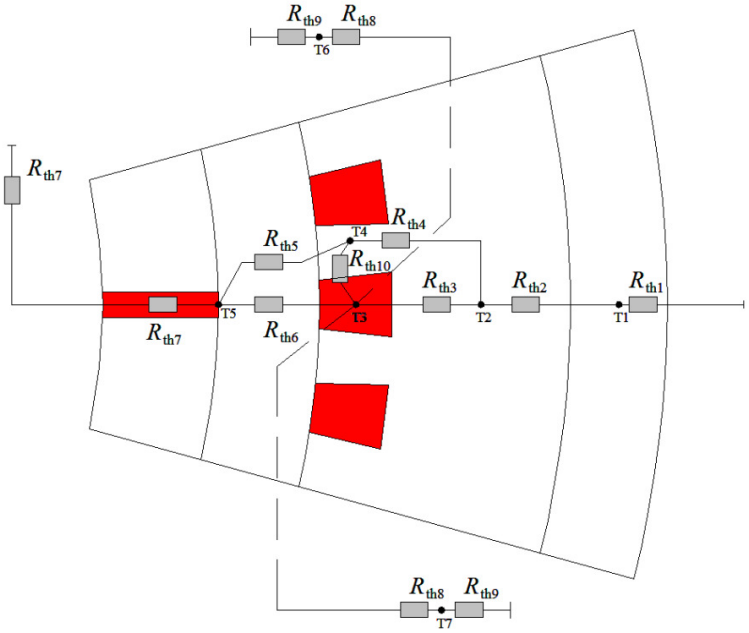

Fig. 2.6. Typical thermal network layout fitted to the machine geometry.

By inserting the sum of related thermal conductances, that is, the incoming branches, of a nodal point into a corresponding element in the conductance matrix and by inserting the thermal conductances of individual leaving branches into a corresponding element of the next and previous nodal point, a lumped-parameter network is produced. The pattern can be given as a series function

$$G = \begin{bmatrix} \sum_{i=1}^{n} R_{1,\mathrm{i}}^{-1} & \cdots & -R_{1,\mathrm{n}}^{-1} \\ \vdots & \ddots & \vdots \\ -R_{\mathrm{n},1}^{-1} & \cdots & \sum_{i=1}^{n} R_{\mathrm{n,i}}^{-1} \end{bmatrix} \tag{2.33}$$

The easiest way to carry out the modelling is to apply simplified geometries. Cylindrical elements can be evaluated by the equation

$$R_{\mathrm{cylinder}} = \frac{\log\left(\frac{r_{\mathrm{out}}}{r_{\mathrm{in}}}\right)}{2\pi k l_{\mathrm{cylinder}}} \tag{2.34}$$

The cylindrical element can be used to model the radial thermal resistances of the rotor and stator yokes. The cylindrical elements can also be used to model the tooth area; however, trapezoid and square blocks are useful in the modelling of non-cylindrical parts, such as slots, teeth and magnets. Equations for trapezoidal and square element types are

$$R_{\text{trapezoid}} = \frac{h}{k\left(\frac{w_1+w_2}{2}\right)l_{\text{trapezoid}}} \text{ and} \tag{2.35}$$

$$R_{\text{rectangle}} = \frac{h}{kw_{\text{rectangle}}l_{\text{rectangle}}}, \tag{2.36}$$

respectively.

More complex equations can be used to describe the medium in more detail, but the accuracy achieved this way is usually lost in the convection modelling, because the accuracies of the correlation equations are quite low.

2.4 Summary of the key design areas

Electrical machine design is a challenging task, which requires control over multiple parameters and understanding of the relations between the design areas. Traditional analytical methods are useful in narrowing down the options of the base design, even though the traction machine design differs from traditional industrial machine designs.

As a traction application does not necessarily have a specific operating point, the traditional guidelines for machine design cannot be directly applied to a traction machine design. Thus, the balance between the electromagnetic design, heat transfer and loss generation becomes more important.

3 Implementation of the design methods

The principles of electrical machine design presented in the previous chapters have been implemented to two prototype machine structures within the application-specific limits. This chapter presents two salient pole structures, one with a special magnet module (MM) structure and one with an embedded magnet (EM) structure designed for a vehicle propulsion system. The electromagnetic design process is presented in detail along with the transient and steady-state analysis of the machine performance.

3.1 Background of the machine development

PM technology was selected, because PM machines can be built with a high pole number to achieve a light and volume-efficient design. The machine was intended to be connected to the tyre with a drive shaft as presented in Fig. 3.1.

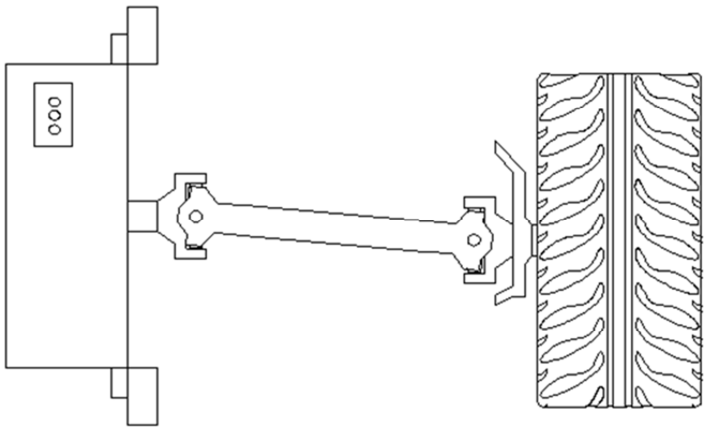

Fig. 3.1. Electrical machine connection to a wheel in the direct drive propulsion system.

The allowable machine voltage and current ratings lead to about 300 V line-to-line voltage (214.5–414.7 V) and 300 A line current limits as a result of the battery package limitations set by the Metropolia design. In the machine design process, the field weakening region was limited to about 50 % with a flat battery. The rotating speed corresponding to the maximum available voltage was selected by the desired maximum speed of 200 km/h. With the selected tyres, the rotating speed required for the maximum speed is about 2000 min^{-1} giving a 0.15 V/min voltage to rotating speed ratio.

The average torque and rotating speed were taken from a drive cycle of a specific sports car track data given by Metropolia, which yielded an average power of 25 kW at 1000 min^{-1}. This was set as the basis of the machine dimensioning. For the rated power of 25 kW, the voltage rating results in a ~100 A line current at the 1000 min^{-1} rotating speed.

The high pull-out torque was a matter of concern from the beginning of the design process. Because of the limiting values of the energy source, the maximum output power from the battery is about 400 kW. As the vehicle was intended to be equipped with four machines, one for each tyre, the maximum input power for one machine was about 100 kW. With these initial data, the design values for the electrical machine were given as follows:

- nominal torque 240 Nm,
- nominal speed 1000 min^{-1},
- maximum torque 1000 Nm,
- maximum speed 2000 min^{-1},
- light in weight, the mass limit 38 kg for the active parts,
- water cooling in the stator frame,
- length limit for the active parts 200 mm and
- diameter limit for the active parts 380 mm.

The dimension limits are based on the actual space available in the car chassis. The actual space is somewhat larger, but the dimensions of the active parts are scaled down to accommodate the water-cooled machine frame in the available chassis space.

The design process started by analytical calculations, and with the axial space limitation, it was obvious that the magnetic structure of the machine is going to be short compared with the physical diameter. For a water-cooled frame, the current density may vary between 4–7 A/mm^2 (Vogt, 1983). An air gap flux density value of 0.8 T and a linear current density of 45 kA/m were decided to be used as the ground values for the electrical design process, resulting in a 36 kPa tangential stress component. The low values of the linear current density allow high torque operation. Thus, loading of the machine in nominal operation is quite easy. The magnetic circuit design was made loose enough to allow space for flux boost in order to get the highest benefit from the reluctance torque component at the lowest speed.

The length of the machine active part was set to 65 mm. The end space required for traditional three-phase integral slot windings in the axial direction is close to the pole pitch of the machine. With the rotor outer diameter of 284 mm, the pole pitch is about 56 mm, which yields a total active part length of 177 mm. These dimensions provide enough rotor surface area to produce 240 Nm of constant torque at the 36 kPa tangential stress and a peak torque of about 110 kPa. The axial length of the rotor is short, because the rest of the space is needed for the end windings. The rotor area required for the torque output is produced by increasing the rotor diameter.

To make the stator and the related stator structure light, the machine was decided to be built with a high pole number. A high pole number allows a light iron core, because the number of flux paths for the main flux increase linearly as the pole number increases. As the core dimensions are scaled

down, a larger rotor can be fitted into the same space than in the case of small pole numbers, which means a larger torque capability as the rotor area increases. The increase in the pole number also promotes pull-out torque production as the pull-out torque is directly proportional to the second power of the pole pair number, as can be concluded from Eqs. 1.2 and 1.5–1.7.

The rotor diameter and the 380 mm limit of the stator stack result in a 48 mm space for the stator stack and the air gap in the radial direction. The lowest pole number to fit the stator geometry inside the specified dimensions and to allow sufficient slot dimensions is $2p = 16$. This yields a slot pitch of 18.8 mm for $q = 1$ which results in 48 slots in the stator. The guide values for a suitable slot pitch of a synchronous machine are between 8 and 25 mm (Vogt, 1983). To ensure safe operation in the maximum speed conditions, it was decided to use low-loss M270-50A grade sheet metal for the iron cores of the rotor and the stator.

The machine winding was chosen to be a two-layer winding to achieve short end windings. It was noted that this can lead to problems with the torque ripple caused by the current linkage harmonics especially at high current ratings. The one slot per pole per phase configuration results in a slightly coarse back EMF waveform, but because the machine is intended for automotive usage, the torque vibrations are acceptable, at least to some degree. The winding configuration is illustrated in Fig. 3.2.

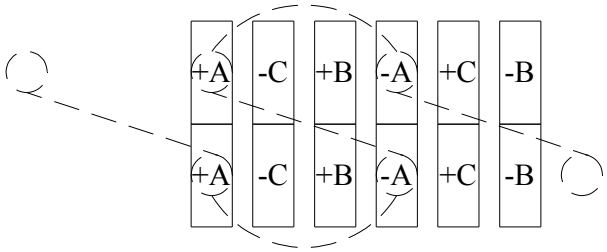

Fig. 3.2. Basic winding arrangement of the designed prototype machine.

Thermal conduction favours small slots as the heat dissipation surface is larger compared with the volume. The tooth width is optimized to keep the flux density of the tooth body at 1.5 T. After this point, the current linkage required for the magnetization increases rapidly. Some points of the AC magnetization curve according to the data for the M270-50A sheet by Surahammars Bruks are presented in Fig 3.3.

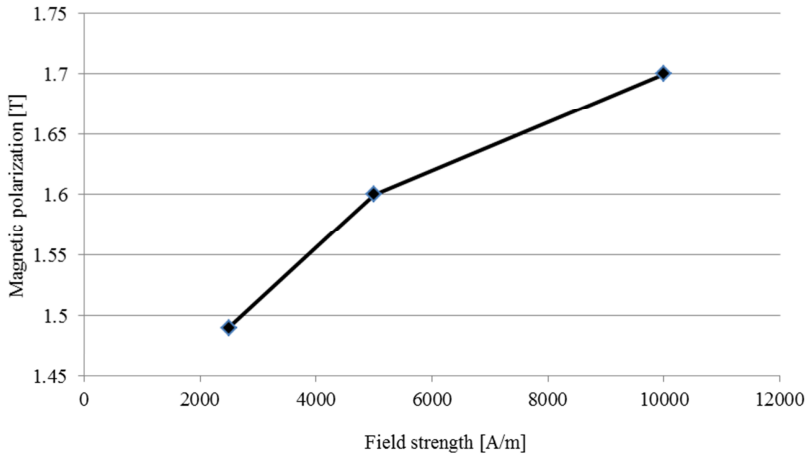

Fig. 3.3. Magnetic polarization with a 50 Hz supply as a function of field strength for the M270-50 A sheet (Surahammars Bruks).

The largest polarization at the 50 Hz excitation given by the manufacturer for the selected M270-50A sheet is around 1.7 T, which can be considered a practical flux density limit for the given sheet grade. The 0.2 T space for the flux density limit is selected to allow space for flux boost to promote reluctance torque production.

Lower flux density values can be used, but this causes additional weight and less slot volume. The priority in the slot height optimization is to allow enough current linkage in the slot to produce rated torque and to maintain as small stator diameter as possible because the space limitation is quite strict. The optimal slot height depends on the thermal balance. The height of the slot is limited by the increasing thermal resistance in the radial direction. The main heat flux from the slot is to the tooth. The slot bottom becomes second. It can be characterized that every slot has one tooth in parallel. Thus, the average heat conduction length in the tangential and radial directions is half of the slot width and slot height, respectively. The assumed parallel heat paths in the slot region are shown in Fig. 3.4.

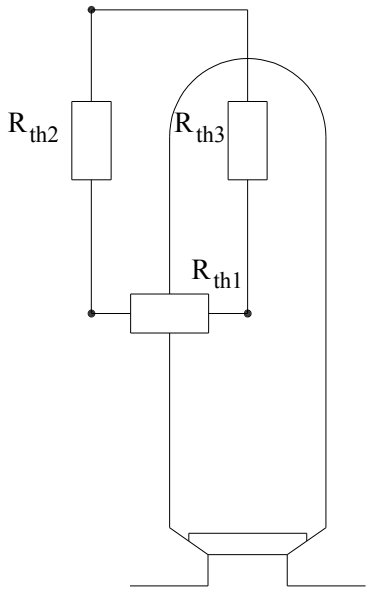

Fig. 3.4. Parallel heat path consisting of one tooth and one slot. Presented heat resistances are used in slot equivalent thermal resistance calculation in Eq. 3.1.

The optimum is found at dimensions for which the parallel connection results in the smallest thermal resistance. The tooth width is set to constant 11.6 mm because of the 1.5 T saturation limit. The slot and tooth are considered rectangular elements. Equation 2.36 is applied to the thermal resistance calculations. The equivalent thermal resistance is calculated as

$$R_{\mathrm{th,eq}} = \frac{(R_{\mathrm{th1}} + R_{\mathrm{th2}})R_{\mathrm{th3}}}{R_{\mathrm{th1}} + R_{\mathrm{th2}} + R_{\mathrm{th3}}} \qquad 3.1$$

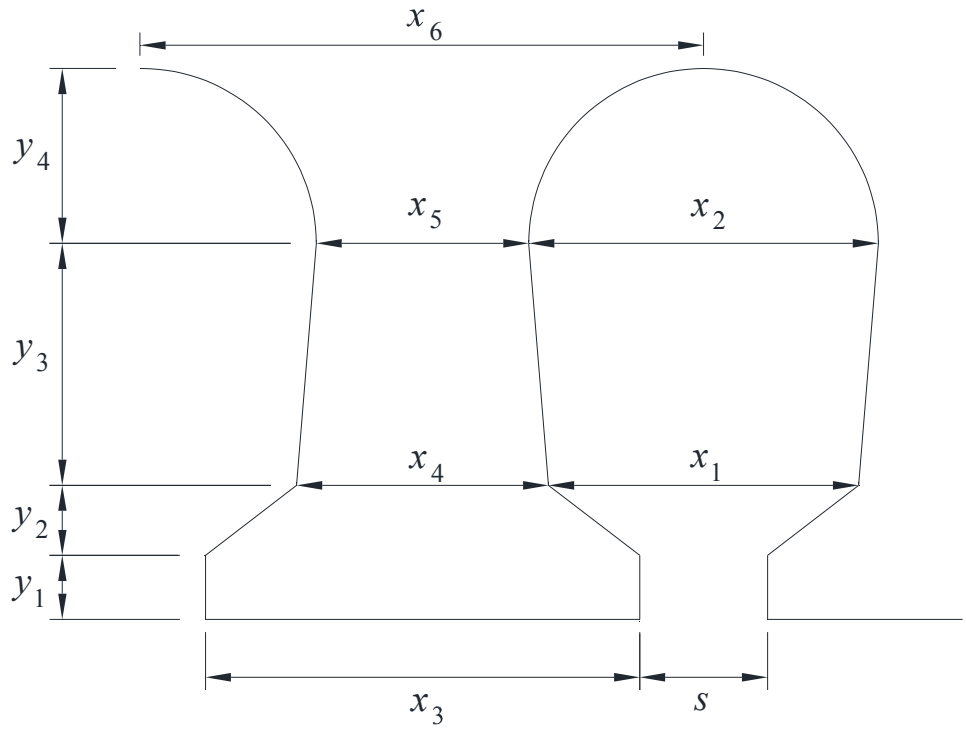

Fig. 3.5. Slot and tooth dimensions.

As a simplification, the slot is modelled as a rectangular element. Dimensions for the rectangular equivalent slot, according to the dimensions in Fig 3.5, are calculated according to

$$h_{\mathrm{eq}} = \frac{y_4 + 2(y_1 + y_2 + y_3)}{2} \tag{3.2}$$

for the equivalent slot height and as

$$w_{\mathrm{eq}} = \frac{x_1 + x_2}{2} \tag{3.3}$$

for the equivalent slot width. The developed simple model has shown relatively good results in the slot area estimation. For evaluation, the thermal conductivities are selected to be 30 W/Km for the core, 0.2 W/Km for the slot impregnation and the slot insulation, 385 W/Km for the copper and 0.026 W/Km for air in the contact region. The selected values are typical for materials used in the thermal modelling of an electrical machine (Miller, 1994). The resistances R_{th1} and R_{th3} also include the air contact resistance (0.1 mm) and 0.24 mm of the slot insulation paper. By varying the tooth slot height from 10 mm to 100 mm, the thermal resistance of the parallel connection varies as presented in Fig 3.6.

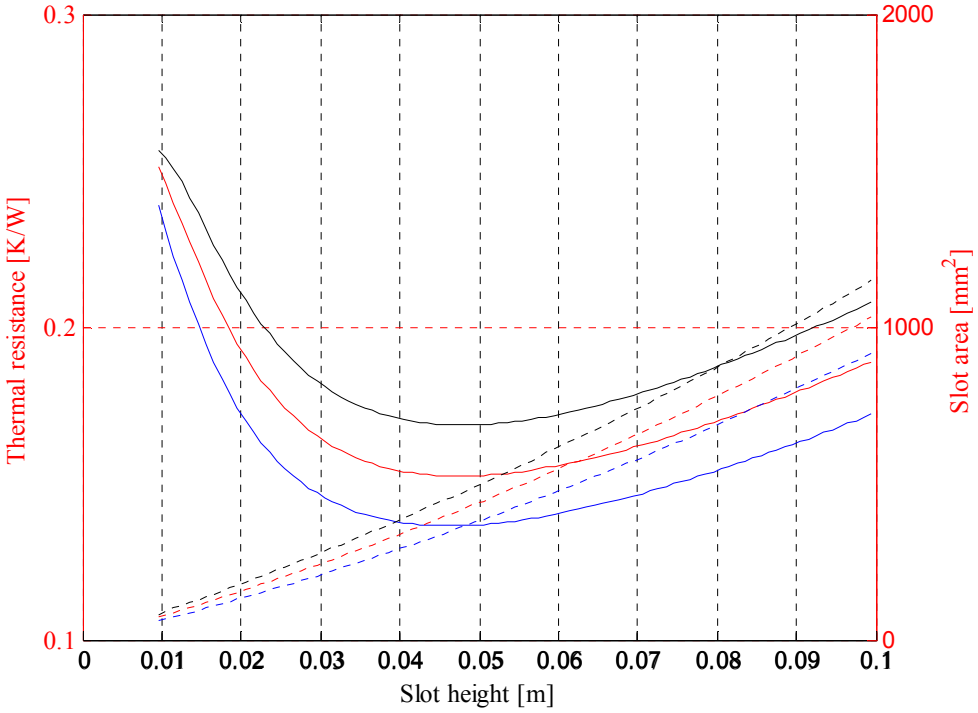

Fig. 3.6. Thermal resistance as a function of slot height for the parallel connection of Fig 3.4 is presented with solid lines. The black line is for a nominal 11.6 mm tooth width. The red and blue lines are for 1.1 and 1.2 times the nominal tooth width, respectively. The dotted lines present the slot cross-sectional area development as a function of slot height.

The local minimum for the thermal resistance of the parallel connection is found at 47.52 mm at the 11.6 mm tooth width. As the tooth gets wider, the optimal tooth height gets lower values because the thermal conduction path has to be shortened as the heat exchange surface of the slot bottom decreases. Nevertheless, a longer tooth can be used as far as the combined thermal resistance is lower than that of the narrower teeth. The slot leakage should also be taken into account to avoid excess leakage. The slot leakage behaviour according to slot dimensions equivalent to Fig. 3.6 is presented in Fig. 3.7.

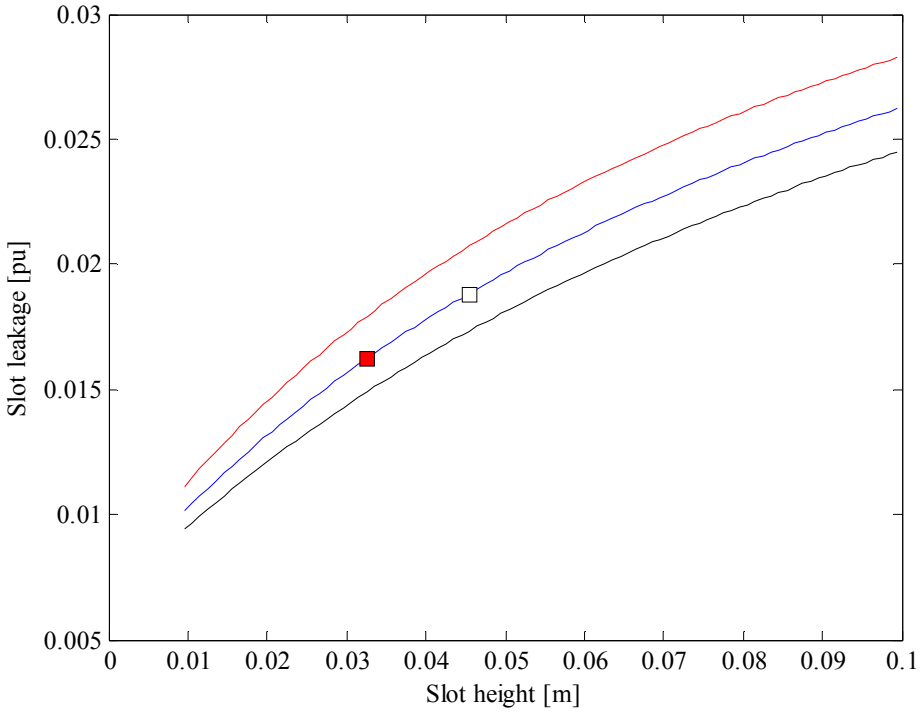

Fig. 3.7. Slot leakage as a function of slot height for a double-layer winding. Per unit values are calculated for the nominal operating speed of 1000 min^{-1}, a 150 V line-to-line voltage and a 100 A line current, which yields an inductance base value L_b of 0.001 H. The red square indicates the leakage value for the selected slot height. The white rectangle represents the optimal slot height according to (Eq. 3.1) at the 11.6 mm tooth width.

Owing to the diameter limit of 380 mm and the flux density limit of 1.5 T, the slot height has to be set as 32.5 mm, which is considerably less than the model suggests. The situation could be corrected by decreasing the rotor diameter, but this would endanger the torque output capability of the machine.

The other issue related to the heat path optimization is the slot size. It has to be ensured that the slot is large enough to carry the current required for the nominal torque. Winding turn number was estimated with equations presented in Section 2.1.2. The total one-phase winding turn number is 64, which yields z_Q=8 coil sides in one slot to match the back EMF to the specified supply voltage of 300 V at a 2000 min^{-1} rotating speed. The selected slot dimensions result in a slot area of 286 mm^2, which still produces a

$$J = \frac{z_Q I_s}{0.5 S_{slot}} = \frac{8 \cdot 100}{0.5 \cdot 286} = 5.6 \text{ A/mm}^2$$

current density value for the 50 % space factor at the rated current of 100 A. The current density is within the limits for water-cooled synchronous machines as presented in Table 2.3. Thus, the cooling of the machine should not give any cause for concern.

The current-carrying capacity can be referred to the slot size as it is directly proportional to the electrical resistance and thereby directly proportional to the heat dissipation of the slot. The slot area and the slot heat dissipation capability are presented in Fig. 3.8. The heat dissipation of the slot is corrected by multiplying the slot copper area by a 5.6 A/mm^2 current density and by assuming a 50 % filling factor for the slot copper. The slot size and the thermal voltage along the equivalent thermal resistance are presented in Fig. 3.7.

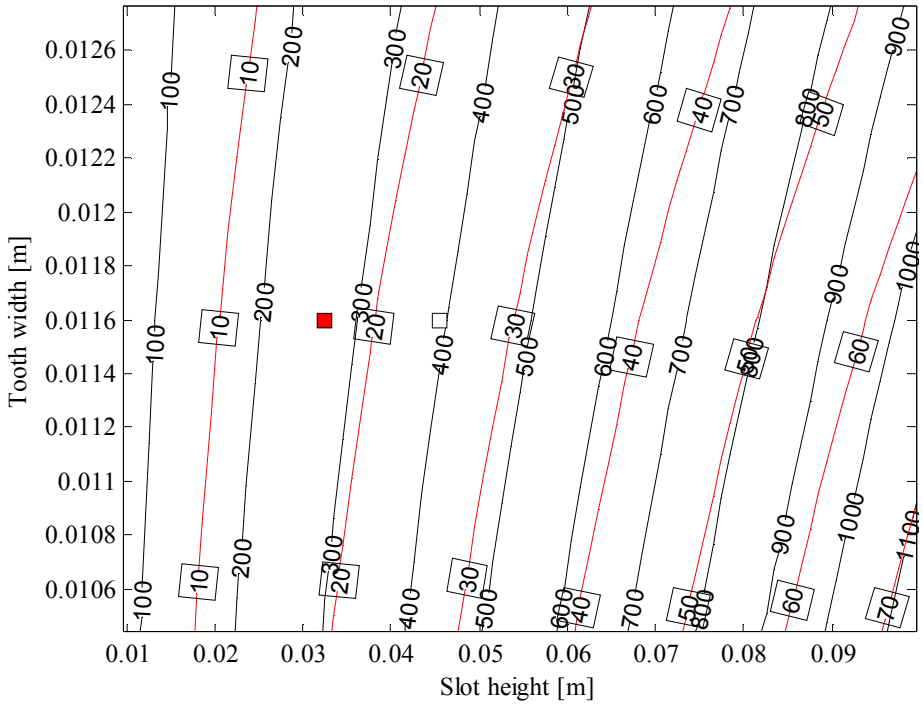

Fig. 3.8. Slot area and indicative temperature difference in the equivalent thermal resistance. The black contour lines represent the slot cross- sectional area. The red lines indicate temperature over equivalent resistance. The red rectangle shows the value for the selected slot height. The white rectangle represents the optimal slot height according to (Eq. 3.1) at the 11.6 mm tooth width.

Figure 3.8 shows that with the optimal slot height for the machine geometry, the slot copper heats more with the same current density value. In order to achieve the same heat flux density with a smaller slot, the current density of the optimal slot geometry would have to be reduced to the value of ~4 A/mm^2.

The magnet module (MM) topology was selected to minimize the consumption of magnet material even though an embedded magnet (EM) arrangement would be mechanically more stable. The fixing of the magnets in the MM design is essential for the machine endurance.

The further development of the machine structure was performed with finite element methods by inspecting different machine geometries for enhanced torque production within the limits of the existing dimensions and power supply.

It was discovered that a magnetic pole construction with sheet metal side bars would be beneficial from the perspective of the torque output as discussed in Section 1.3.2. The only concern was the fixing of the magnet unit on the rotor surface. Thus, from the very beginning, the machine design was a challenging task, because adhesive fixing has generally been avoided in these machine designs, even though the manufacturer specifications for the adhesive holding capability would seem convincing. The resulting pole configuration of the electrical machine is presented in Fig. 3.9.

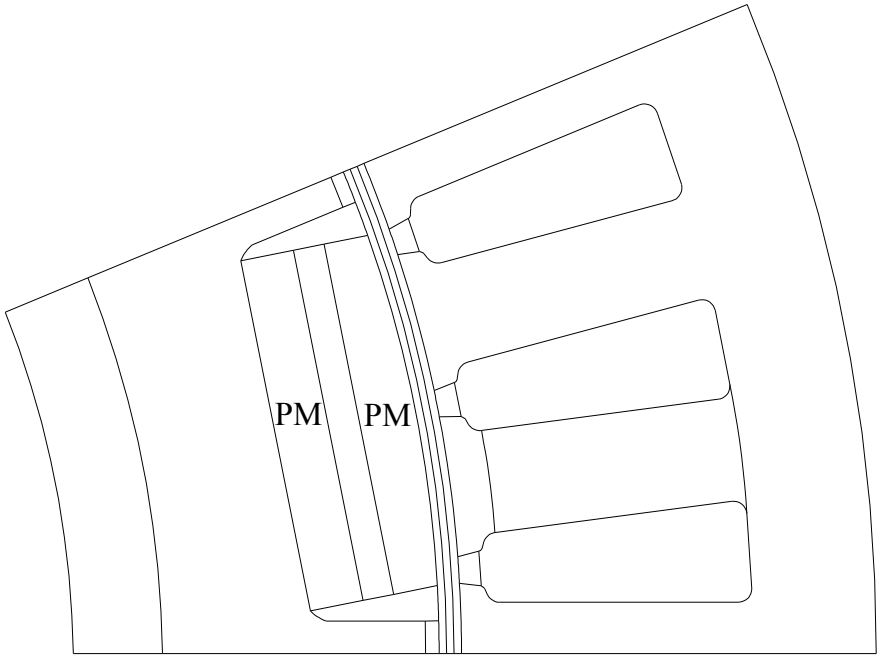

Fig. 3.9. MM machine pole geometry with a glued magnet pole structure.

The pole structure produces similar behaviour of the direct- and quadrature-axis magnetic conductivity as in the embedded magnet design. The difference is that the iron cams are separated from the magnets to prevent short-circuiting of the magnets. This ensures better utilization of the magnet material in the flux production as the leakage flux caused by the iron passage short-

circuiting is prevented. The magnet itself consists of three parts as presented in Fig 3.10. The top and bottom layers of the magnets are separated with a high-permeability SOMALOY™ soft magnetic composite layer. The purpose of the SMC layer is to guide the flux in the q-axis direction for high reluctance torque operation. The soft magnetic composite piece between the magnets is also easier from the manufacturing point of view, and compared with the solid block solution, the core losses are much lower. However, the mechanical structure is weaker compared with embedded designs, but the lower magnet volume and the option to use a magnet material with a low remanence value can make difference in an application that does not require high operating speeds. The direct-axis inductance of the surface magnet machine is also slightly smaller compared with the embedded magnet design, which usually results in higher pull-out torque characteristics.

The results of the finite element calculations were promising, but because of the current limitation, the machine pull-out torque maximum was lowered to the value of 700 Nm. The mechanical strength of the machine gave some cause for concern, but eventually, the construction of the prototype machine was accomplished.

3.1.1 Testing and mechanical aspects

In the final structure, the topmost layer of the magnet was slit towards the air gap in the axial direction to reduce the eddy current effects. The magnet stack was bundled up with a two-compound composite adhesive, and the whole stack was tied to the rotor surface with a two-component Araldite™ epoxy resin. The magnet module is shown in Fig. 3.10.

Fig. 3.10. Three-layer magnet module of the MM machine. The top and bottom layers are made of a Ne493a grade magnet material. The material of the middle layer is a Somaloy 550 composite. The whole assembly is epoxy coated. The slitting of the topmost magnet is not shown because of the epoxy coating.

The fixing of the magnets was a challenging task. First, the machine was tested with the adhesive fixing of the magnets. This resulted in a failure in the magnet fixing during the initial testing. Apparently, the sizing could not resist the forces acting inside the machine, even though the

calculated safety factor according to the tensile strength was high. The machine could be stopped fast enough to prevent any severe damage.

A carbon fibre banding was also tested, but the fibring process failed in the curing mold installation, and the band was damaged. This resulted in a band failure at the 1500 rpm speed and led to a total destruction of the test rotor and the windings. The rotor was next secured with a fibreglass band and an elastic polybutadiene resin. This arrangement showed good endurance, but the band failed in the final tests at 2000 rpm; however, the machine did not suffer any additional damage.

Although the test results were adequate and feasible, at least to some degree, an additional series of tests were performed with a welded stainless steel band. It was known beforehand that stainless steel has a high coefficient of temperature enlargement, and a possible failure was therefore expected. However, the stainless band performed extremely well up to the 1500 rpm operating speed, and no weakening was noticed even in the maximum torque tests. The 2000 rpm operating speed was again too much. The band yielded and the tension caused the band to touch the stator surface as a result of the excess heating of the band. The operation was normalized again when the rotating speed was lowered to 1500 min^{-1}. The finite element method verifies the excess heating of the band caused by the conducting losses. Calculations at the rated current show eddy current loss generation of 316 W already at the 1000 min^{-1} rotating speed. The eddy current losses increase to the level of 1300 W at the 2000 min^{-1} rotating speed. The band causes about a 1.2 % unit decrease in the efficiency ratings at the rated 25 kW power. Thus, it is not advisable to use conducting banding at these frequency levels.

This magnet module machine type still needs further development to overcome the mechanical problems, but thus far, the results are promising. However, it was decided to design a new rotor structure instead to ensure safe machine operation. The new rotor structure was designed with buried magnets to the same frame geometry as the previous one.

3.1.2 Second generation

To ensure safe operation over 1500 min^{-1} operation, an embedded magnet structure was introduced. To achieve similar operation characteristics, the back electromotive force waveform was equalized. The embedded magnet topology is presented in Fig. 3.11.

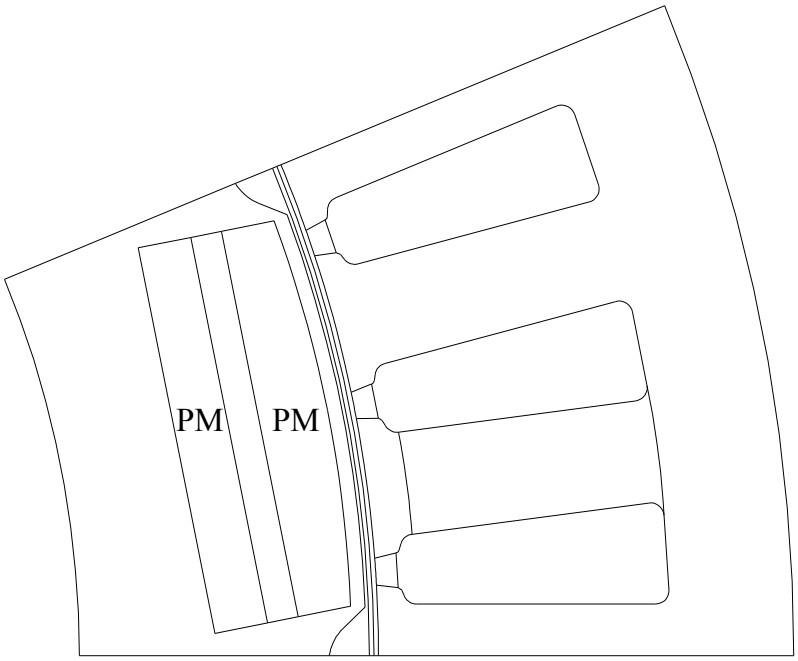

Fig. 3.11. Pole arrangement of the embedded magnet machine.

The two-magnet arrangement has been maintained for the sake of improved inductance ratio, and additionally, the pole is shaped in the q-axis to achieve a similar back EMF waveform as that of the surface magnet structure. The magnet remanence has to be high because of the high stray fluxes in the magnet sides. These two structures are compared in the following sections.

3.2 Steady-state analysis

This chapter presents the results of the steady-state finite element analysis on the designed machine types. The results of the analytical approach in the previous chapters are used as the basis of the finite element modelling. The analytical approach and the finite-element-based methods should go hand in hand in the design process. The finite-element-based computer programs allow a more thorough analysis of the geometry-related effects on the machine performance compared with the analytical methods; however, a careful study of the initial parameters helps in avoiding unnecessary computations.

3.2.1 Back electromotive force

Both of the machines are designed to produce similar back electromotive force characteristics in order to achieve a similar magnetic behaviour. The magnet material for the MM structure is Neorem Ne 493a. The magnet grade data are presented in Fig. 3.12.

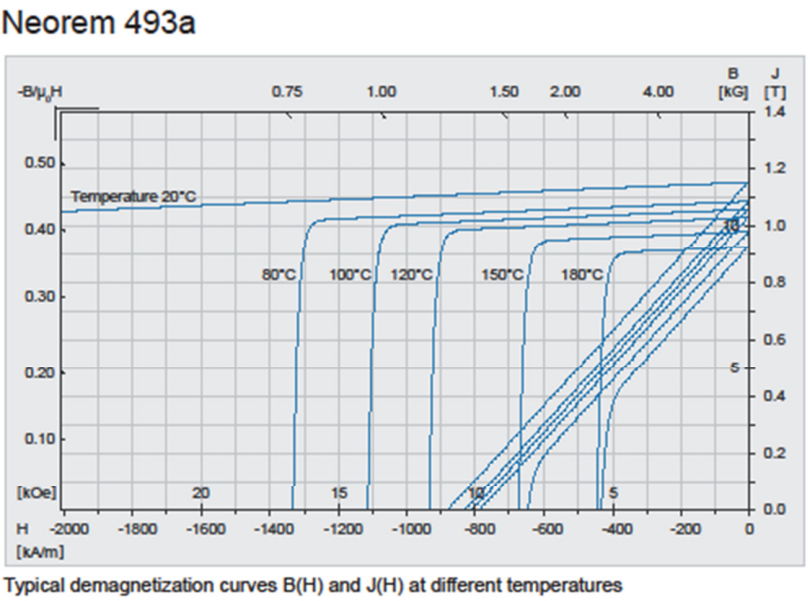

Fig. 3.12. Ne493a grade data by Neorem Magnets.

The embedded magnet structure requires a magnet grade with a larger remanence, because the q-axis provides a short circuit path for the magnet flux. The magnet grade of the embedded magnet machine is Ne753 a of Neorem magnets. The magnet grade data are presented in Fig. 3.13.

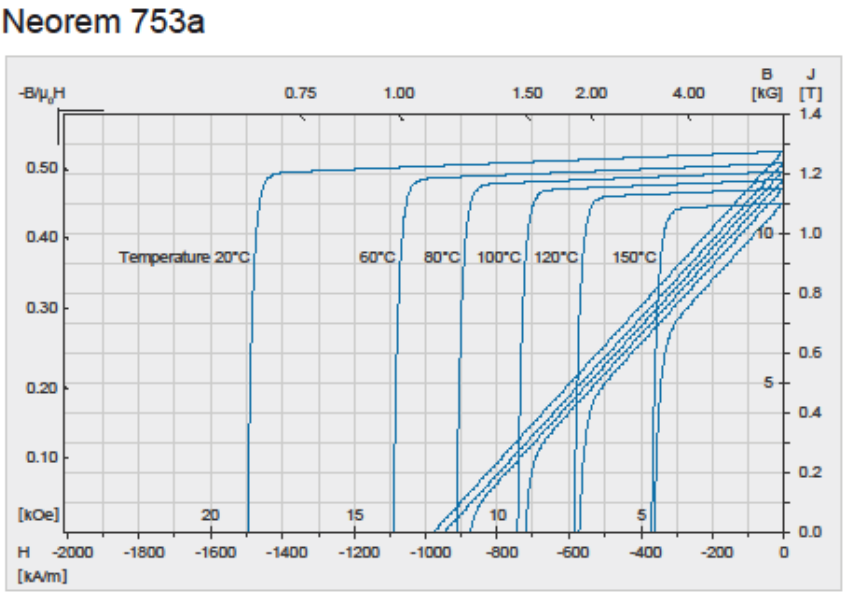

Fig. 3.13. Ne753a grade data by Neorem Magnets.

For finite element calculations, the magnet characteristics are considered for the 100 °C temperature. This yields a 1.07 T remanence for the MM machine and a 1.2 T remanent flux density for the EM machine. When comparing the magnet grade data, the difference in the temperature tolerance becomes evident. The demagnetization curve at the 100 °C temperature of the Ne753 grade has a knee below the 0.3 T flux density. At this temperature, the rotating speed limit would be about 3.9 p.u. This can be estimated by comparing the magnet remanence knee point value with the zero field strength value at a given temperature. Compared with the Ne 493a grade, there is a considerably higher risk of permanent demagnetization in overspeed operation or in short-circuit situations, if the temperature is high enough. The rotating speed limit estimates in per unit values according to the magnet grade data are given in Table 3.1.

Table. 3.1. Estimated rotating speed limits for different temperatures according to the magnet data presented in Figs. 3.12 and 3.13 for the magnets Ne493a and 753a, respectively.

Temperature [°C]	Ne753a	Ne493a
80	12	(no limit)
100	3.9	(no limit)
120	2.3	(no limit)
150	1.52	4.85
180	(no data)	2.09

In order to keep the machine size small, the permanent magnet material should be utilized as well as possible. This requirement results in a squared air gap flux waveform. This can be observed from the back electromotive force calculation in Flux 2D. The results are shown in Fig. 3.14.

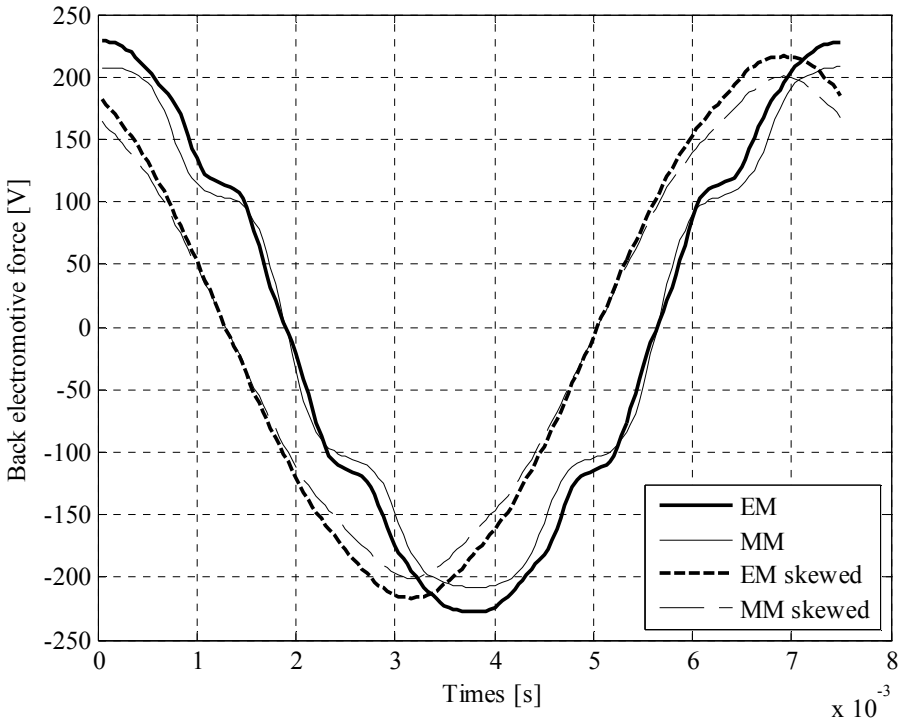

Fig. 3.14. Simulated line-to-line back electromotive waveforms of the prototype machines. The dashed line indicates the EM designs while the solid line is for the MM structure. The one slot pitch skewing of the actual machine results in a more sinusoidal waveform.

The non-skewed back EMF waveform is not sinusoidal, because the pole shapes are not formed to produce a sinusoidal waveform. Nevertheless, the skewing of the actual machine corrects this situation. The pole shapes of the machines are designed to maximize the flux generation with the given magnet material. The pole-generated air gap flux waveforms are presented in Fig. 3.15.

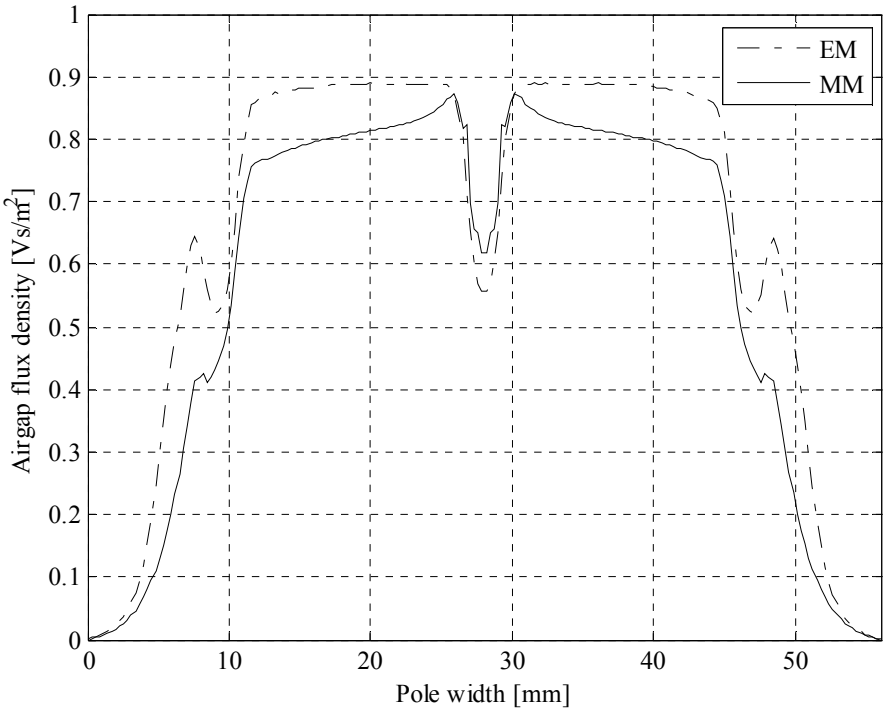

Fig. 3.15. One-pole air gap flux density waveforms normal to the surface for the MM and EM structures in no-load conditions without skewing. The estimate is from the middle of the annulus with a pole position similar to Figs. 3.9 and 3.11. The notching of the waveform is caused by the slotting effect.

Because of the stronger magnets, the flux waveform of the EM structure has higher flux density values. The flux maximization results in a square waveform of the air gap flux density. The waveform can be made sinusoidal by pole shaping, but this results in a poor utilization of the magnet material.

3.2.2 Synchronous inductances

The static finite element model illustrates the torque output capability of the machine. There are two ways to analyse the machine performance. A direct method is to obtain steady-state performance points by a Flux 2D simulation. Even though the current-fed calculations are relatively fast, the calculations still take time. Another method is to use a Flux 2D solution for the two-axis model synchronous inductances as a basis for an analytical performance analysis.

As presented in Section 1.3, the two-axis model synchronous inductances can be used to determine the machine performance characteristics. The magnitude of the synchronous inductance depends

on the magnetization state of the machine. Generally, the direct-axis inductance is quite stable, but the quadrature-axis inductance is sensitive to the magnetization state of the machine.

Traditional two-axis model synchronous inductances can be evaluated by the flux 2D software. The inductances are calculated by applying magnetization to an individual flux axis. The d-axis is placed to point to the coil centre in order to determine the d-axis synchronous inductance. The q-axis is evaluated in a similar way by rotating the pole by 90 electrical degrees to obtain the q-axis in the magnetizing direction.

The steady-state solution of the Flux 2D solver does not take into account the end-winding leakage term. Thus, the leakage in the end-winding region is determined analytically. Later on, the end-winding leakage term is also applied to the transient calculations of the voltage-supplied models. The end-winding leakage term is calculated by equation

$$L_\sigma = \frac{4m}{Q} q N^2 \mu_0 (2 l_{\mathrm{ew}} \lambda_{\mathrm{ew}} + W_{\mathrm{w}} \lambda_{\mathrm{w}}) \qquad 3.4$$

where

- l_{ew} is the axial height of the end winding,
- W_{w} is the width of the coil span and
- λ_{ew} and λ_{w} are the permeance coefficients of the end winding according to to (Vogt, 1983).

The terms λ_{ew} and λ_{w} are permeance coefficients of the winding geometry. The cross-section of the end-winding region of the winding scheme presented in Fig. 3.8 is in accordance with Fig. 3.16. Thus, the corresponding coefficients λ_{ew} and λ_{w} have values 0.324 and 0.243 (Vogt ,1983), respectively.

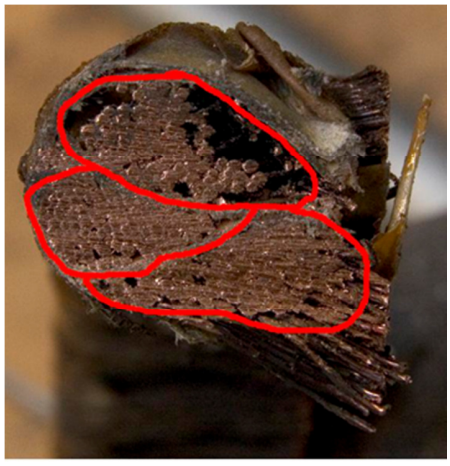

Fig. 3.16. Geometrical arrangement for the end winding of a half slot winding results in the values of 0.324 and 0.243 for λ_{l} and λ_{w}, respectively (Vogt, 1983) for the end-winding leakage term calculation.

According to the winding dimensions, the leakage term according to Eq. (1.3) is 0.0537 mH, which yields 0.052 in per unit values. The inductance base value for the per unit conversion is calculated for a 1000 min^{-1} rotating speed, a 150 V line-to-line voltage and a 100 A line current, yielding 1.03 mH. The synchronous inductances of both machine structures, including the end leakage term, are presented in Fig. 3.17.

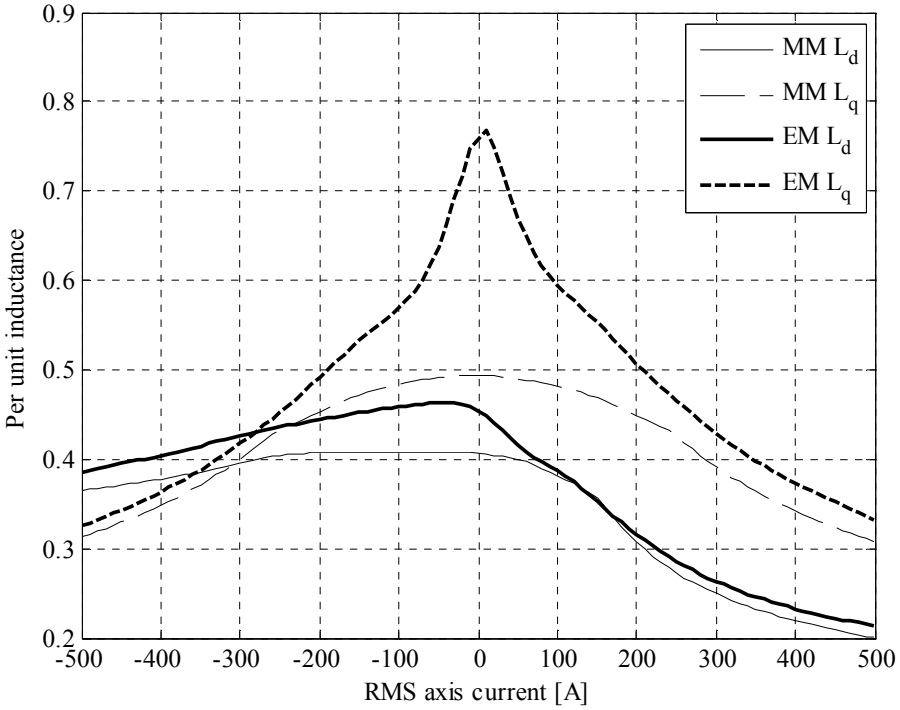

Fig. 3.17. Direct- and quadrature-axis inductances as a per unit value presentation as a function of supply current. The current is aligned with one axis at a time to obtain the inductance values for the given axis. The method is applied separately for the d- and q-axes.

Fig 3.17 shows that the EM machine has higher inductance ratings than the MM machine, which is in good agreement with the theory of inductance calculation, because the EM configuration has more iron in the flux path compared with the MM configuration. The direct-axis inductance is 0.46 for the EM structure and 0.41 for the MM structure. Because the direct-axis synchronous inductance is inversely proportional to the breakover torque, the breakover torque values for the MM and EM machine according to Table 3.2 inductances would be 2.44 and 2.17 times the nominal torque of 240 Nm if the saliency and saturation effects are neglected.

The quadrature-axis inductances are higher compared with the direct-axis inductances, as expected. The quadrature-axis inductances seem to saturate heavily as the q-axis current increases, especially in the EM structure. Because of the armature reaction, the flux path starts to shift in the q-axis direction, which causes the q-axis inductance to saturate.

Since the two-axis model values are calculated separately for the d- and q-axes, the estimate does not take into account the cross-saturation effect on the inductances. In this type of traction machines, an individual axis analysis in not sufficient for accurate performance evaluation as presented in the following sections. The direct- and quadrature-axis inductances depend on both current components. The cross-magnetizing effect can be evaluated by calculating the inductances of individual axes in interference with the intersecting current component as presented in (Stumberger et al., 2003). Inductances are calculated according to the equation

$$L_{\mathrm{d,q}} = \frac{\partial \psi_{\mathrm{d,q}}\left(i_{\mathrm{d,q}}, i_{\mathrm{q,d}}\right)}{\partial i_{\mathrm{d,q}}} \approx \frac{\Delta \psi_{\mathrm{d,q}}}{\Delta i_{\mathrm{d,q}}} \tag{3.5}$$

The direct- and quadrature-axis inductance graphs for the MM and EM arrangements are presented in Figs. 3.18–3.21.

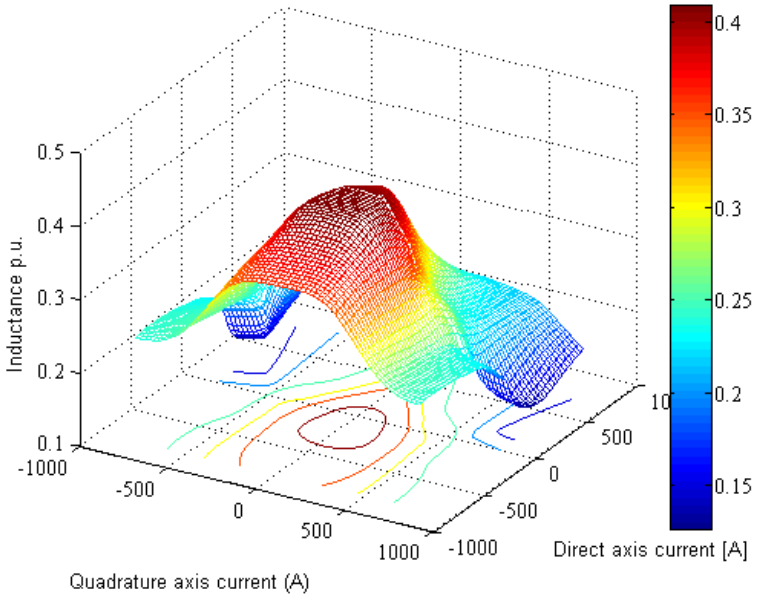

Fig. 3.18. Per unit direct-axis synchronous inductance including the cross-saturation effect of the quadrature-axis current on the MM machine.

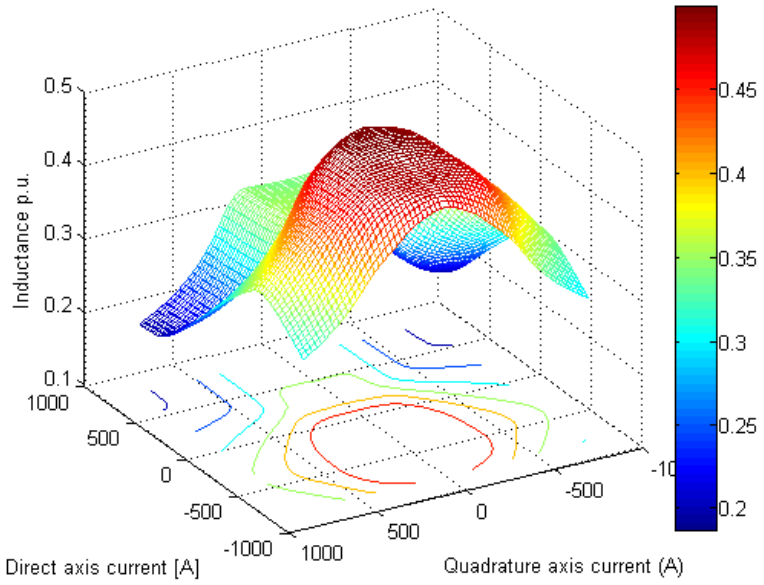

Fig. 3.19. Per unit quadrature-axis inductance including the cross-saturation effect of the direct-axis current on the MM machine.

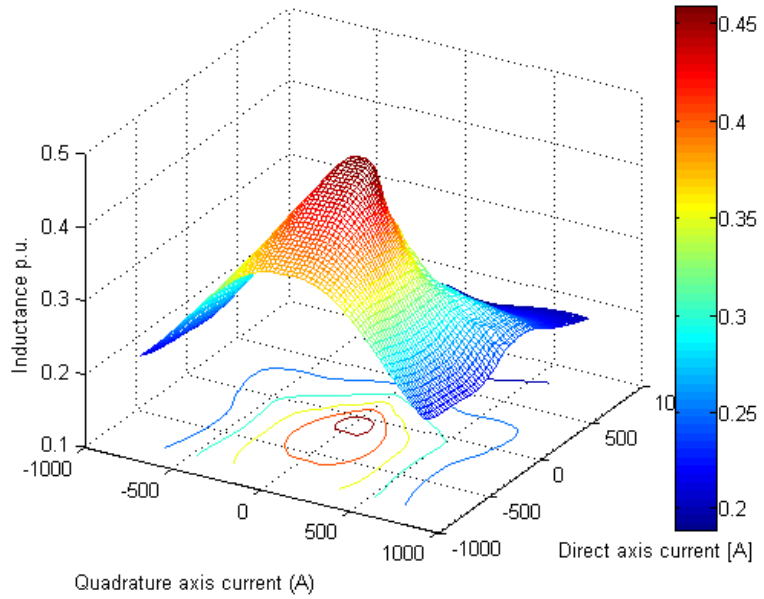

Fig. 3.20. Per unit direct-axis synchronous inductance including the cross-saturation effect of the quadrature-axis current on the EM machine.

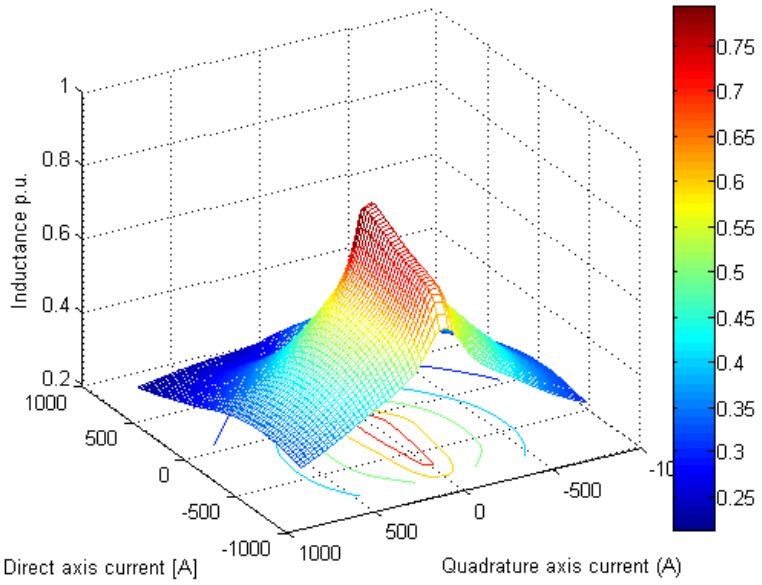

Fig. 3.21. Per unit quadrature-axis inductance including the cross-saturation effect of the direct-axis current on the EM machine.

The inductances are symmetrical with the positive and negative values of the quadrature-axis current in both L_d and L_q. The main difference lies in the direct-axis current component. With the demagnetizing direct-axis current, the inductance levels usually remain steady as presented above in Fig. 3.17. An increasing torque causes the direct-axis inductance to saturate earlier, which narrows down the field weakening region of the machine. Compared with the EM design, the magnet module inductances respond slowly to current changes. The laminate material in the rotor surface of the EM machine and the iron paths to the quadrature axis saturate more easily under increased magnetization, which causes large variations in the inductance values.

3.2.3 Torque production

In the normal motoring operation of the non-salient pole machine, the $i_d = 0$ control usually develops the best torque to current ratio, and the torque is controlled by the amount of positive I_q current. For non-salient pole designs, the best combination is found by using a suitable amount of negative direct-axis current along with the positive quadrature-axis current, as presented in Section 1.3.3.

Traditionally, individual axis inductances have been used for salient pole machine performance estimation. The per unit values of Fig. 3.17 are given in Table 3.2.

Table. 3.2. Per unit inductances of the MM and EM structure. The currents are aligned according to the corresponding axes as presented in Fig. 3.17.

Current [A]	$L_{d,EM}$	$L_{q,EM}$	$L_{d,MM}$	$L_{q,MM}$
-500.0	0.39	0.33	0.36	0.31
-450.0	0.39	0.34	0.37	0.33
-400.0	0.40	0.36	0.38	0.35
-350.0	0.41	0.39	0.39	0.37
-300.0	0.43	0.42	0.40	0.40
-250.0	0.44	0.45	0.40	0.43
-200.0	0.44	0.49	0.41	0.45
-150.0	0.45	0.53	0.41	0.47
-100.0	0.46	0.57	0.41	0.48
-50.0	0.46	0.64	0.41	0.49
-10.0	0.46	0.66	0.41	0.49
10.0	0.46	0.69	0.41	0.49
50.0	0.46	0.72	0.41	0.49
100.0	0.46	0.75	0.41	0.49
150.0	0.45	0.77	0.41	0.49
200.0	0.42	0.67	0.40	0.49
250.0	0.39	0.59	0.38	0.48
300.0	0.35	0.55	0.36	0.47
350.0	0.32	0.51	0.31	0.45
400.0	0.29	0.47	0.27	0.43
450.0	0.26	0.43	0.25	0.39
500.0	0.25	0.40	0.23	0.36

According to the estimated two-axis model inductances, the torque output of the machine can be estimated by Eq. 1.9. The torque production as a function of current angle is presented in Fig. 3.22.

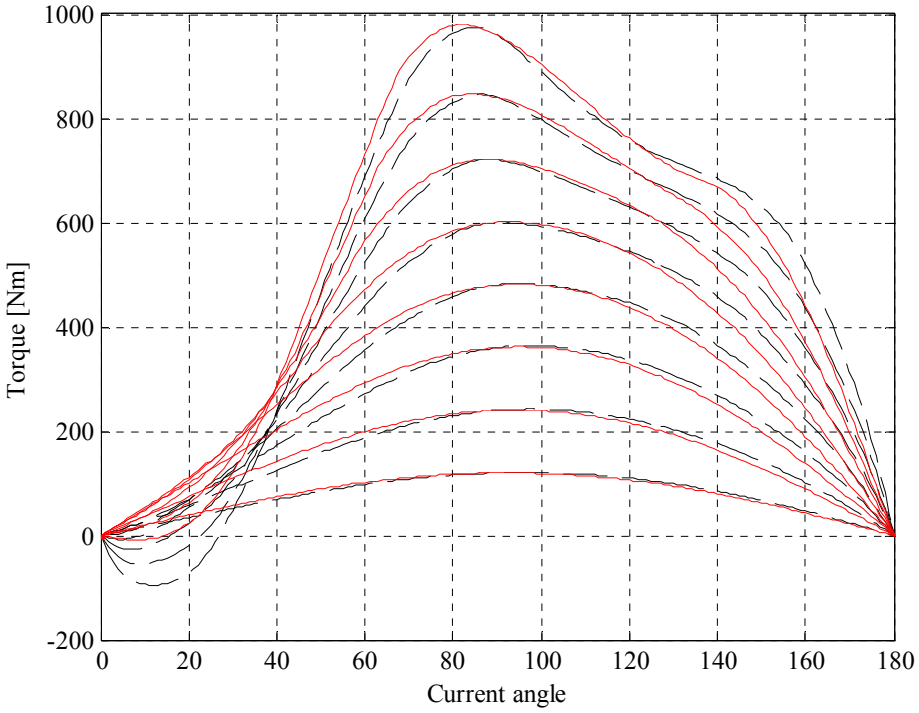

Fig. 3.22. Estimated torque output as a function of current angle calculated according to the synchronous inductance data presented in Fig. 3.17 and Table 3.2. The solid line is for the MM machine while the dashed line is for the EM machine. The currents range from 50 A_{RMS} to 400 A_{RMS} at 50 A_{RMS} steps. Stator Joule losses are neglected. Permanent magnet flux and supply voltage are 1 p.u.

The estimation of individual component torque production according to the inductances of Table 3.2 shows peak torques below current angles of 90 degrees at the current ratings above 200 A, which is caused by the reverse of the inductance ratio as the saturation reduces the quadrature-axis inductance below the direct-axis inductance values, as presented in Fig 3.22. The negative torque at low current angle values is caused by the reluctance torque being larger than the synchronous torque component.

As a comparison with Fig. 3.22, the electromagnetic torque estimation according to the magneto-static model of Flux2D™ at 100 A of excitation is presented in Fig. 3.23.

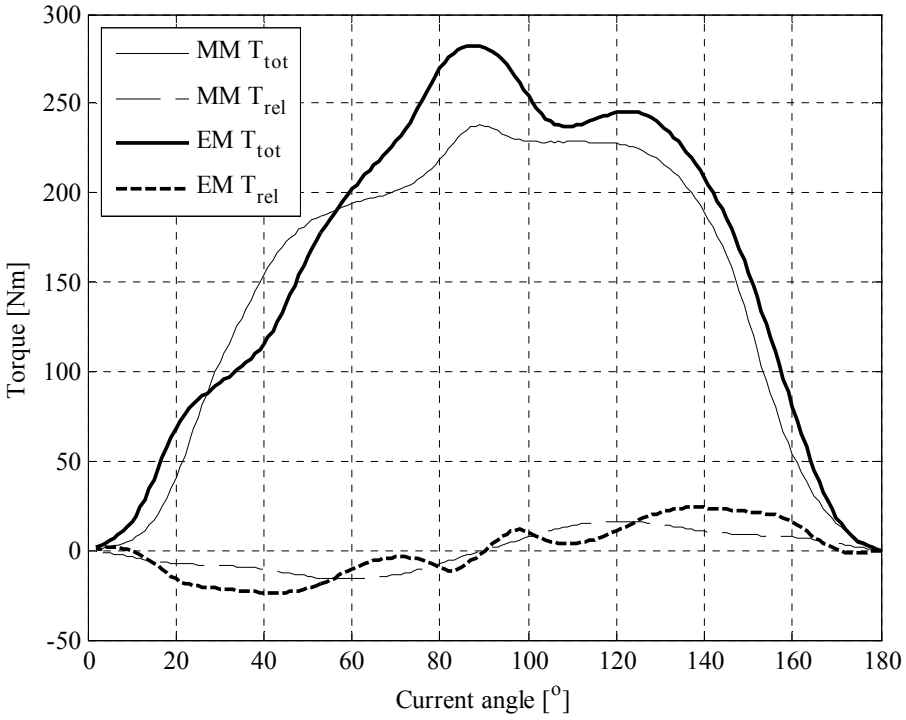

Fig. 3.23. Torque production as a function of current angle according to the Flux 2D model at the 100 A current.

The torque curve is distorted, and the peak torque point is not as distinct as the theory suggests. This is mainly due to the absence of skewing in the modelling. The permeance differences resulting from the rotation of the rotor in the static analysis cause fluctuation in the torque curve, and thus, do not give a reliable estimate on the torque behaviour. Nevertheless, the reluctance peak is higher for the embedded design, and the earlier occurrence of the reluctance torque maximum seems to favour the magnet module design. The finite element evaluation also predicts a torque peak around a 90-degree current angle at the nominal current, which is in line with the analytical evaluation.

At higher current levels, the finite element approach suggests current angles above values of 90 degrees, which is in line with the theory presented in Section 1.3 but differs from the analytical two-axis model results presented in Fig 3.22. At higher current values, the torque curves start to reach a uniform shape for both of the machines. The peak torque production takes place around 120-degree current angle for both machines. The Flux 2D estimates for torque at the 300 A and 400 A currents are presented in Figs. 3.24 and 3.25.

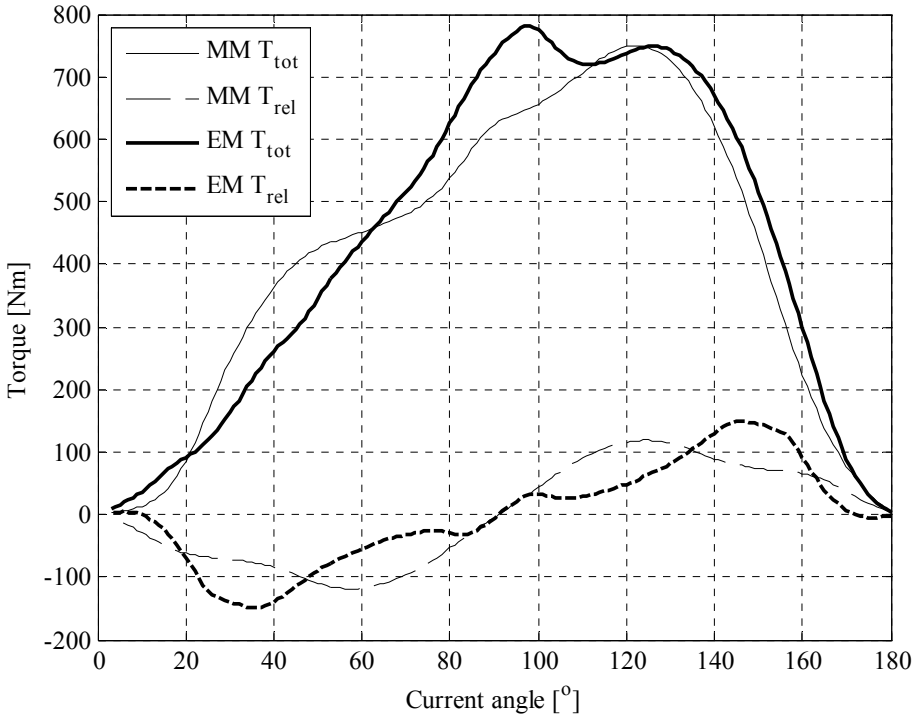

Fig. 3.24. Torque production as a function of current angle according to the Flux 2D model at the 300 A current.

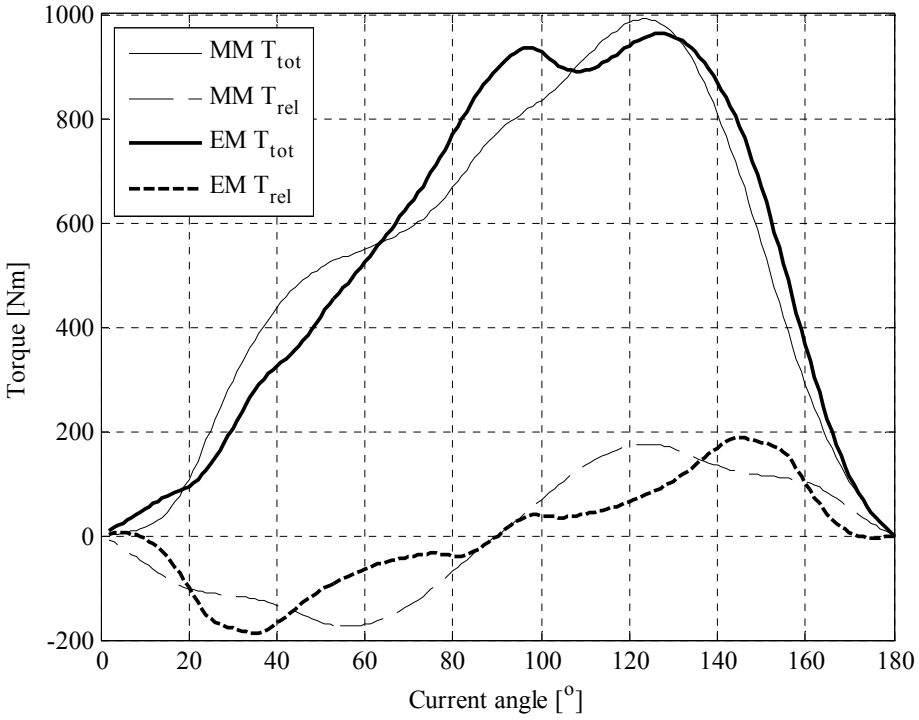

Fig. 3.25. Torque production as a function of current angle according to the Flux 2D model at the 400 A current.

The reluctance torque production can be seen clearly as a flux path shift at the higher supply current values compared for example with the nominal point current value of 100 A. However, the curve of the reluctance component according to the current angle is completely unique for both of the machines. The reluctance torque production requires large currents and demagnetizing current in the direct axis.

The two-axis inductance estimation alone does not give an exact estimate of the machine inductance behaviour, because the air gap flux density waveform is not purely sinusoidal (see Fig. 3.15), (Miller, 1994). The peak values of torque at different excitation currents seem to match closely, but the difference in the occurring current angle is significant. The armature reaction, which consists of the d-axis and the q-axis field should be taken into account in more detail to achieve a better correspondence of the analytical and finite-element-based estimates. With the cross-saturation taken into account, the torque curve of the analytical model is corrected close to the finite element estimates as presented in Fig. 3.26.

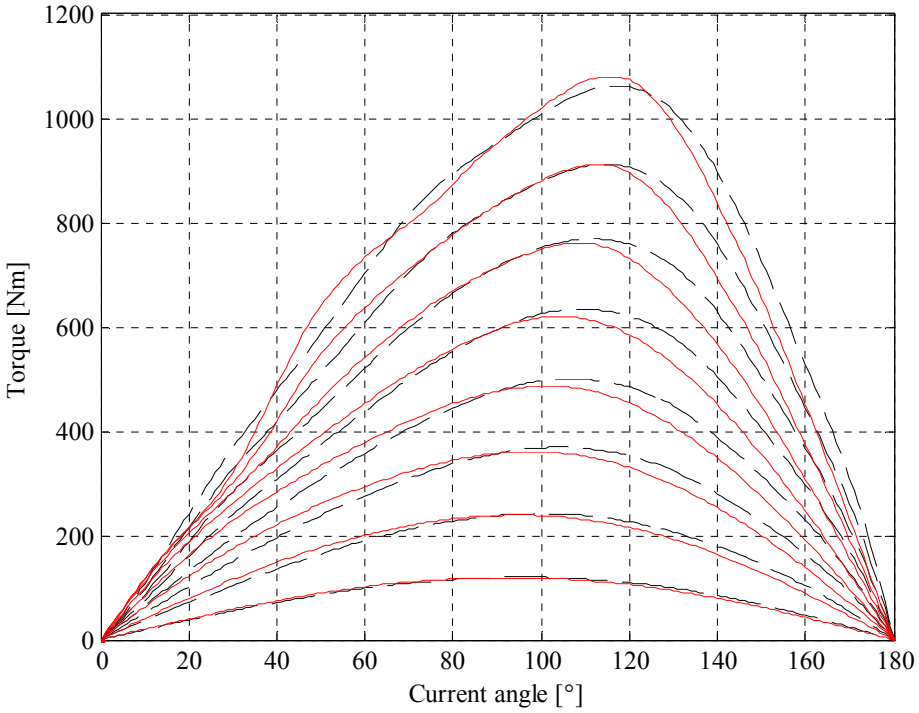

Fig. 3.26. Estimated torque output as a function of current angle calculated according to the cross-saturated inductances. The solid line is for the MM machine, while the dashed line is for the EM machine. The currents range from 50 A_{RMS} to 400 A_{RMS} at 50 A_{RMS} steps. Stator Joule losses are neglected. Permanent magnet flux and supply voltage are 1 p.u.

The torque production curve is now in line with the theory. The steady-state current analysis suggests a similar behaviour of the torque production in the finite element modelling. Even though the inductance charts seem to differ substantially, as shown in Figs. 3.18–3.21, the torque production behaviour is surprisingly similar.

Both of the designs show increased torque production capability because of the rotor saliency. The reluctance torque component curves are presented in Fig 3.27 and the proportion of the reluctance torque production in the total torque production is presented as a function of current angle in Fig. 3.28.

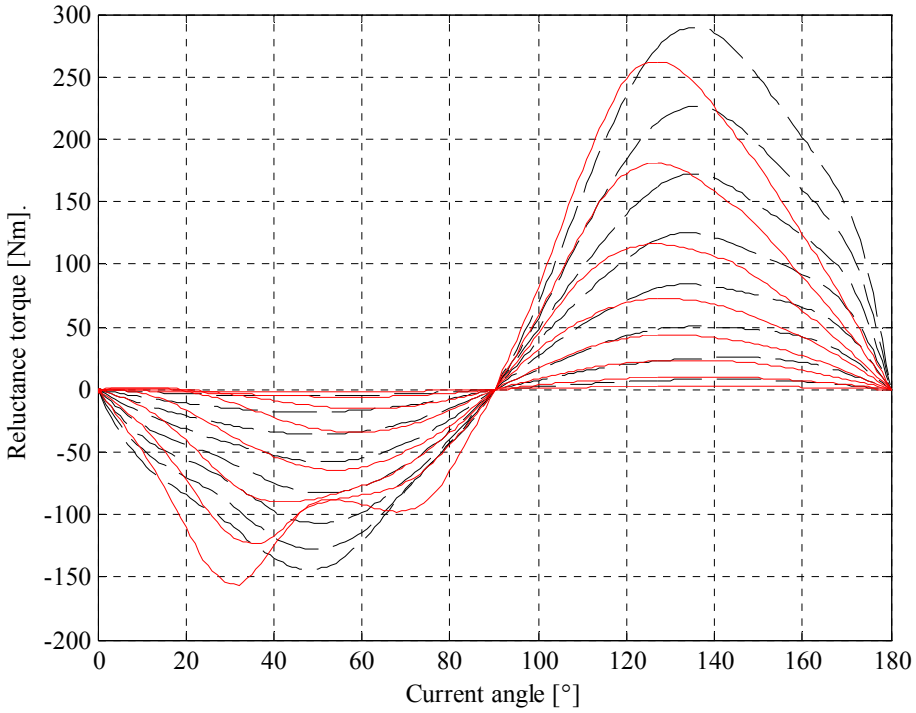

Fig. 3.27. Reluctance torque component as a function of current angle. The currents range from 50 A_{RMS} to 400 A_{RMS} at 50 A_{RMS} steps. The dashed line indicates the EM machine and the solid line for the MM machine.

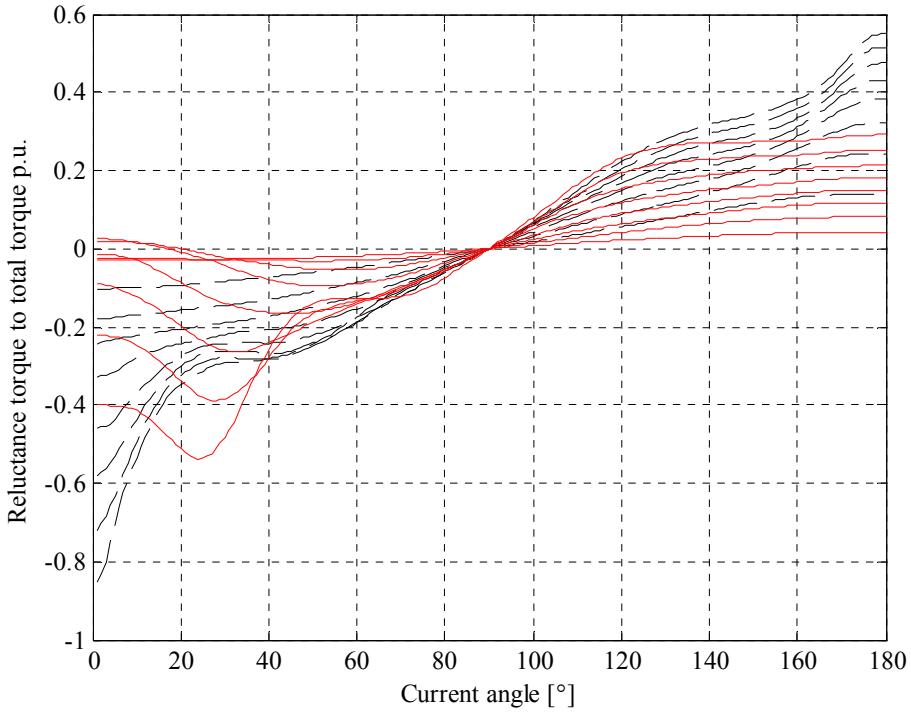

Fig. 3.28. Proportion of reluctance torque in the total torque production as a function of current angle. The currents range from 50 A_{RMS} to 400 A_{RMS} at 50 A_{RMS} steps. The dashed line indicates the EM machine and the solid line for the MM machine.

The torque curves in Fig. 3.27 and 3.28 demonstrate a clear benefit of the reluctance torque production in the total torque output. The reluctance component is around 20 % of the total torque output at high current values. The analytical and finite element results show that the machines under study have potential, and the reluctance torque component can be increased significantly with a suitable amount of current.

The design process shows that special attention has to be paid to the modelling process. The evaluation suggests that the estimation of the cross-saturation effect is essential in the torque production analysis of a traction machine. The results are also important from the perspective of the drive parameter selection. Comparing with Figs. 3.22 and 3.26, the incorrect selection of drive parameters can lead to a ~20 % loss in peak torque production.

To achieve the best performance, the electrical machine should be driven with a minimum current control, which results in the highest torque to current ratio for the given operation point as presented in Fig. 3.29.

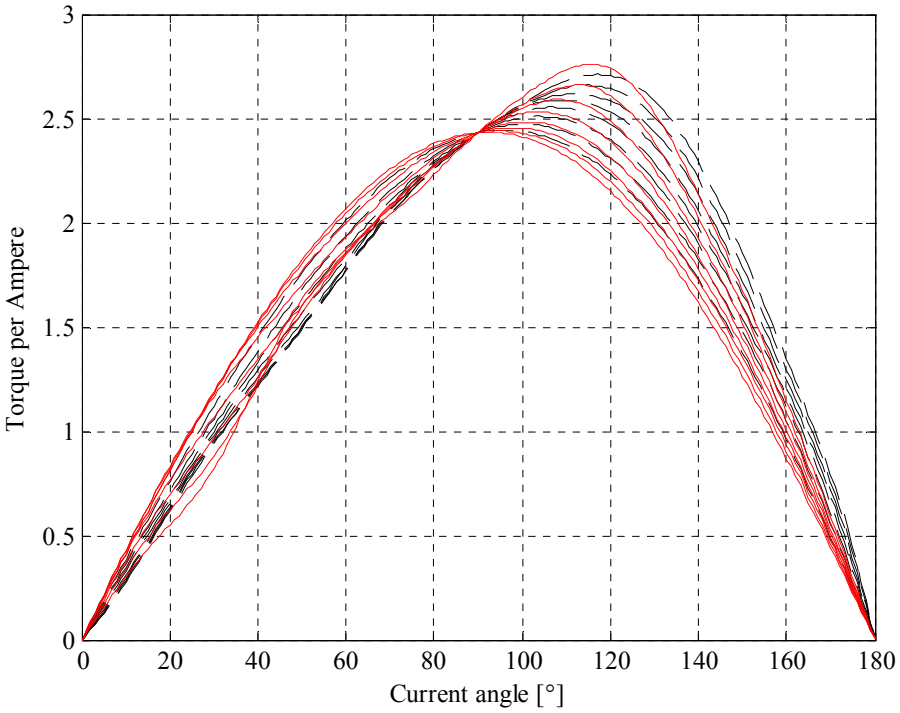

Fig. 3.29. Torque per ampere production as a function of current angle. The currents range from 50 A_{RMS} to 400 A_{RMS} at 50 A_{RMS} steps. The dashed line is for the EM machine while the solid line is for the MM machine.

The highest torque to ampere ratios are achieved at current angles at which the reluctance torque component reaches the highest values.

3.2.4 Performance over speed range

The machine performance over the operating speed range is important in traction drives. Varying supply conditions require good understanding of the machine state at different operating points. The torque production characteristic curves as a function of rotating speed for 1 p.u supply voltage are presented in Fig. 3.30. At speeds below 1 p.u., the constant voltage behaviour is shown for curiosity. Keeping the voltage constant results in strongly limited torque production below the rated speed as the current (0.5–4 p.u.) is needed to increase the stator flux linkage, which must in all conditions match with the voltage supply. Comparison with Fig. 3.33 shows that when 0.25 p.u. voltage is used, the torque peak at 4 p.u. current is found at a lower speed, accordingly. These figures are not intended to suggest any control method for the machines but only illustrate the torque producing capabilities at different speeds and constant voltages.

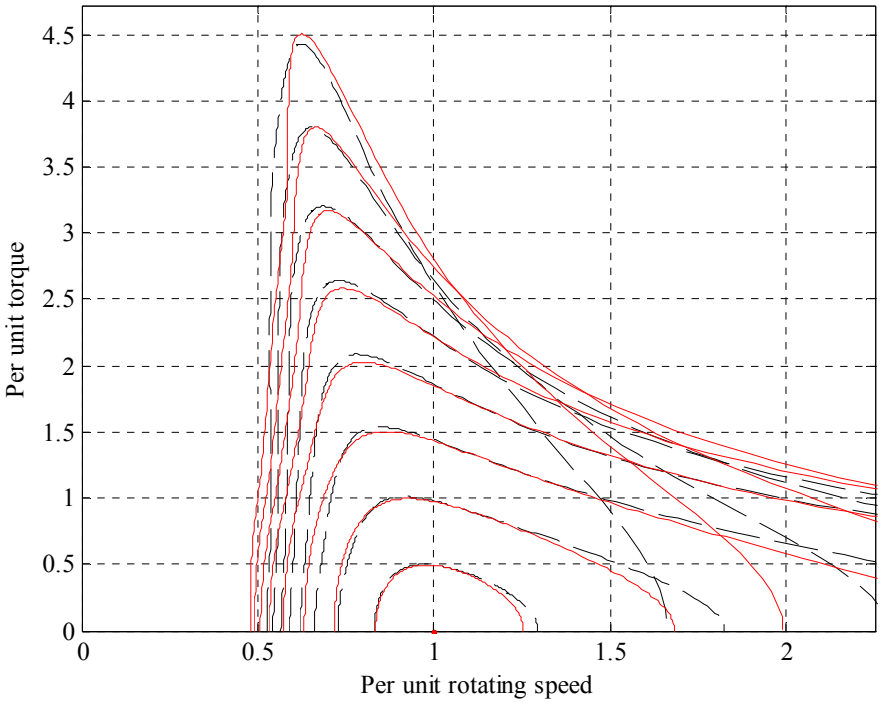

Fig. 3.30. Comparison of torque production at currents 0.5–4 per unit at 0.5 per unit steps. The solid line is for the MM machine and the dashed line for the EM machine. Figure shows the available maximum torque when permanent magnet flux and supply voltage are 1 p.u.

Comparison of the torque curves in Fig. 3.30 shows the better field weakening characteristics of the MM machine. The torque-producing capability of the EM machine is slightly better at higher current values. High pull-out torque values are achieved at subnominal speeds where the excess voltage is used to boost the flux linkage. This point represents the maximum torque output of the machine. Depending on the supply voltage level, the peak torque point shifts along the rotating speed axis, which is in this case around 4.5 times the nominal torque value for both of the machines. Higher peak torque levels can be achieved, but it requires more current to achieve a higher voltage to speed ratio to increase the flux linkage level.

The field weakening behaviour of both machines shows the saturation effect of inductances at high current values, which narrows down the field weakening region. In order to achieve better torque output, the current level has to be decreased as the speed increases. The torque production curves of the machines are presented separately in Figs. 3.31 and 3.32 in addition to the constant power curves.

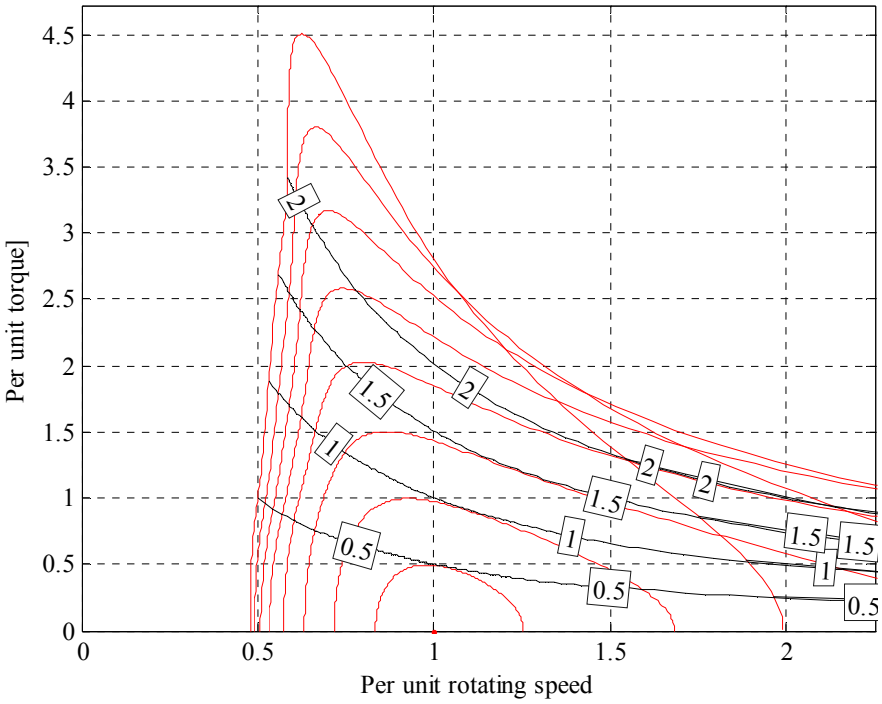

Fig. 3.31. Torque production curves of the MM structure based on the inductance values of the saturation model. The red curves are torque curves for currents 0.5, 1, 2, 3 and 4 p.u. The black labelled contour lines are torque curves for constant power in per unit values. The back electromotive force and supply voltage are 1 p.u.

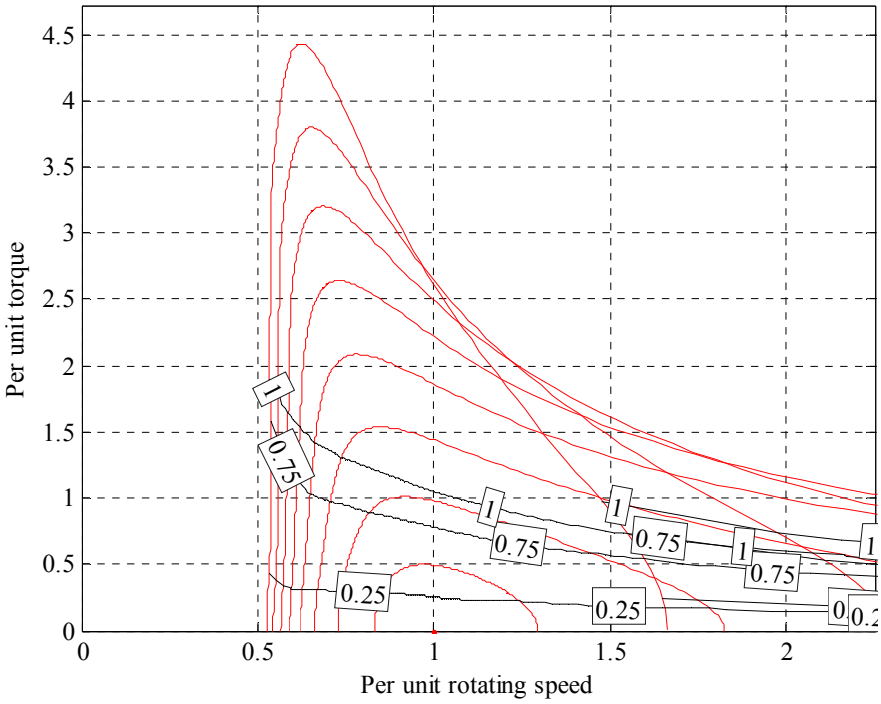

Fig. 3.32. Torque production curves of the EM structure based on the inductance values of the saturation model. The red curves are torque curves for currents 0.5–4 per unit at 0.5 per unit steps. The black labelled contour lines are constant power curves in per unit values. The back electromotive force and supply voltage are 1 p.u.

According to the analytical evaluation, the field weakening characteristics of both machine types are sufficient for the given application when considering the nominal point operation. The EM machine field weakening characteristics are slightly better around nominal current values as a result of the larger direct-axis inductance value when compared with the MM design. Nevertheless, the field weakening characteristics of the machines seem to be sufficient for the given application.

Now, our only concern is the low battery voltage. The torque production curves as function of rotating speed for 0.25 p. u. supply voltages are presented in Fig. 3.33.

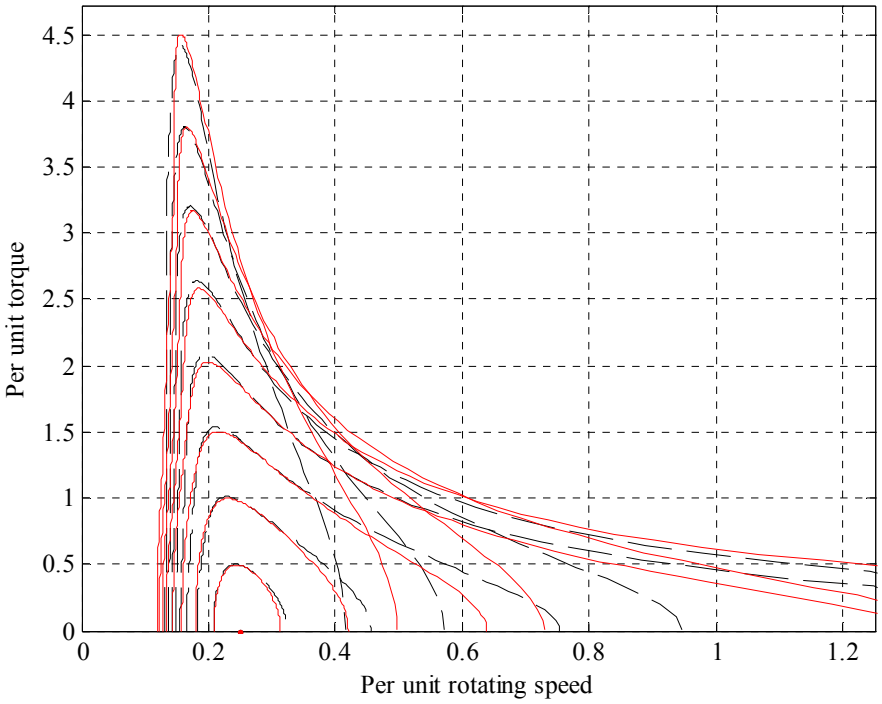

Fig. 3.33. Comparison of torque production at currents 0.5–4 per unit at 0.5 per unit steps. The solid line is for the MM machine and the dashed line for the EM machine. The figure shows the available maximum torque when the permanent magnet flux is 1 per unit and the supply voltage 0.25 p.u.

With the 25 % supply voltage level, the machines are is still capable of producing peak torque of 4.5 times the nominal torque, but the nominal speed requires over 50 % of excess current. This supply voltage level is too low compared with the cut of level of the Altairnano 50 Ah cell, the cut-off voltage of which is about 60 % of the normal operating voltage of 374 V line-to-line. However, a low voltage level can lead to problems with the thermal endurance if this is not taken into account in the design process. Thus, in the traction machine design process, it is necessary also to take into account the thermal characteristics of the machine.

3.3 Time stepping analysis

Transient magnetic analysis allows a more detailed evaluation of the machine performance over the operating speed range. It allows the determination of the iron and Joule losses and currents to define the efficiency and power factor. Time stepping analyses are conducted with voltage-fed models and sinusoidal voltage waveforms. The drawback of a sinusoidal supply waveform is the optimistic estimate of the loss behaviour under different load conditions. PWM-fed machines tend

to have a higher loss generation because of the increased harmonic content of the supply. A finite-element-based loss analysis is discussed in detail in Chapter 4.

3.3.1 Voltage-fed dynamic model

In the finite element analysis, the voltage-fed model gives more accurate values for the breakover torque. This calculation includes the analytically determined end-winding leakage component calculated in Section 3.2.2. Even though the end-winding leakage component is small, the leakage component becomes relatively significant in the torque output analysis because the PM machine synchronous inductances are low. The transient calculations are carried out by assuming a 120 °C temperature for both of the machines. The transient magnetic torque production including the end-winding leakage component for the 150 V line-to-line supply at a 1000 min^{-1} rotating speed is presented in Fig. 3.34.

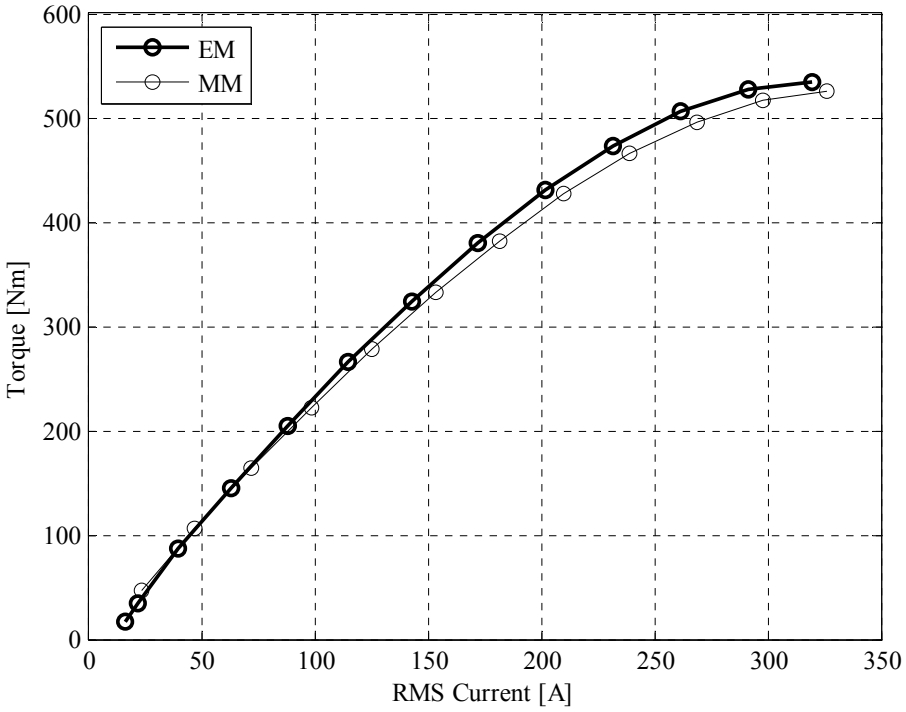

Fig. 3.34. Torque production as a function of current with a transient-voltage-driven simulation at a 1000 min^{-1} rotating speed and a 150 V line-to-line supply voltage.

Compared with the static current model, the torque curve starts to bend after the 200 A supply current. The peak value of torque is achieved around 300A of supply current. An increase in the torque output requires a higher supply voltage as Eq. 1.2 suggests. In the MM configuration, the flux starts to shift in the q-axis direction as the static model predicts. In the EM structure, the PM

flux tends to bend against the q-axis and short circuit with the adjacent pole. This effect is less intense in the MM structure because of the air gap path. To achieve higher torque ratings, the supply voltage has to be increased.

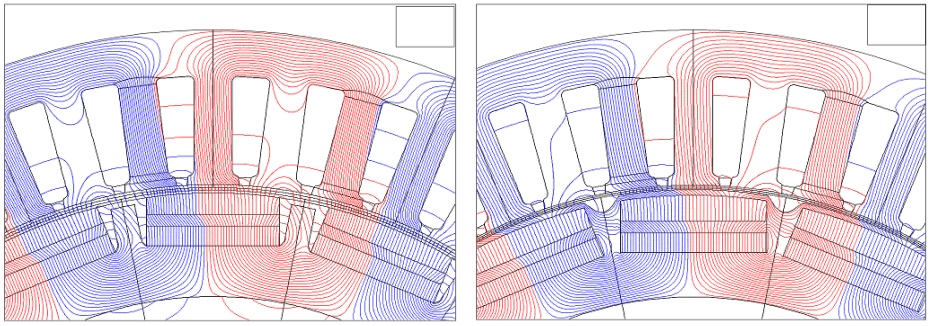

Fig. 3.35. Flux paths of the MM (left) and EM (right) configurations at the $150V_{LL}$ and 200 A supply.

The breakover point of torque production at the 150 V supply is reached just below a current of 300 A with both of the machines at 1000 min^{-1}. This means that the machines can only produce a torque maximum around 500 Nm with a 300A excitation current at the 150 V line-to-line supply voltage. An optimal current angle to produce a higher torque cannot be achieved without increasing the supply voltage. To achieve higher pull-out torque levels, there has to be voltage reserve designed in the system to reach the benefits from the reluctance torque component as presented in Section 1.3.

3.3.2 Short-circuit endurance

Because of the low direct-axis synchronous inductance, the sustained short-circuit current of a PM machine tends to be large. The short-circuiting current can cause a large enough demagnetizing flux in the d-axis direction to permanently demagnetize the magnets. The MM configuration is especially vulnerable as there is no iron in the d-axis direction to saturate and protect the magnet closest to the air gap. The EM configuration has thus better opportunities to withstand short circuits.

Magnets can be protected by selecting the magnet grade carefully, which means choosing grades without the 3rd quadrant remanence knee, but this usually leads to larger machine dimensions, because the magnets having some counter-magnetization resistance have lower energy products compared with the high B_r grades. A suitably high stator leakage also helps to protect the magnets as it decreases the demagnetizing flux of the machine.

To observe the short-circuit endurance of the machine structure, a three-phase short circuit evaluation was carried out in a Flux2D environment. Short circuit is applied to all three phases in no-load conditions of a generator. The short-circuiting is timed to take place in a point where one line-to-line voltage sign is changing from negative to positive. This time period results in the highest peak in the short-circuiting current in that particular phase. Short circuit currents are presented in Fig 3.36.

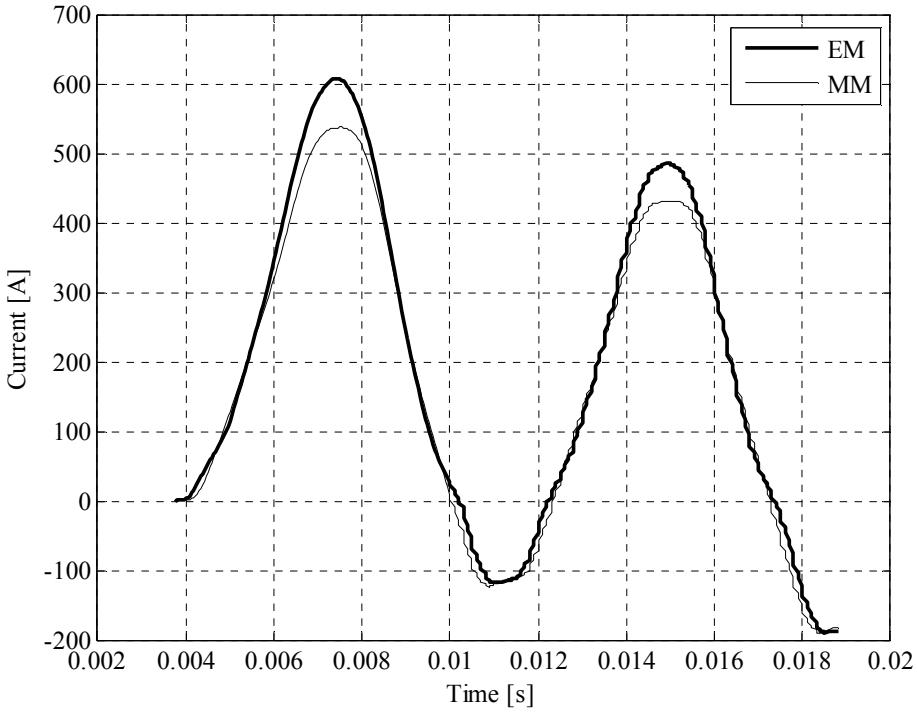

Fig. 3.36. Three-phase short-circuit currents at 1000 min^{-1} speed for the MM and EM structures. Waveforms include DC offset since the short circuit starts at peak flux linkage.

The peak currents are 607.5 A for the MM machine and 537.0 for the EM machine. The short circuits current peaks occur at 4.0 ms and 3.67 ms after the initialization of the short circuit. The flux density graphs of the short circuit for the MM and EM configurations for the corresponding time periods are presented in Fig. 3.37.

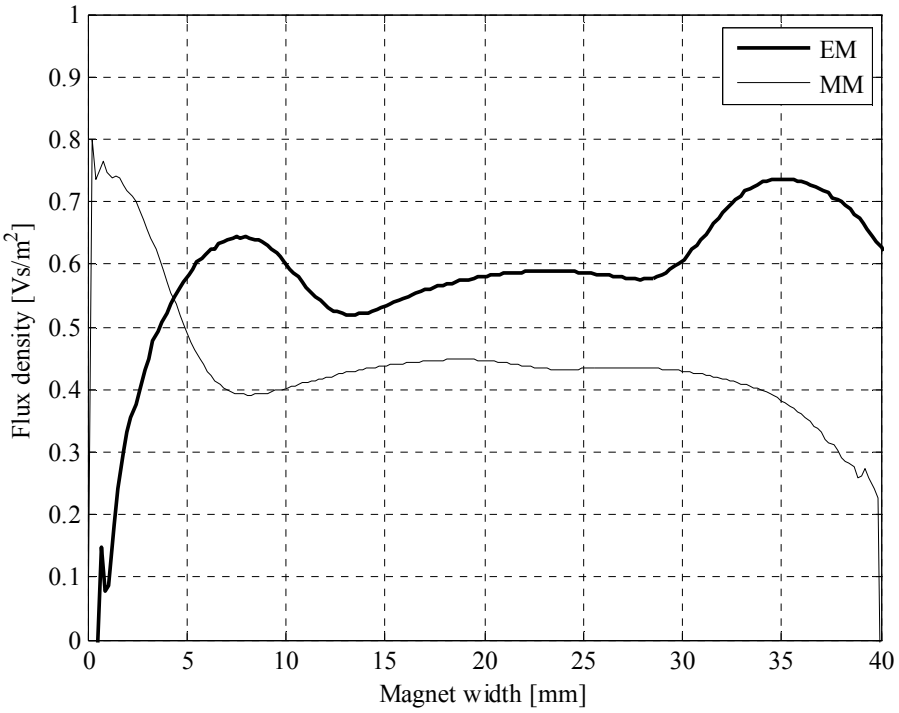

Fig. 3.37. Three-phase short-circuit flux density graph of the magnet surfaces of the MM and EM configurations according to the Flux 2D simulation. The flux densities are given in normal direction on the surface of the magnet closest to the air gap.

With the selected Ne493a grade for the MM configuration, at least partial demagnetization is inevitable if the magnet temperature exceeds 150 °C as shown in the data sheet in Fig 3.12. The Ne753a grade of the EM configuration is more sensitive to the temperature because of the higher B_r as shown in Fig 3.13. Thus, the EM configuration can only handle three-phase short circuits below magnet temperatures of 100 °C. The leading edge of the EM magnet suffers most. Interestingly, the highest stress occurs at the lagging edge of the MM structure. According to the short-circuit analysis, it would be beneficial to replace the magnet grade of the EM configuration to a more temperature tolerant grade. Nevertheless, in both cases, a long-term short circuit will eventually demagnetize the magnets as the magnets heat up.

3.4 Thermal network

An analytical thermal model was developed to study the thermal properties of the machine in steady-state operation. The model was extended to allow dynamic observation over time. Temperature modelling is essential in PM structures owing to the temperature sensitivity of the PM material in general. A dynamic model is needed to validate the machine performance even for

highly arbitrary load cycles, in which constant operating values are repeatedly exceeded. This applies especially to mobile solutions.

The developed analytical model includes 38 nodal points. The distribution of nodal points across the geometry is presented in Appendix II.

The nodal points are distributed as follows:

- 5 in the stator core,
- 5 in the windings,
- 1 in the annulus,
- 6 in the magnet pole,
- 3 in the rotor core,
- 3 in the axle,
- 4 in the bearings,
- 6 in the end shields,
- 3 in the frame and
- 2 in the end space.

The model is basically in the 2D form in addition to the axial heat flow paths in the frame, shaft and windings. The main heat flow path is in the radial direction through the laminate stacks because the insulation layer of the laminate sheets prevents the heat flow in the axial direction. The stator frame shell area is divided into two parts in the radial direction. The axial conductivity in the laminate stacks is neglected because the magnitude of axial heat conduction is negligible compared with the heat conduction in the radial direction.

In order to match the thermal resistances of the teeth and rotor pole area with the circular resistance elements, the radial thermal resistances of the teeth area are divided by the slot number because of the parallel heat flow paths in the tooth and slot region. The same applies to the slot axial resistances owing to the parallel heat flow paths in the axial direction. The radial thermal resistances of the rotor pole area are divided by the pole number for the same reason.

3.4.1 Frame region and end-winding space

Half of the frame is treated as a fluid cooling surface area and half as a natural-convection-affected surface in parallel with the previous according to (Richter, 1962) as

$$\alpha_{\text{natural}} \approx 6.5 + 0.05(T_{\text{s}} - T_{\infty}) \qquad 3.6$$

where

- T_s is the object surface temperature and
- T_∞ is the temperature of the surrounding medium.

The equation of natural convection is also applied to both end-shield surfaces. The thermal resistances of the frame, stator and rotor yoke and rotor shaft in the radial direction are modelled by Eq. 2.34. The placement of temperature nodes in the frame region is presented in Fig. 3.38.

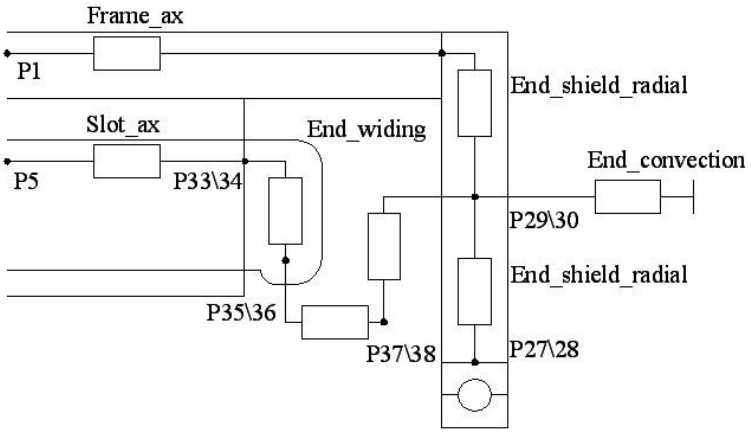

Fig. 3.38. Temperature node placement in the frame region. The duplicate numbering of the nodal points refers to the corresponding numbering in each end of the machine. The whole thermal network is presented in APPENDIX II.

End shields are also modelled as cylindrical plates with one node at each end of the machine. The axial thermal resistance is also taken into account. The bearings are modelled in the radial direction only. Because of the complicated structure of the bearing, the radial thermal conductivity is taken into account as an equivalent air gap of 0.3 mm as suggested by (Staton et al., 2005). The nodal point arrangement for bearings is presented in Fig 3.39. The contact resistance to the end shield and shaft are also modelled as air on the inner and outer race surfaces.

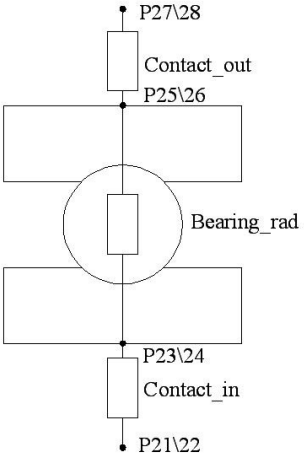

Fig. 3.39. Thermal resistance displacement of a bearing.

3.4.2 Teeth and slots

The tooth area is divided into four parts, rectangular in the tooth tip and body and trapezoidal in the tooth bottom and neck as presented in Fig. 3.40. The calculation of these thermal resistances applies Eqs. 2.35 and 2.36.

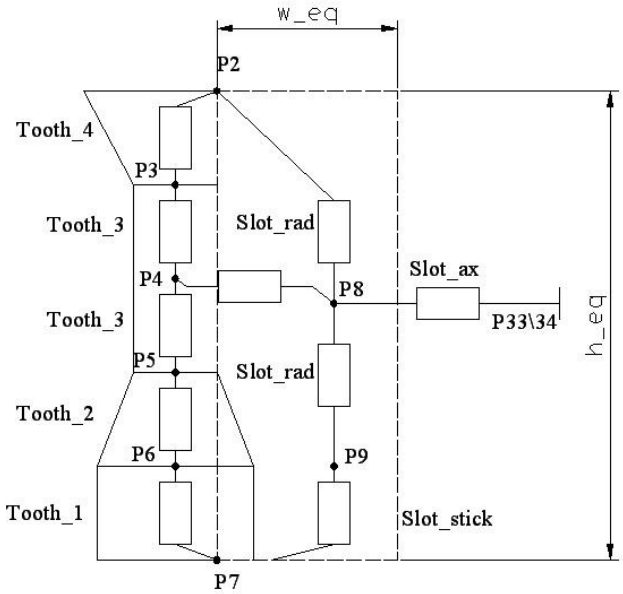

Fig. 3.40. Thermal resistances of the slot and tooth areas. The whole thermal network is presented in APPENDIX II.

This information can be used to determine the equivalent numbers of parallel strings in slots in the corresponding directions. Equivalent slot dimensions are calculated by applying the dimensions of Fig. 3.5 to Eqs. 3.2 and 3.3. The number of conductors in the slot height is thus

$$n_{\mathrm{h}} = \frac{h_{\mathrm{eq}} n_{\mathrm{strings}}}{w_{\mathrm{eq}}} \tag{3.7}$$

and

$$n_{\mathrm{w}} = \frac{n_{\mathrm{strings}}}{n_{\mathrm{h}}} \tag{3.8}$$

for the number of conductors in the length of slot width. The equivalent resistances in the slot height and slot width (in other words, radial and tangential directions, respectively) can be calculated as

$$R_{\mathrm{slot,radial}} = \frac{n_{\mathrm{h}}}{k_{\mathrm{Cu}} n_{\mathrm{w}} l_{\mathrm{Fe}}} + \frac{h_{\mathrm{eq}} - n_{\mathrm{h}} d_{\mathrm{string}}}{\lambda_{\mathrm{impr}} n_{\mathrm{w}} l_{\mathrm{Fe}}} + \frac{2h_{\mathrm{slot,ins}}}{\lambda_{\mathrm{slot,ins}} w_{\mathrm{eq}} l_{\mathrm{Fe}}} \tag{3.9}$$

and

$$R_{\mathrm{slot,tangential}} = \frac{n_{\mathrm{w}}}{k_{\mathrm{Cu}} n_{\mathrm{h}} l_{\mathrm{Fe}}} + \frac{w_{\mathrm{eq}} - n_{\mathrm{w}} d_{\mathrm{string}}}{\lambda_{\mathrm{impr}} n_{\mathrm{h}} l_{\mathrm{Fe}}} + \frac{2h_{\mathrm{slot,ins}}}{\lambda_{\mathrm{slot,ins}} h_{\mathrm{eq}} l_{\mathrm{Fe}}} \tag{3.10}$$

respectively. Because the thermal resistances represent the thermal resistance in the tangential direction for the whole width of the slot, the tangential thermal resistance has to be divided by two as every slot has one tooth in parallel with each other. Thus, the heat passage length is half of the slot width in average. In addition to the slot radial and tangential direction, there has to be a thermal contact resistance added to the heat path because the impregnation leaves air pockets in the coil sides (Kylander, 1995) and (Saari, 1995). These can be modelled as small air gaps. The lengths of typical contact region air gaps are presented in Table 3.3.

Table. 3.3. Suggested air gaps in the thermal contact area (Saari, 1995), (Kylander, 1995).

Material	Equivalent air gap length [μm]
Winding to core	100–300
Cast iron frame to stator, or more than 100 kW	50–80
Aluminum frame to stator, or less than 100kW	30–40

Windings are divided into five different nodal points. Three nodes are placed in the stator core; one in the centre and one in each end of the stator stack. The last two nodes are for the end windings as presented in Figs. 3.38 and 3.40.

Axial heat flow is evaluated for the copper only because the heat-carrying capability of the impregnation material is considerably lower compared with the copper. The copper area is calculated with the actual copper turn number according to

$$S_{\mathrm{Cu}} = 0.25 z_{\mathrm{Q}} n_{\mathrm{parallel}} \pi {d_{\mathrm{string}}}^2 \qquad 3.11$$

where

- z_{Q} is the number of coil turn sides in one slot,
- n_{parallel} is the number of parallel strings in the coil turn and
- d_{string} is the diameter of one string.

Thus, the axial thermal resistance of a single coil is

$$R_{\mathrm{Cu,axial}} = \frac{l_{\mathrm{Fe}}}{k_{\mathrm{Cu}} S_{\mathrm{Cu}}} \qquad 3.12$$

The end-winding axial resistance is calculated similarly, but the end-winding length is calculated from the equation

$$l_{\mathrm{end}} = 1.2\tau_{\mathrm{p}} + 0.05\,, \qquad 3.13$$

which is an experimental formula for the end-winding length (Vogt, 1983). The result has to be multiplied by 0.5 to obtain the thermal resistance in the middle of the end winding loop.

3.4.3 Air gap region

The evaluation of the air region thermal resistances is based on the Taylor number *Ta*, which describes the heat exchange (convection and conduction) between two concentric cylinders, in which the inner cylinder rotates. If no axial flow is present, the annulus flow is usually quite laminar. The transition to turbulent flow begins at higher rotating speeds. Equation for the calculation of the Taylor number according to (Becker et al., 1962) is

$$Ta = \frac{\Omega^2 r_\delta \delta^3}{\nu^2 F_{\mathrm{g}}} \qquad 3.14$$

where

- Ω is the mechanical angular speed,
- r_δ is the average air gap radius,
- δ is the air gap length,
- ν is the kinematic viscosity of the air gap fluid and
- F_g is a correcting factor depending on the cylinder dimensions.

F_g can be neglected in practical cases where the air gap length is considerably smaller compared with the rotating radius ($\delta/D_r<0.1$). Taylor numbers beyond 1740 are considered as a turbulent region (Becker et al., 1962). In this region, the Nusselt number is described as

$$Nu = 0.409Ta^{0.241} - 137Ta^{-0.75} \quad 3.15$$

At lower Taylor numbers, the value of the Nusselt number is considered to be Nu =2 (Becker et al., 1962). The convection coefficient from the stator to the rotor over the characteristic length of air gap is

$$\alpha_\delta = \frac{k_f Nu}{2\delta}. \quad 3.16$$

Radiation is not taken into account because the effect is negligible as a result of the small temperature difference between the rotor and stator surfaces.

3.4.4 Rotor region

A rotor model allows modelling of the embedded and module magnets. The ‘pole shoe’ area is neglected in the magnet module design. The magnets are modelled with rectangular elements having nodal points at the top and bottom of the magnets. The arrangement is presented in Fig. 3.41.

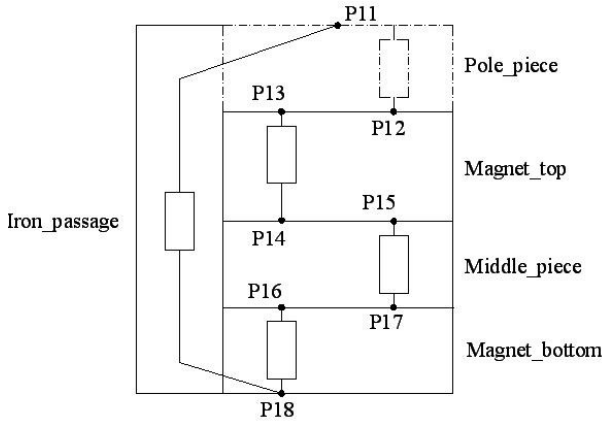

Fig. 3.41. Thermal resistances of a pole region. In the EM structure there is a thermal resistance of the pole shoe. In the MM structure instead, the thermal resistance is considered zero. The thermal contact areas between the node pairs 12–13, 14–15 and 16–17 are taken into account as adhesive joints in the MM structure and as air gaps in the EM structure. The iron path acts as a short-circuit path of heat flux for each pole.

There are also contact resistance areas for magnet surfaces. The thermal contact area in the magnet module machine is modelled as an insulation layer of 200 μm in thickness. This area is replaced by air in the embedded magnet structure. The magnet pole also has a side path for heat flux in the quadrature-axis direction, modelled with a rectangular element in both structures. The tangential thermal conductivity of the rotor is neglected in the model.

3.5 Results of the thermal modelling

The developed lumped thermal model is used to predict the thermal behaviour of the machine in different load conditions. The model analysis is divided into time-dependent and steady-state analyses. The steady-state analysis provides fast evaluation of temperatures in static load conditions but does not give information about the transient characteristics. With a transient model, it is possible to evaluate the machine endurance for specific load cycles, in which the rated values are repeatedly exceeded. The losses are evaluated by the Flux 2D program and applied to specific nodes of the thermal model.

3.5.1 Steady-state analysis

Knowledge on material parameters is important in thermal modelling. In general, the list of materials is quite short. The thermal conductivities of metals vary between 20 and 30 W/Km depending on their silicon content (Miller, 1994). Lower thermal conductivity values are related to a higher silicon content. In this analysis, the thermal conductivity of the sheet metal is set to 30

W/Km as there were no accurate data available of the specific grade used in this study. The thermal conductivity of electric steel is highly dependent on the silicon content of the steel along with the electrical conductivity. Electric steels of low specific loss values have a higher silicon content to reduce the steel resistivity in order to decrease the eddy current losses. A high silicon content has the same effect on thermal conductivity.

The thermal characteristics of aluminium are difficult to model since physical properties vary according to the material grade. The thermal conductivity of cast aluminium is around 140 W/Km, but certain alloys are close to the 200 W/Km rating of pure aluminium (Miller, 1994), (Incropera, 2007). The alloy for the frame and rotor shaft is tool aluminium, which has a typical thermal conductivity of 180 W/Km.

Insulating sheets and adhesives usually have thermal conductivity values around 0.2 to 0.3 W/Km. For slot impregnation resins, thermal conductivities around 0.2 have been reported for polyethylene compounds. More expensive epoxy resins can reach 1 W/Km values and above.

Material-specific data for thermal conductance calculations are presented in Tables 3.4 and 3.5.

Table. 3.4. Material-specific data for thermal conductance calculations.

Material	Thermal conductivity [W/Km]
Sheet metal	30
Copper	385
Aluminium	140
Slot impregnation	0.2
Slot insulation	0.2

The thermal conductivities of solid materials are not updated according to the temperature because the accurate temperature behaviour is not known for the industrial grade materials. Previous studies on the thermal performance of electrical machines have shown good agreement of the models with the selected material parameters (Rilla, 2006).

The air properties (thermal conductivity, density, kinematic and dynamic viscosity) are updated according to the temperature because air properties are sensitive to the prevailing temperature. The effect is significant in the thermal conductivity joints and especially in the air gap region. The thermal conductivity of air as a function of temperature is presented in Fig. 3.42.

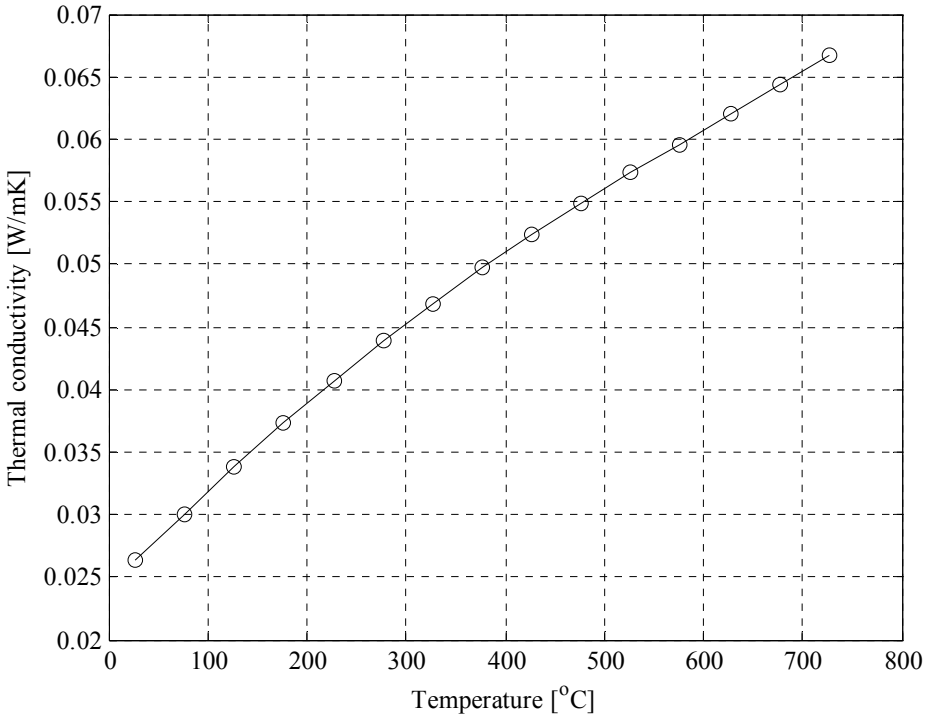

Fig. 3.42. Thermal conductivity of air as a function of temperature.

Table. 3.5. Physical properties of air at the 100 °C temperature.

Quantity	Thermal conductivity	Unit
Thermal conductivity	0.032	$Wm^{-1}K^{-1}$
Density	0.95	$kg\ m^{-3}$
Kinematic viscosity	$23.06 \cdot 10^{-6}$	$m^2\ s^{-1}$
Dynamic viscosity	$21.9 \cdot 10^{-6}$	$kg\ m^{-1}s^{-1}$

The model is tested for a rated speed of 1000 min^{-1} and a 25 kW load. The loss distribution is based on the Flux 2D analysis. Copper losses are estimated analytically. The loss data for the thermal model are given in Table 3.6.

Table. 3.6. Estimated loss data in the rated point for the MM and EM structures at the 120°C temperature.

Loss data	MM [W]	EM[W]
Copper loss	1231	1231
Stator core loss	54	53
Tooth losses	90	104
Top magnet loss	35	36
Lower magnet loss	6	1
Middle piece	2	4
Rotor yoke loss	7	24
Bearing losses (SKF)	237	237
Additional losses	126	126
Total	1786	1814

According to the Flux 2D and analytical calculations, the loss behaviour seems similar in both machines. The main difference seems to lie in the magnet Joule losses and the rotor core losses. Surprisingly, the top-mounted magnets seem to have almost an equal amount of losses. In the actual machine, the magnet close to the air gap in the magnet module is slitted to decrease the losses. The absence of core material in the d-axis direction causes additional stress to the lower magnet of the MM structure compared with the EM structure. According to the IEC standard, the additional losses for the output power of 25 kW are 125.7 W. The bearing losses are estimated according to the SKF calculators for a given bearing type. It was noted that lubrication viscosity has a slight effect on the bearing friction losses in the sealed bearing structure. The embedded magnet machine has through-ventilation channels in the end-shield region. This is taken into account by applying convective cooling to the end-winding space node with the air fluid data values of the average temperature between the ambient and machine inner air space. The ambient air temperature is considered to be 25 °C and cooling fluid temperature 35 °C.

The results of the steady-state model according to Table 3.6 loss data are presented in Table 3.7.

Table. 3.7. Temperature rise of the steady-state thermal model at rated values.

Temperature node	MM[°C]	EM [°C]
Slot middle	85.1	53.6
Coil end	90.6	56.9
Stator yoke	45.0	26.2
Tooth middle	55.5	36.8
Top magnet	60.2	59.0
Rotor yoke	61.1	59.3
Inner air	54.5	29.9

The estimated machine temperatures show clearly the benefit of the through-ventilated structure. According to the evaluation, the machine operates within safe temperature limits at the rated speed and torque. The model was used to determine the maximum load value for the machines within the temperature limits. The windings of the machine are designed for a 155 °C limit. At a 140 A current, the EM structure reaches the winding temperature limit. In this point, the magnets are approximately in a 125 °C temperature. The MM structure, on the other hand, meets the winding temperature limit at a 112 A current. However, the magnets are at a much lower temperature of 115 °C in this point. The analytical prediction of thermal characteristics shows that the machine dimensioning should be at the safe side.

3.5.2 Transient analysis

In addition to the thermal conductance matrix of the static model, a thermal capacitance matrix was generated. The capacitance matrix is built as a diagonal matrix according to Section 2.3.5.

Only solid materials are taken into account because the thermal capacitances in the air region are considerably smaller. The material data needed to construct the matrix are presented in Table 3.8.

Table. 3.8. Material parameters for thermal capacitance calculations.

Material	Specific heat capacity at 100°C [$Jkg^{-1}K^{-1}$]	Density [kg m^{-3}]
Sheet metal	450	7600
Copper	385	8960
Aluminium	900	2700
Slot impregnation	2100	900
Insulation	2100	900

Iteration is carried out by a 2^{nd}-order Adams-Moulton method, as it is suggested to be fast and stable tool for the analysis of thermal gradient (Kylander, 1995). The results of the dynamic model according to the MM and EM structure are presented in Fig. 3.43. The loss data are taken from Table 3.6.

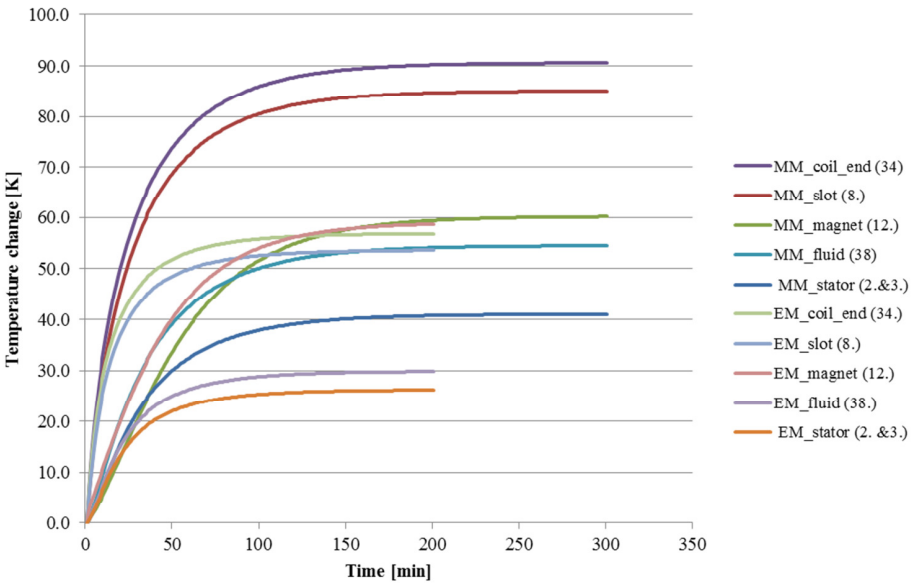

Fig. 3.43. Temperature rise in K of different machine parts according to the transient analysis for the MM and EM structures at rated values. The loss values are based on Table 3.7. The numbers in brackets are the corresponding node numbers of the applied thermal model.

The cooling arrangement of the EM structure shows a clear benefit related to the temperature change. The time constant of the EM structure for the temperature stabilization is also considerably lower compared with the totally enclosed structure of the MM machine, as expected. The corresponding time constants for the coil end temperature are ~55 minutes for the MM machine and ~46 minutes for the EM machine.

3.5.3 Sensitivity of the developed model

The sensitivity of the analytical thermal model is inspected by varying the thermal conductivities of materials and referring them to the selected values. The selected thermal conductivities provided in Table 3.5 have shown good agreement in previous machine studies (Rilla, 2006). The material parameters should nevertheless be selected carefully, and the sensitivity of the model should always be checked by varying the material parameters. Additional care has to be taken in the selection of the insulating material parameters. This is clearly seen in Table 3.9, where the effects of thermal conductivities on the slot temperature node are given.

Table. 3.9. Table for winding temperature estimation depending on the selected thermal conductivity of the material. The resulting temperature difference is presented for each material separately.

Material	Thermal conductivity range [W/mK]	EM-slot temperature [°C]	ΔT [°C]	SM-slot temperature [°C]	ΔT [°C]
Copper	360–400	84.7–84.6	0.1	119.1	-
Electric sheet	20–40	87.5–83.0	4.5	125.0–115.9	4.1
Slot_insulation	0.2–0.3	84.6	-	119.1	-
Slot_impregnation	0.2–0.6	84.6–76.9	7.7	119.1–100.8	18.3
Frame	140–200	84.6–84.5	0.1	119.1–118.3	0.80
All high - All low	-	87.5–74.8	12.7	125.0–96.9	28.1

According to the results of Table 3.9, the selection of the thermal conductivity of the slot impregnation has the highest influence on the model results. The low conductivity values refer to typical polyester resins. High 0.6 W/mK values are achievable with more expensive epoxy resins. The thermal conductivity of the slot insulation sheet seems to have a negligible effect on the temperature distribution. The EM structure has lower temperature changes as a result of the through-ventilated structure. This can be seen clearly in the changes in the slot impregnation conductivity. The second highest influence on the temperatures is the thermal conductivity of the sheet metal.

3.6 Conclusions on the machine design

According to the thermal analyses made on the structures, the proposed design methods resulted in two functional machine structures.

The performance analysis by two-axis model inductances is only indicative for these machine types. A comparison between the finite element method and the analytical approach shows the weakness of the traditional analytical model, which does not take into account the armature reaction accurately because the direct- and quadrature-axis inductances obtained from the Flux 2D calculation for the d- and q-axes individually do not describe the magnetic state of the machine correctly.

The enhanced method with the cross-saturation gives better results. Thus, finite-element-based methods are needed for the more accurate machine performance estimation of these machine types. Care must be taken because an accurate control of parameters in the voltage- and current-fed models is not possible. Therefore, an iterative approach is mandatory in the design process. The voltage levels and load angles have to be varied to find an optimum current angle.

The magnet module design seems to suffer from mechanical problems in the magnet fixing. Thus, the embedded machine structure is more favourable because of its better mechanical stability. The through-ventilated structure also shows benefits in cooling, and this should be considered in mobile applications as the traditional ICE solutions also have to be protected against environment.

The through-ventilated structure provides a higher steady-state load capability, and the lower temperature rise time constants allow a better dynamic performance.

4 Analysis of the experimental studies

A set of tests were performed for both machine types. The power output capability and thermal stress tests were performed to compare the performance of the machine structures. The test bench and the cooling arrangement were the same for both of the machines.

To simulate the cooling arrangement of a moving machine, the cooling of the machine was arranged with an aluminium heat exchanger and a 12 V_{DC} electric water pump with a measured flow of 0.12 kg/s. The heat exchanger was exposed to forced cooling with an auxiliary axial fan. The embedded magnet machine has additional cooling vents on both end shields for enhanced convection heat transfer. For comparison, the surface magnet module machine is a totally enclosed design. The surface magnet module and the embedded magnet machines are referred to from here onwards as an MM and EM, respectively.

4.1 Test set-up

The test set-up consists of two test machines, a three-phase 400 V and 355 kW ABB induction machine, a Magtroll 2000 Nm Torque meter, a Yokogawa PZ-4000 power analyser and a Fluke thermometer unit for the PT-100 temperature elements. Details of the test set-up are presented in APPENDIX I. The test set-up is shown in Fig. 4.1.

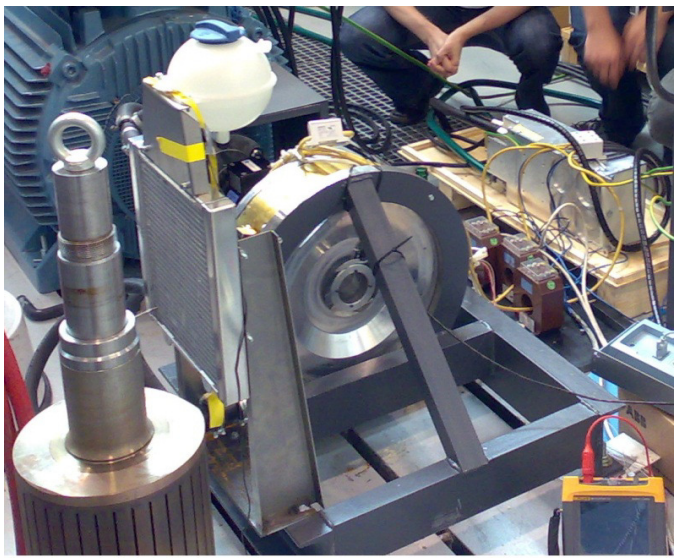

Fig. 4.1. Test set-up with the MM machine in the front, load machine in the back and heat exchanger on the left.

The results obtained are based on the frequency converter unit and the developed control method by Vacon Oy. The electrical values are obtained with the power analyser by applying a 1 s sampling time in the data capture.

4.1.1 Load analysis

The measured root mean square line-to-line back EMF values for the MM and EM machines, at the ambient temperature of 25 °C and 1000 min^{-1} rated speed, are 135.4 V and 154.3 V, respectively. The measurement was carried out by rotating the measured machine with a load machine and measuring the line-to-line voltage with a power analyser. The estimated value for the back EMF according to the finite element calculations at the rated speed of 1000 min^{-1} is 155.0 V for the MM machine and 159.9 V for the EM machine.

The difference in the EMF ratings is mostly due to the dimensioning error in the magnet module design caused by the end effect in the rotors, which is explained by the fact that the permanent magnet ends tend to short-circuit part of the main flux. Thus, the rotor length in the MM machine is too short. According to (Jussila, 2010), the physical length of a permanent magnet rotor should be the length of the stator stack plus two times the air gap length at each end of the machine. Thus, the machine rotor length should be

$$l_{\text{rotor}} = l_{\text{Fe}} + 4\delta \qquad 4.1$$

to match the effective stator core length. Consequently, the rotor flux is smaller than the optimum 150.0 V because of the length of 65 mm instead of the optimal 68 mm. This error was corrected in the EM machine dimensioning. An additional flux decrease is caused by the slitting of the surface magnet in the axial direction. The adhesive layers between the magnet pieces decrease the space factor of the magnet pole.

The difference shows directly in the load characteristics. The MM machine torque output is around 10 % smaller with currents of equal size when compared with the EM machine. Both machines are measured in motoring operation for 300, 700 and 1500 min^{-1} rotating speeds. In addition, the 2000 min^{-1} rotating speed is measured only for the EM machine because of the mechanical restrictions of the MM structure. The output power and torque of the machines are presented in Tables 4.1 and 4.2. The current values refer to the nominal current I_{n}=100 A.

Table. 4.1. MM machine power output and torque production given according to the rotating speed and the load current. The values highlighted by grey indicate the nominal point. The values are in [kW || Nm].

min^{-1}	**0.4I_n**	**0.6I_n**	**0.8I_n**	**I_n**
1500	12.1 || 77.0	18.85 || 120.0	25.29|| 161.0	X
1000	8.27 || 79.0	12.60 || 121.0	17.06 || 162.9	21.23 || 202.7
700	5.87 || 80.0	9.020 || 123.0	12.09 || 164.9	15.10 || 205.9
300	2.68 || 85.3	3.990 || 127.0	5.340 || 170.0	6.660 || 212.0

Table. 4.2. EM machine power output and torque production given according to the rotating speed and the load current. The values highlighted by grey indicate the nominal point in [kW || Nm].

min^{-1}	**0.4I_n**	**0.6I_n**	**0.8I_n**	**I_n**
2000	20.1 || 96.0	30.16 || 143.0	40.42 || 193.0	49.42 || 236.0
1500	15.1 || 96.0	22.77 || 145.0	30.33|| 193.1	38.01 || 242.0
1000	10.0 || 95.0	15.18 || 145.0	20.42 || 195.0	25.55 || 244.0
700	7.11 || 97.0	10.85 || 148.0	14.59 || 199.0	18.18 || 248.0
300	3.140 || 100.0	4.780 || 152.0	6.380 || 203.0	7.980 || 254.0

Because of the loss of the PM flux, the MM machine does not reach the rated 240 Nm torque at the nominal current rating as shown in Table 4.1. The EM structure, on the other hand, meets the required torque rating. The importance of the nominal point selection is also shown in the torque output characteristics. The torque production of the machines decreases quite significantly at the rated current when the operating speed increases. This is due to the decreasing back EMF as the magnets deteriorate thermally as a result of increasing losses as discussed later in Section 4.2.3. The steady-state torque production at the rated current for both of the machines is presented in Fig. 4.2 as a function of rotating speed.

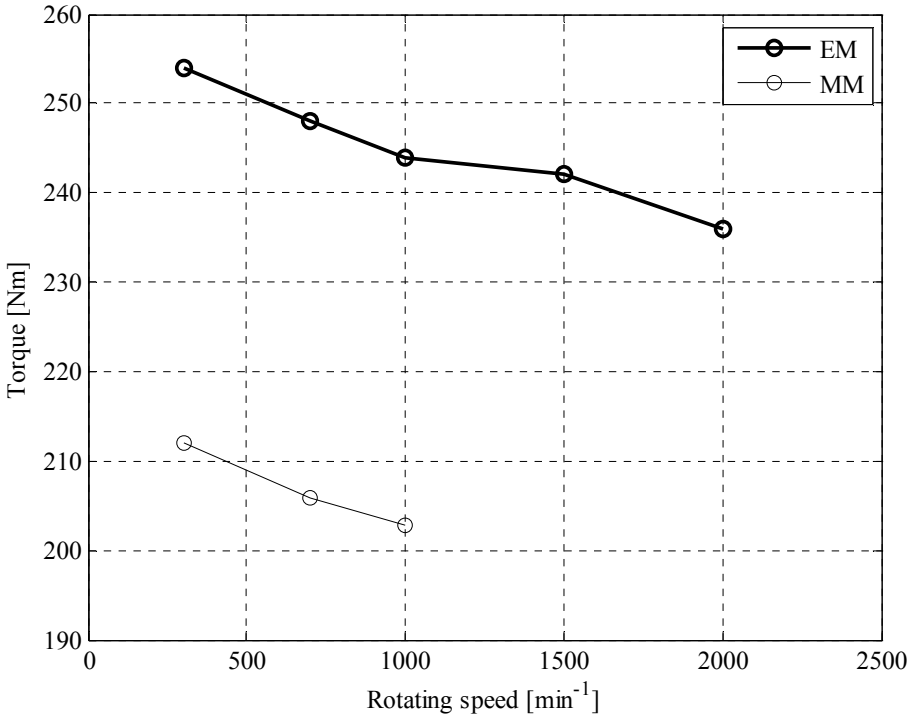

Fig. 4.2. Constant torque production of the machine, with the nominal voltage level and steady-state temperature, as a function of rotating speed at the nominal current according to the values in Tables 4.1 and 4.2.

The torque decay in the EM structure is around 7 % in the torque output when comparing with the 300 rpm and 2000 rpm values at the nominal current. The drop is caused by a decrease in the back EMF voltage caused by the increasing magnet temperature. According to Fig. 4.1, the torque decay rate of the MM configuration is about the same as with the EM structure.

The behaviour in Fig. 4.2 suggests similar loss distribution characteristics for both of the machine configurations. Additional peak torque test resulted in a 585 Nm maximum torque value for the MM machine and 660 Nm maximum value for the EM machine at the 320 A current. The percentage difference in the peak torque production is about the same as in the back electromotive measurement. The peak torques are low compared with the finite element results, which yield nearly 800 Nm values for both of the machines at the ~300 A current. According to the finite element calculations, the supply voltage should be about 1.5 times the back EMF voltage. Apparently, the frequency converter control method is not capable of producing an optimal current angle control in order to achieve the desired operation of the machine. According to the measured data, the machine operating state is presented as phasor diagrams in Figs. 4.3 and 4.4.

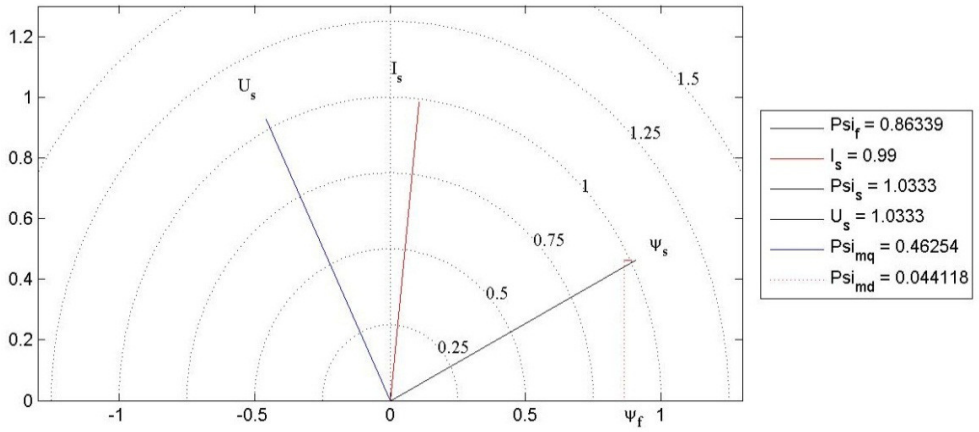

Fig. 4.3. Per unit phasor presentation of the MM machine at the 1000 min^{-1} rotating speed with nominal current and load. The power factor is 0.85.

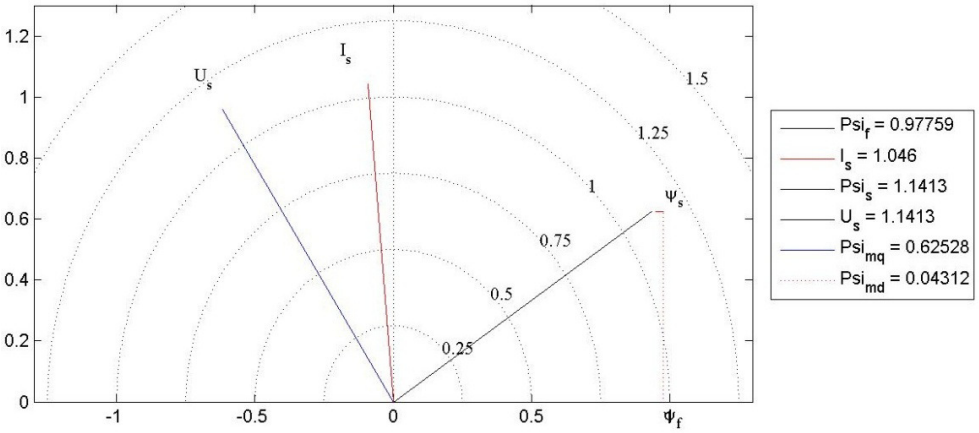

Fig. 4.4. Per unit phasor presentation of the EM machine at the 1000 min^{-1} rotating speed with nominal current and load. The power factor is cos φ = 0.88.

According to the measured data, the frequency converter drives the MM machine with the positive I_d current at the nominal operating values because of the low EMF voltage level. On the other hand, the EM machine is fed with a ~17 % excess voltage at the same torque reference.

4.1.2 Efficiency and loss analysis

Machine efficiencies are calculated from the measured input and output powers of the machines. The low voltage level causes the dominating effect of Joule losses in the machine efficiency ratings. The efficiency values are presented in Tables 4.3 and 4.4 according to the rotating speed

and current. The 1500 min^{-1} speed full current values for the MM machine were not measured because of a motor failure.

Table. 4.3. Measured MM machine efficiency at different rotating speeds and currents.

min^{-1}	**$0.4I_n$**	**$0.6I_n$**	**$0.8I_n$**	**I_n**
1500	0.91	0.93	0.93	-
1000	0.91	0.92	0.92	0.91
700	0.90	0.91	0.90	0.89
300	0.89	0.87	0.85	0.82

Table. 4.4. Measured EM machine efficiency at different rotating speeds and currents.

min^{-1}	**$0.4I_n$**	**$0.6I_n$**	**$0.8I_n$**	**I_n**
2000	0.98	0.96	0.96	0.94
1500	0.97	0.96	0.95	0.94
1000	0.96	0.95	0.95	0.93
700	0.95	0.95	0.94	0.92
300	0.93	0.92	0.87	0.86

The measured efficiencies of the MM machine in different load and speed conditions are quite poor for a permanent magnet machine. Even though the efficiencies of the MM structure are lower compared with the EM configuration, the absolute losses are very close to each other. The total heat dissipations of the machines are presented in Tables 4.5 and 4.6.

Table. 4.5. Total loss dissipation of the MM machine in [W].

min^{-1}	**$0.4I_n$**	**$0.6I_n$**	**$0.8I_n$**	**I_n**
1500	1220	1360	1780	-
1000	830	1140	1470	1980
700	680	910	1290	1830
300	330	610	950	1480

Table. 4.6. Total loss dissipation of the EM machine in [W].

min^{-1}	**0.4I_n**	**0.6I_n**	**0.8I_n**	**I_n**
2000	500	1150	1700	3420
1500	480	940	1610	2310
1000	390	740	1150	1880
700	350	530	870	1480
300	220	421	910	1330

There is inconsistency in the measurement results at low current values. The measured torque values are so low that the accuracy of the 2000 Nm torque transducer causes problems. This can also be observed from the curve. The machine efficiencies according to Tables 4.3 and 4.4 are presented in Figs. 4.5 and 4.6, respectively.

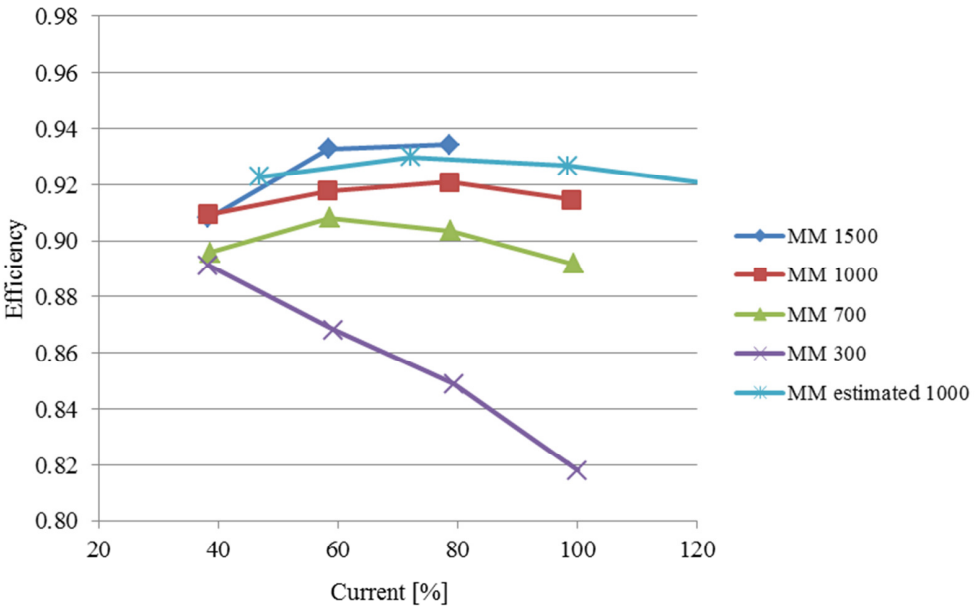

Fig. 4.5. MM machine efficiency according to Table 4.3 with the estimated efficiencies at the 1000 min^{-1} rotating speed.

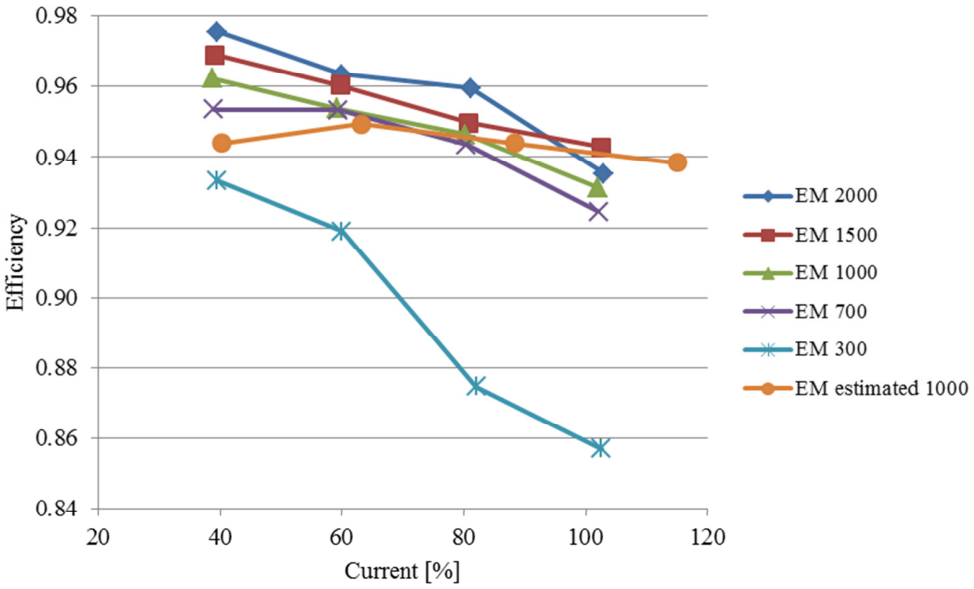

Fig. 4.6. EM machine efficiencies according to Table 4.4 with the estimated efficiency at the 1000 min^{-1} rotating speed.

The EM machine efficiency is higher at low current values as expected. The closed design on the other hand has more arc in the efficiency curves because of the restricted heat removal. The heat removal to the cooling fluid decreases at lower loss values as a result of the decreasing temperature difference. The measured losses at 1000 min^{-1} and the 100 A current are close to the estimated loss values presented in Table 3.6.

4.2 Thermal characteristics

Machine temperatures were measured according to the load points presented above. The results are compared with the developed thermal model in order to verify the validity of the model. The steady-state properties are important for the model accuracy, but a more important aspect is the dynamic performance in varying load conditions. The physical parameters for the modelling are the same as presented in Table 3.5 in Section 3.5.1. The specific heat capacities of the dynamic model are the same as in Table 3.8.

4.2.1 Steady-state temperatures

As expected, the temperature behaviour of the machines seems to be similar, but the benefit of the ventilated structure of the EM machine starts to show at the 700 min^{-1} speed. The temperature rises of the MM and EM machines are presented in Tables 4.7 and 4.8, respectively.

Table. 4.7. Measured end-winding temperatures of the MM machine in °C.

min^{-1}	**0.4I_n**	**0.6I_n**	**0.8I_n**	**I_n**
1500	64.5	79.2	101.7	-
1000	59.9	71.8	94.6	128.2
700	51.6	66.4	89.0	120.8
300	42.9	58.0	82.2	114.9

Table. 4.8. Measured end-winding temperatures of the EM machine in °C.

min^{-1}	**0.4I_n**	**0.6I_n**	**0.8I_n**	**I_n**
2000	56.4	65.6	80.0	100.7
1500	51.4	61.1	76.3	99.4
1000	48.0	59.0	76.4	101.4
700	44.6	56.7	76.3	105.4
300	40.1	54.0	76.2	108.7

Table 4.7 shows that the temperature rise occurs as expected. The load point at 1500 min^{-1} and 100 % torque was not measured to protect the magnets from overheating because no information about the magnet surface temperature was available during the measurement, and the 700 min^{-1} temperature at the 100 % torque was already over hundred degrees.

At the rated values of 1000 min^{-1} and the 100 A current, the steady-state thermal model results in 126 °C for the end-winding temperature of the MM machine. The corresponding temperature for the EM structure is 104.8 °C. The developed model seems to agree well with the measured data. The corresponding load points for the 1000 min^{-1} rotating speed are shown in Fig. 4.7.

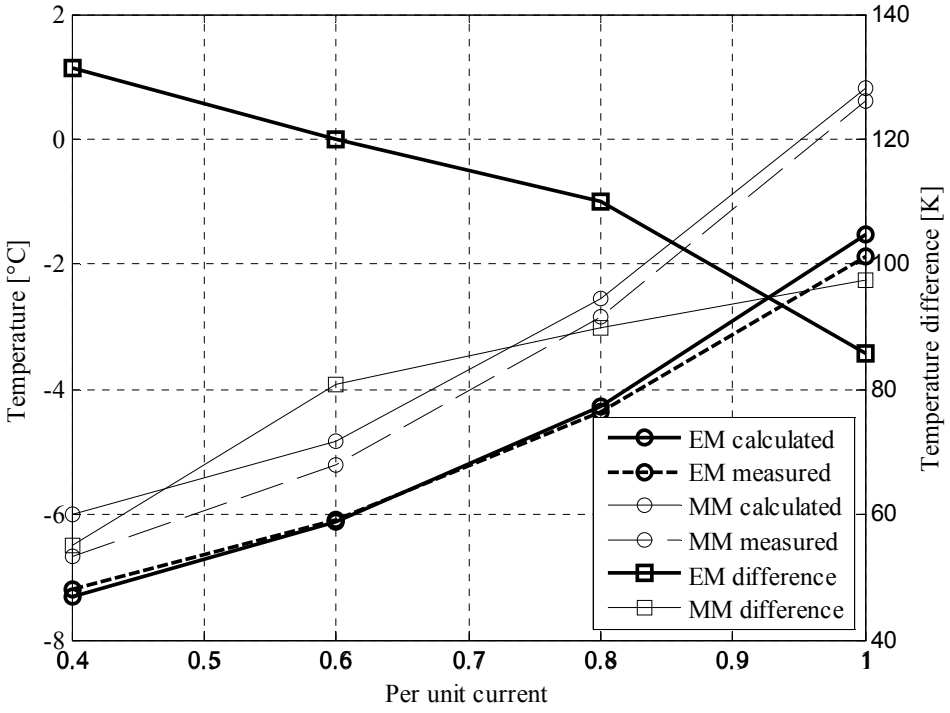

Fig. 4.7. Comparison of the measured coil temperatures and model estimates for a 1000 min^{-1} rotating speed. The secondary axis presents the temperature difference of the estimated model to the measured values.

The temperature rise characteristics of the EM machine for each constant speed in Table 4.8 follow the theory for individual rotating speeds, but the advantage of venting is evident as the rotating speed increases. The winding temperatures decrease at equivalent loading when the rotating speed increases. Increasing the rotating speed enhances the coil end convection and thereby decreases the coil end temperature. The effect is opposite in the enclosed structure because the coil end does not have direct contact to the ambient air.

4.2.2 Comparison with the dynamic model

The rated point values of Table 3.7 were selected to evaluate the dynamic model performance. The temperature rise curves are presented in Fig. 4.8.

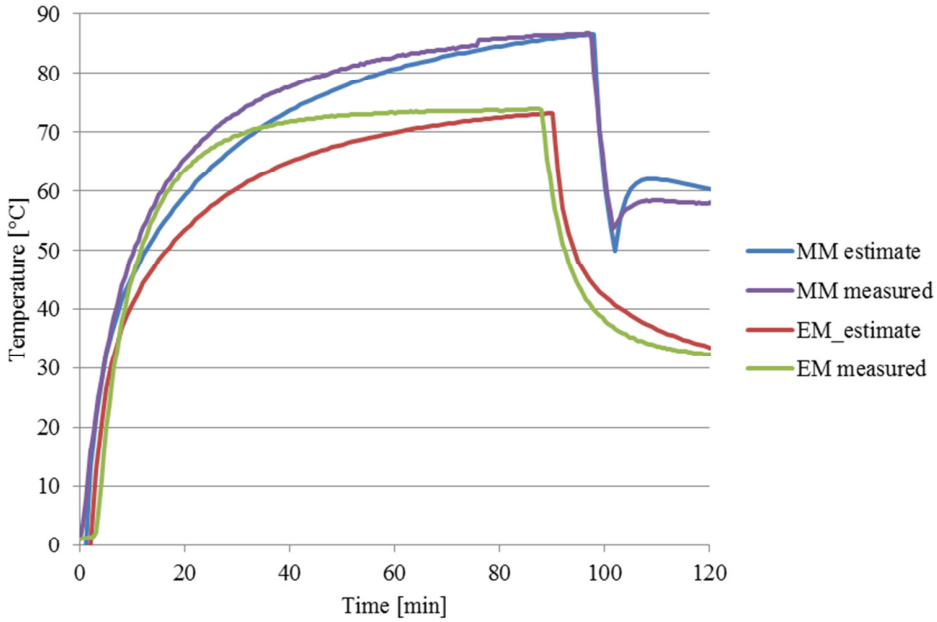

Fig. 4.8. Coil end temperature rise of the MM and EM machines as a function of time at 1000 min^{-1} and a 100 A rated current.

The developed dynamic model shows good performance for the MM machine, as shown in Fig. 4.8. According to the slope, the modelled heat capacitance seems to be large for both machines because the model temperature rise is slower compared with the measured data. The difference is more pronounced with the EM machine with the ventilated frame. The result is an indicator of the analytical model inaccuracy resulting from the selected boundary conditions and simplifications in the machine geometry. The results can be corrected to some extent by verification tests and correction coefficients, but in new machine designs, this is not possible. At best, the model is only a good estimate of the phenomenon itself.

The model was also tested to obtain actual measured race track data. The torque and rotating speed profiles from tests on the Nürnburgring Nordschleife race track are presented in Fig. 4.9.

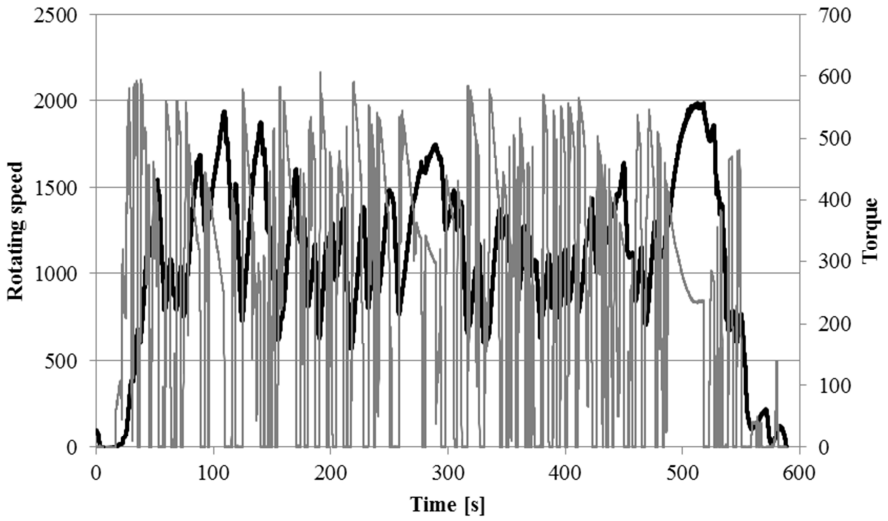

Fig. 4.9. Measured track data from the test lap on Nürbrugring Nordschleife. The rotating speed is presented in black and the torque in dark grey. The measured data are from the right rear machine with an approximately 600 Nm peak torque value.

The measured track data were used as a feed signal for the dynamic thermal model to estimate the temperature behaviour of the EM machine in track conditions. The rotating speed, supply current and cooling fluid temperatures were taken into account in the simulation. The estimated coil temperature profile of a single lap on the Nürburgring Nordschleife track is presented in Fig. 4.10 together with the measured coil temperature.

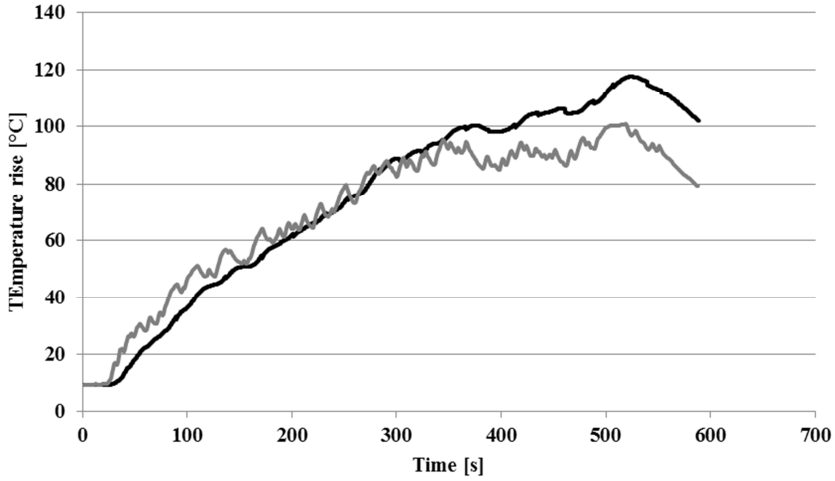

Fig. 4.10. Measured (black) and estimated (gray) coil temperature in a single lap measurement on Nürburgring Nordschleife.

The simulation model shows good agreement with the measured coil temperature even though the ambient temperature and convective cooling effects of the moving vehicle could not be replicated in the simulation procedure. The model starts to deviate from the track data around 350 second point. It is possible that the modelled air gap convection coefficient is overestimated at high rotating speed values, which causes the model to cool more efficiently.

4.2.3 Estimation of the magnet temperature

The increasing rotating speed causes increasing core losses and additional stray load losses in the machine, especially in the rotor, which cause degradation of the magnet polarization, that is, reversible demagnetization of the magnet. The measured back EMF of the EM machine is 154.3 V and respectively, 135.4 V for the MM machine at the 25 °C temperature. The corresponding values for the back EMF in different load conditions were measured between the changes in the machine load. According to these data, the magnet temperature can be estimated, because the magnet remanent flux density decreases by about 0.11 % for every Kelvin degree as the magnet temperature rises. The estimated magnet temperatures are presented in Tables 4.9 and 4.10, and correspondingly, in Figs. 4.11 and 4.12.

Table. 4.9. Estimated magnet temperatures [°C] of the MM machine according to the back EMF measurement.

min^{-1}	**0.4I_n**	**0.6I_n**	**0.8I_n**	**I_n**
1500	67	78	89	-
1000	59	66	78	94
700	51	57	66	77
300	37	40	49	66

Table. 4.10. Estimated magnet temperatures [°C] of the EM machine according to the back EMF measurement.

min^{-1}	**0.4I_n**	**0.6I_n**	**0.8I_n**	**I_n**
2000	60	64	71	80
1500	53	57	62	72
1000	49	52	59	69
700	42	46	54	65
300	33.19	42.04	45.66	54.02

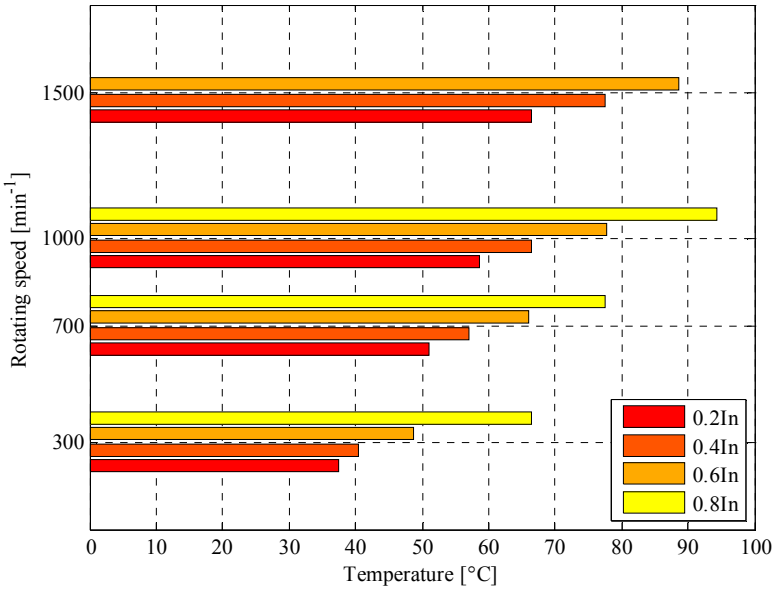

Fig. 4.11. Magnet temperature values based on Table 4.9 for the MM machine.

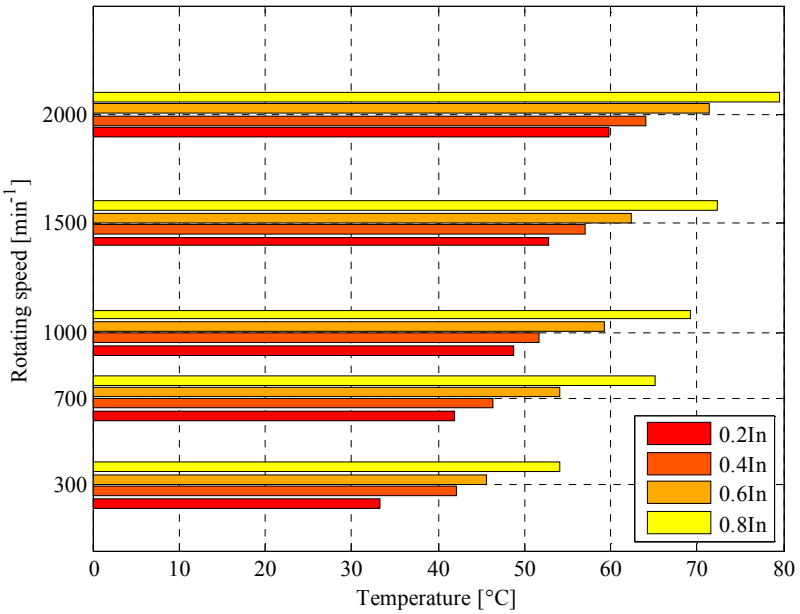

Fig. 4.12. Magnet temperature values based on Table 4.10 for the EM machine.

When comparing with the rated-value operation at 1000 min^{-1} and the 100 A current, the static thermal model shows good agreement with the estimated magnet temperatures. The temperature model gives 91.2 °C for the magnet temperature of the MM machine. On the other hand, the magnet temperature of the EM machine is 86 °C, which is slightly too high when compared with the 69 °C value in Table 4.10. It seems that the convection from the rotor shaft sleeve should be taken into account because the structure in question has a large convection surface area to the machine inner air. The enclosed structure does not gain any significant benefit from the axle sleeve modelling, because the machine inner air is considerably higher compared with the through-ventilated structure. The shaft of the EM machine is shown in Fig. 4.13.

Fig. 4.13. Rotor shaft of the EM machine.

4.2.4 Cooling efficiency

The radiator inlet and outlet temperatures were also measured with two separate PT-100 elements, and the heat removed by the cooling system was calculated for the measured water flow of 120 g per second. Heat removal in the equivalent load points and rotating speeds is presented in Tables 4.11 and 4.12.

Table. 4.11. Radiator heat removal rate for the MM machine in [W].

min^{-1}	**0.4I_n**	**0.6I_n**	**0.8I_n**	**I_n**
1500	542	612	726	X
1000	424	498	598	750
700	372	424	536	688
300	276	360	484	650

Table. 4.12. Radiator heat removal rate for the EM machine in [W].

min^{-1}	**0.4I_n**	**0.6I_n**	**0.8I_n**	**I_n**
2000	292	310	350	378
1500	258	266	298	358
1000	244	248	274	286
700	236	242	276	364
300	186	214	244	298

Compared with the totally enclosed structure of the MM machine, the heat removal through water in the EM machine cooling is considerably lower. This could be anticipated because the heat exchange rate is dependent on the temperature difference. Because of the vented structure, the stator stack temperature is lower than in the totally enclosed MM machine. The majority of the heat exits the machine structure through the venting. The heat removal is still considerable compared with the total heat production of the machines. The water heat removal rate compared with the total losses is presented in Tables 4.13 and 4.14.

Table. 4.13. Ratio of water cooling heat removal to the total losses of the MM machine.

min^{-1}	**0.4I_n**	**0.6I_n**	**0.8I_n**	**I_n**
1500	0.44	0.45	0.41	-
1000	0.51	0.44	0.41	0.38
700	0.55	0.46	0.41	0.38
300	0.84	0.59	0.51	0.44

Table. 4.14. Ratio of water cooling heat removal to the total losses of the EM machine.

$\mathbf{min^{-1}}$	$\mathbf{0.4}I_n$	$\mathbf{0.6}I_n$	$\mathbf{0.8}I_n$	I_n
2000	0.58	0.27	0.21	0.11
1500	0.54	0.28	0.19	0.16
1000	0.62	0.34	0.24	0.15
700	0.68	0.46	0.32	0.25
300	0.83	0.51	0.27	0.22

The measuring accuracy of the torque meter is 0.1 % of the measuring range, which means that the error margin is 2 Nm. The offset is high, and there is thus a certain error in the measured value, but still, the values are comparable with other measured values because the other point also includes the same error. The magnitude of the measured values can be kept correct. Keeping this in mind, the effect of the water cooling is undisputed in the MM machine construction. In the low-speed area and moderate power ratings, the majority of losses are removed by water, but the cooling efficiency of water seems to decrease quite dramatically as the loading increases. The situation is better in the EM machine where the majority of losses are removed by convection through the venting holes of the machine. According to the measurements, the decrease in the water cooling efficiency seems to be quite linear if the 300 min^{-1} speed is ignored.

4.3 Conclusions

According to the tests, there are no significant differences in the machine performance of the two machine types studied. The analytical and finite-element-based modelling seems to agree with the measured performance data when considering operation at rated torque values. The measured peak torques could not be achieved with the test set-up. One possible reason is related to the control of the machine. The control method is not capable of producing a correct current angle for high torque operation. However, the test results show that the lack of back EMF voltage in the MM machine results in a lower performance compared with the EM machine. The difference is highest in the peak torque production.

The temperature measurements show good agreement with the developed lumped-parameter thermal model. Further development of the model is needed for the through-ventilated structure as the magnet temperature estimates are high compared with the estimates for the measured decrease in the back EMF.

The dynamic model also agrees well with the measured data, but the thermal capacitance values are too high. A more accurate model of the geometry could solve this problem.

To sum up, the machine performance is at the estimated level with the embedded magnet structure. This would also apply to the magnet module design with corrected rotor dimensions that are due to the permanent magnet end effect. However, the mechanics of the magnet module has to be developed further. The comparison still shows the benefit of the through-ventilated structure over the totally enclosed machine. It would be advisable to consider through-ventilated structures in mobile applications for a higher performance if suitable protection against ambient conditions could be arranged.

Further testing by Metropolia has shown good results of the EM machine performance in the field weakening region resulting in several speed records on track and ice. Among the most significant achievements is the 17.03.2012 electric vehicle speed record of 252.09 km/h on ice, which means over 50 % field weakening of permanent magnet polarization on fully charged batteries.

5 Conclusions

This thesis presents a study on the permanent magnet traction machine design for a performance-oriented vehicle application with a four-wheel drive. The study provides two different approaches to produce a light-weight machine structure with increased saliency for enhanced torque production and field weakening characteristics: A traditional embedded magnet machine design with inherent saliency and a special magnet module design to increase the machine saliency are introduced.

5.1 Contributions of the doctoral thesis

According to the thermal analysis carried out for the structures, the implemented design methods resulted in two functional machine configurations. Both of the introduced concepts show an increased torque output capability as a result of the increased saliency.

The magnet module design seems to suffer from mechanical problems in the magnet fixing. Thus, the embedded machine structure is a more favourable solution because of its better mechanical stability. Furthermore, the through-ventilated structure shows benefits in cooling, and this should be considered in mobile applications as traditional ICE solutions have also to be protected against the environment. A through-ventilated structure provides higher steady state load capability and the lower temperature rise time constants allow a better dynamic performance.

Because a traction application does not necessarily have a specific operating point, the traditional guidelines for machine design cannot be directly applied to a traction machine design. Thus, the balance between the electromagnetic design (including design limitations related to energy source selection), heat transfer and loss generation becomes more important, especially in Joule-loss-dominated machine structures as presented in the doctoral thesis.

According to the simulations, a performance analysis by individual two-axis model inductances is only indicative for these machine types. A comparison between the finite element method and the analytical approach shows the weakness of a traditional analytical model, which does not take into account the armature reaction accurately enough because the direct- and quadrature-axis inductances obtained from the Flux 2D calculation for the d- and q-axes individually do not correctly describe the magnetic state of the machine.

An extended finite-element-based approach is needed to analyse the cross magnetization effect on the machine performance in order to fully exploit the torque output potential. Nevertheless, an analytical approach is efficient in the basic dimensioning and prediction of the physical behaviour as shown in the simple tool development carried out for the slot and tooth dimensioning to evaluate the heat transfer efficiency in the stator stack.

According to the tests, there are no significant differences in the performances between these two machines. The analytical and finite-element-based modelling seems to agree with the measured performance data when considering operation at rated torque values. However, the test results

show that the lack of back EMF voltage in the magnet module (MM) machine results in a lower performance compared with the EM machine. In addition, the welded steel band generates significant losses, which clearly reduces the overall efficiency of the MM structure.

The temperature measurements also show good agreement with the developed lumped-parameter thermal model. Further development of the model is needed for the through-ventilated structure, because the magnet temperature estimates are high compared with the modelled values including the decrease in the back EMF. The dynamic model also agrees well with the measured data, but the thermal capacitance values are too high resulting in a deviation in low transients.

The estimated peak torques could not be achieved with the test set-up. This is possibly related to the control of the machine. The control method is not capable of producing a correct current angle for high torque operation. Additional tests by Metropolia have shown good results of the field weakening capability resulting in several speed records on various tracks.

5.2 Prospects of the future work

At least the following topics of further study have been identified in the course of the doctoral work:

- Determination of optimum magnetic circuit dimensions considering the utilization of voltage reserve in torque production.
- Effect of variation in the supply voltage level on the selection of the nominal point.
- Development of an analytical lumped-parameter model for the optimization of machine heat removal.
- Development of an analytical cross-magnetization model for the fast evaluation of machine parameters.
- Development of magnet pole fixing methods in the magnet module design.

References

(Altairnano, 2009) Altairnano, 2009, *Altairnano 50Ah battery cell technical paper*, [Online], [Accessed 10 June 2012], Available from www.altairnano.com.

(Arkadan et al., 2007) Arkadan, A.A., Al-Aawar, N. and Hanbali, A.A., "Design Optimization of SynRM Drives for HEV Power Train Applications," In *IEEE international Conference on Electric Machines and Drives*, Vol. 1., 2007, pp. 810–814.

(Barcaro et al., 2008) Barcaro M., Bianchi, N. and Magnussen F., "PM motors for hybrid electric vehicles," In *Universities Power Engineering Conference*, 2008, pp. 1–5.

(Becker et al., 1962) Becker, K. M. and Kaye, J., 1962, "Measurements of Diabatic flow in annulus with inner rotating cylinder," *Journal of Heat Transfer*, no 84, pp. 97–105.

(Boglietti et al., 1991) Boglietti A., Ferraris P., Lazzari M. and Profumo F., "Iron losses in magnetic materials with six-step and PWM inverter supply," *IEEE Transactions on Magnetics*, Vol. 27, Iss. 6, 1991, pp. 5334–5336.

(Boglietti et al., 1993) Boglietti A., Ferraris P., Lazzari M. and Profumo F., "Effects of different modulation index on the iron losses in soft magnetic materials supplied by PWM inverter," *IEEE Transactions on Magnetics*, Vol. 29, Iss. 6, 1993, pp. 3234–3236.

(Boglietti et al., 1995) Boglietti A., Ferraris P., Lazzari M. and Pastorelli M., "Change of the iron losses with the switching supply frequency in soft magnetic materials supplied by PWM inverter," *IEEE Transactions on Magnetics*, Vol. 31, Iss. 6, 1995, pp. 4250–4252.

(Boglietti et al., 2003) Boglietti A., Cavagnino.A, Lazzari M. and Pastorelli M., "Predicting iron losses in soft magnetic materials with arbitrary voltage supply: An engineering approach," *IEEE Transactions on Magnetics*, Vol. 39, Iss. 2, 2003, pp. 981–989.

(Caricchi et al., 1994) Caricchi, F., Crescimbini, F., Fedeli, E. and Noioa, G., "Design and construction of a wheel-directly-coupled axial-flux PM motor prototype for EVs," In *IEEE Industry Applications Society Annual Meeting*, Vol. 1, 1994, pp. 254–261.

(Chan, 1996) Chan, C.C. and Chau, K.T., "An advanced permanent magnet motor drive system for battery-powered electric vehicles," *Transactions on Vehicular Technology*, Vol. 45 , Iss. 1, 1996, pp. 180–188.

(Chau et al., 2008) Chau, K.T. Chan, C.C. and Liu C., "Overview of Permanent-Magnet Brushless Drives for Electric and Hybrid Electric Vehicles," *Transactions on Industrial Electronics,* Vol. 55., Iss. 6, 2008, pp. 2246–2257.

(Cvetkovski et al., 2006) Cvetkovski, G., Petkovska, L. and Gair, S., "Torque analysis of axial field PM synchronous motor for EV," In *International Symposium on Power Electronics, Electric Drives, Automation and Motion*, 2006, pp. 214–217.

(Eckermann, 2001) Eckermann E., 2001, *World History of the Automobile*, Society of Automotive Engineers Inc. Warrendale.

(Elliot, 1993) Elliot R., 1993, *Electromagnetics: History, Theory, and Applications*, 1st ed., New Jersey: Wiley-IEEE Press.

(Faiz, 2006) Faiz, J. and Keyvani-Boroujeni B., "Optimal Design of Internal Permanent Magnet Motor for Starter/Generator of Hybrid Electric Vehicle," In *Power Electronics and Motion Control Conference*, 2006, pp. 984–990.

(Grauers, 2004) Grauers A. and Kasinathan P., "Force Density Limits in low–speed PM machines due to temperature and reactance," *IEEE Transactions on Energy Conversion*, Vol. 4, Iss. 3, September 2004, pp. 518–525.

(Heikkilä, 2002) Heikkilä, T, *Permanent magnet synchronous motor for industrial inverter appilications - analysis and design*, Acta universitatis Lappeenrantaensis No. 134, Doctoral thesis, 2002, Lappeenranta University of Technology.

(Hämäläinen, 2009) Hämäläinen H., 2009, "Skin effect and voltage stresses in PWM frequency converter driven motors," Master's thesis, Lappeenranta University of Technology.

(IEA, 2011) International Energy Agency, 2011, *Key World Energy statistics*, Technical report, [Online], [Accessed 10 June 2012], Available from www.iea.org.

(IEEE Coll., 1993) IEEE Colloquium on *Motors and Drives for battery powered Propulsion*, Digest No. 80, 1993.

(Incropera, 2007) Incropera F.P. and DeWitt D. P., 2007, *Fundamentals of Heat and Mass Transfer*, 6th ed., New York: John Wiley & Sons, Inc.

(Jung et al., 2007) Jung J-W., Hong J-P. and Kim Y-K., "Characteristic Analysis and Comparison of IPMSM for HEV According to Pole and Slot Combination," In *Vehicle Power and Propulsion Conference,* 2007, pp. 778–783.

(Jussila, 2010) Jussila H., 2010, *Concentrated Winding multiphase permanent magnet machine design and electromagnetic properties - case axial flux machine*, Acta Universitatis Lappeenrantaensis No. 374, Doctoral thesis, Lappeenranta University of Technology.

(Kylander, 1995) Kylander, G., 1995, *Thermal modeling of small cage induction motors*, Technical report No. 265, Chalmers University of Technology, Göteborg, Sweden, February 1995.

(Larminie, 2003) Larminie J. and Lowry J., 2003, *Electric Vehicle Technology Explained*, Chichester: John Wiley & Sons, Ltd.

(Lindström, 1999) Lindström J., 1999, *Thermal Model of a Permanent Magnet Motor for A Hybrid Electric Vehicle*, Technical report, Chalmers University of Technology, Göteborg, Sweden.

(Liu et al., 1993) Liu. J., Howe D., Mellor P.H. and Jenkins M.K., "Thermal analysis of permanent magnet machines," In the *Sixth International Conference on Electrical Machines and Drives*, No. 376, September 8–10, 1993, pp. 359–364.

(Mellor et al., 1991) Mellor P.H., Roberts D. and Turner D.R., "Lumped parameter thermal model for electrical machines of TEFC design," In *IEEE Proceedings B Electric power applications,* Vol. 138, Iss. 5, 1991, pp. 205–218.

(Metropolia, 2009) Helsinki Metropolia University of Applied Sciences, 2009, *Metropolia Electric Race-About media archive,* [Online], [Accessed 10 June 2012], www.raceabout.fi.

(Miller, 1994) Hendershot J.R. Jr. and Miller T.J.E., 1994, *Design of Brushless Permanent-Magnet motors*, Oxford: Magna Physics Publishing and Claredon Press.

(Neorem 493, 2008) Neorem 2008a, *Neorem magnet Ne493a data sheet,* [Online], [Accessed 10 June 2012], Available from www.neorem.fi.

(Neorem 753, 2008) Neorem 2008b, *Neorem magnet Ne753a data sheet,* [Online], [Accessed 10 June 2012], Available from www.neorem.fi.

(Nerg, et al., 2010) Nerg J., Rilla M. and Pyrhönen J., "Thermal Analysis of Radial-Flux Electrical Machines with a High Power Density," *IEEE Transactions on Industrial Electronics*, Vol. 55, Iss. 10, 2010, pp. 3543–3554.

(Neudorfer et al., 2008) Neudorfer, H., Wicker, N. and Binder A., "Comparison of Three Different Electric Powertrains for the Use in Hybrid Electric Vehicles," In *IET Conference on Power Electronics*, *Machines and Drives*, 2008, pp. 510–514.

(Ohyama et al., 2006). Ohyama K., Nashed M.N.F., Aso K., Fujii H. and Uehara H., "Design using Finite Element Analysis of Switched Reluctance Motor for Electric Vehicle," In *ICTTA*, 2006, pp. 727–732.

(Polinder et al., 1997) Polinder H. and Hoejimakers M.J., "Eddy-current losses in the permanent magnets of a PM machine," In the *Eighth International Conference on Electrical Machines and Drives*, 1997, pp. 138–142.

(Post, 2000) Post R.F. and Ryutov D.D., "The Inductrack: a simpler approach to magnetic levitation," *IEEE Transactions on Applied Superconductivity*, Vol. 10, Iss. 1, 2000, pp. 901–904.

(Profumo et al., 1997) Profumo, F., Zhang Z. and Tenconi, A., "Axial flux machines drives: a new viable solution for electric cars," *IEEE Transactions on Industrial Electronics*, Vol.44, Iss. 1, 1997, pp. 39–45.

(Pyrhönen et al., 2008) Pyrhönen J., Jokinen T. and Hrabovkova V., 2008, *Design of Rotating Electrical Machines*, Chichester: John Wiley & Sons.

(Pyrhönen et al., 2010) Pyrhönen J., Ruuskanen V., Nerg J., Puranen, J. and Jussila, H., "Permanent-Magnet Length Effects in AC Machines," *IEEE Transactions on Magnetics*, Vol. 46, Iss. 10, 2010, pp. 3783–3789.

(Qionghua et al., 2003) Qionghua Z., Shuanghong W., Zhiyuan M., Wei G. and Yihui Q., "Design of a 50kW Switched Reluctance Machine for HEV Propulsion System," In the *58th IEEE Conference on Vehicular Technology*, Vol. 5, October 6–9, pp. 3207–3211.

(Ramamurthy, 2001) Ramamurthy S.S. and Balda J.C., "Sizing a Switched Reluctance Motor for electric vehicles," *IEEE Transactions on Industry Applications*, Vol. 37, Iss. 5, 2001, pp. 1256–1264.

(Richter, 1962) Richter R., 1962, *Elektrische Maschinen: Synchronmaschinen und Einankerumformer* (Electrical machines: Synchronous machines and Rotary Converters) II, Basle and Stuttgart: Birkhäuser Verlag.

(Rilla, 2006) Rilla M,, 2006, “Thermal modelling of permanent magnet synchronous machine”, Master’s thesis, Lappeenranta university of Technology.

(Rooks, 2004) Rooks J.A. and Wallace A.K. (2004), “Energy efficiency of VSDs,” *IEEE Industry Applications Magazin*e 10, pp. 57–61.

(Ruotsalainen, 2012) Ruotsalainen S., 2012, *Ajoneuvojen ja työkoneiden voimansiirron kehittäminen*, [Development of vehicle and working machine transmission], Final report (in Finnish), Helsinki Metropolia University of Applied Sciences.

(Russenschuck, 2010) Russenschuck S., 2010, *Field computation for Accelerator Magnets*, Weinheim: Wiley-VCH Verlag GmbH & Co. KGaA.

(Saari, 1995) Saari J., 1995, *Thermal Modelling of High speed induction machines*, Acta Polytechnica Scandinavica, Electrical Engineering series No. 82, Espoo.

(SKF, 2012) SKF, 2012, [Online], [Accessed 10 October 2012], Available from www.skf.com

(Shidore et al., 2007) Shidore, N., Bohn, T., Duoba, M., Lohse-Busch, H. and Sharer, P., "PHEV 'all-electric range' and fuel economy in charge-sustaining mode for low SOC operation of the JCS VL41 M Li-ion battery using battery HIL," In the *23rd International Electric Vehicle Symposium (EVS23)*, Anaheim, CA, Dec. 2007.

(Staton et al., 2005) Staton, D., Boglietti, A. and Cavagnino, A. “Solving the More Difficult Aspects of Electric Motor Thermal Analysis in Small and Medium Size Industrial Induction Motors,” *IEEE Transactions on Energy Conversion*, Vol. 20, Iss. 3, 2005, pp. 620–628

(Steinmetz, 1984) Steinmetz C.P., “On the Law of Hysteresis,” In *IEEE proceedings*, Vol. 72, Iss. 2, 1984, pp. 197–221.

(Stumberger et al., 2003) Stumberger, B., Stumberger, G., Dolinar, D., Hamler, A. and Trlep, M., “Evaluation of saturation and cross-magnetization effects in interior permanent-magnet synchronous motor,” *IEEE Transactions on Industry Applications*, Vol. 39., Iss. 5., 2003, pp.1264–1271.

(TRB, 2006) Transportation Research Board of the National Academies, “Tires and Passenger Vehicle Fuel Economy”, Special report 286, USA, 2006.

(Tutkun, 2002) Tutkun N. and Moses A.J., "Measurement of power loss distribution in a typical stator core under PWM voltage excitation," *Journal of Magnetism and Magnetic Materials*, No. 262, 2002, pp. 230–234.

(Vogt, 1983) Vogt K., 1983, *Elektrische Maschinen. Berechnung rotierender elektrischer Maschinen* (Electrical machines. Design of rotating electrical machines), 3rd edition, Berlin: VEB Verlag GmbH.

(Watanabe et al., 2007) Watanabe, K., Kawasaki, Aida, S., Komatsuzaki, A. and Miki, I., "Driving force characteristics of 40kW switched reluctance motor for electric vehicle," In *ICEMS*, 2007, pp. 1894–1898.

(WEG, 2009) Technical guide – Induction motors fed by PWM frequency inverters, [Online], [Accessed 10 June 2012], Available from www.weg.net.

(Wu et al., 2002) Wu W., Dunlop J.B. and Collocott S.J., "Design optimization of switched reluctance motor by electromagnetic and thermal finite element analysis," In *INTERMAG, GS-01*, 2003.

(Xia, 1998) Xia, W. and Chin, P., "A Specially Designed EV PM Motor Drive," In *Proceedings of Energy management and Power Delivery*, Vol. 2., 1998, pp. 718–722.

(Xingming et al., 2009) Xingming Z., Xuhui W., Feng Z., Tao F. and Xinhua G., "An optimal method of power parameters' matching design in DMPM based HEV," In *ICEMS*, 2009, pp. 1–6.

(Xiong et al., 2008) Xiong, W., Wu, Z. Yin, C., Chen, L., "Economical comparison of three hybrid electric car solutions," In *IEEE Vehicle Power and Propulsion Conference*, Shanghai, 3–5 September, 2008, pp.1–6.

(Zeraouila et al., 2006) Zeraouila, M., Benbouzid, M.E.H. and Diallo, D., "Electric motor drive selection issues for HEV propulsion systems: a comparative study," *IEEE Transactions on Vehicular Technology*, 2006, pp.1756–1764.

APPENDIX I: Test equipment

Magtroll TM 314 2000 Nm inline torque transducer

- combined error of linearity and hysteresis < ±0.1% of rated torque
- Temperature influence on the zero\sensitivity < ±0.1% of rated torque/10 K
- Influence of speed on the zero torque signal < ± 0.01% of rated torque /1000 min^{-1}
- Long term stability of sensitivity <± 0.05% of rated torque / year

Magtroll TM 6400 Transducer display

- Accuracy of speed measurement 0.01% of reading
- Accuracy of Torque 0.01% of range (10V)

Yokogawa Pz-4000 Power analyzer

- Temperature 23°C ±3°C
- Accuracy:

Table I. Yokogawa PZ-4000 accuracy table

Frequencies	Voltage/Current	Power
DC	±(0.2% of rdg + 0.1% of rng)	±(0.2% of rdg + 0.1% of rng)
0.1 Hz < *f* < 10 Hz	±(0.2% of rdg + 0.1% of rng)	±(0.2% of rdg + 0.05% of rng)
10 Hz < *f* < 45 Hz	±(0.2% of rdg + 0.05% of rng)	±(0.2% of rdg + 0.025% of rng)
45 Hz < *f* < 1 kHz	±(0.1% of rdg + 0.05% of rng)	±(0.1% of rdg + 0.025% of rng)
1 kHz < *f* < 10 kHz	±(0.1% of rdg + 0.05% of rng)	±(0.1% of rdg + 0.04% of rng)
10 kHz < *f* < £ 50 kHz	±(0.2% of rdg + 0.1% of rng)	±(0.2% of rdg + 0.05% of rng)
50 kHz < *f* < 100 kHz	±(0.6% of rdg + 0.2% of rng)	±(0.6% of rdg + 0.1% of rng)
100 kHz < *f* < 200 kHz	±(0.6% of rdg + 0.2% of rng)	±(1.5% of rdg + 0.15% of rng)
200 kHz < *f* < 400 kHz	±(1% of rdg + 0.2% of rng)	±(1.5% of rdg + 0.15% of rng)
400 kHz < *f* < 500 kHz	±[(0.1 + 0.006f)% of rdg +0.2% of mg]	±[(0.1 + 0.009f)% of rdg +0.15%of rng]
500 kHz < *f* < 1 MHz	±[(0.1 + 0.006 ´ f)% of rdg +2% of rng]	±[(0.1 + 0.009f)% of rdg +1.5%of rng]
1 MHz < *f* < 5 MHz	±[(0.1 + 0.006 ´ f)% of rdg +2% of rng]	–

APPENDIX II: Thermal network

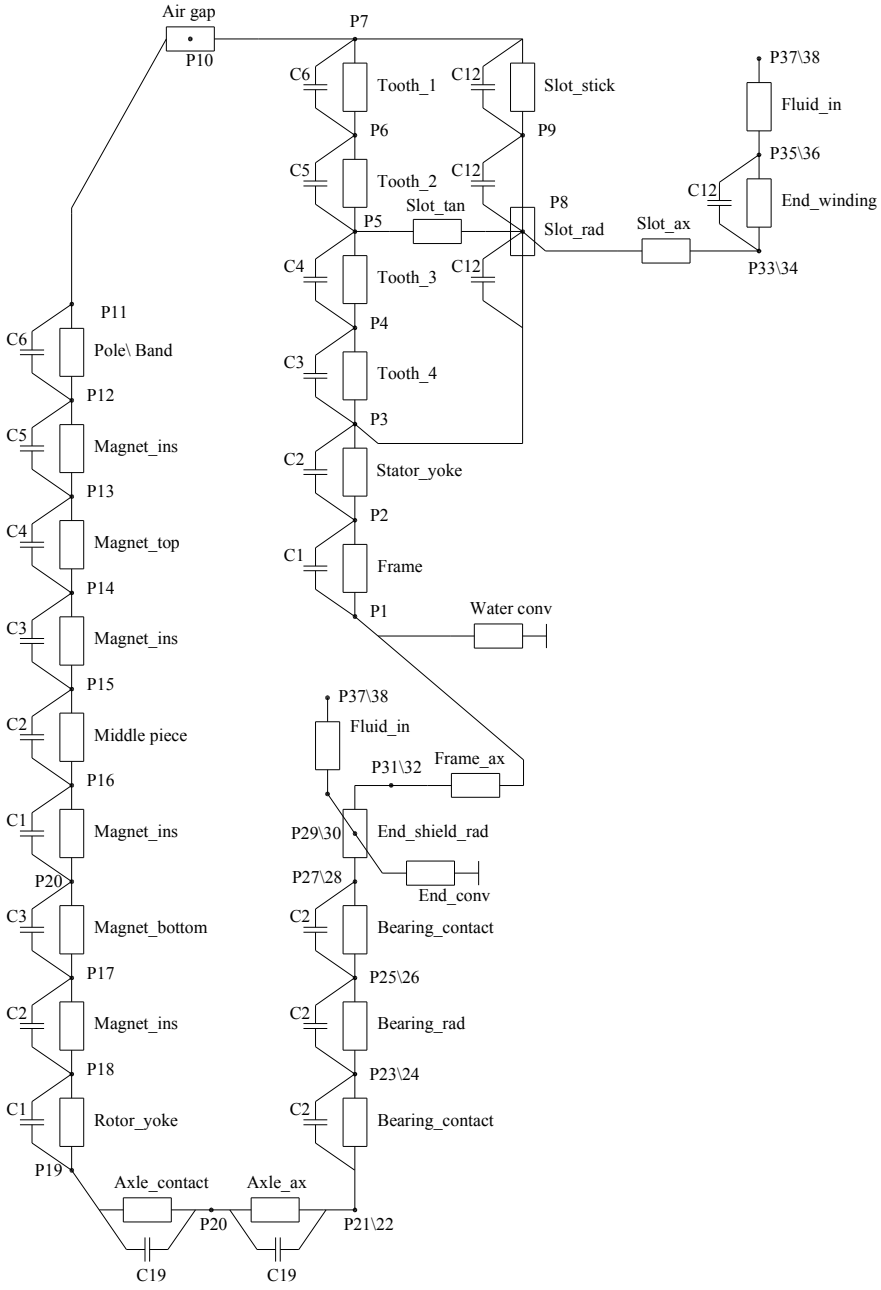

APPENDIX III: Test machine dimensions

Stator diemensions

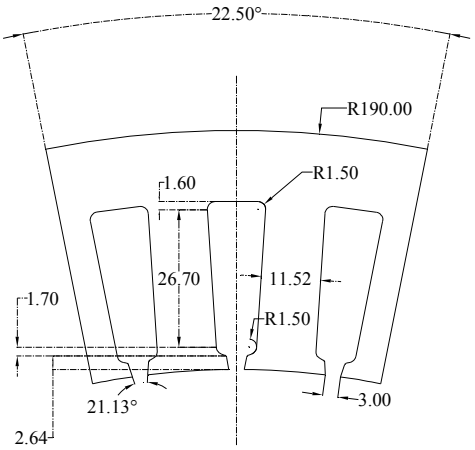

Embedded magnet (EM) dimensions

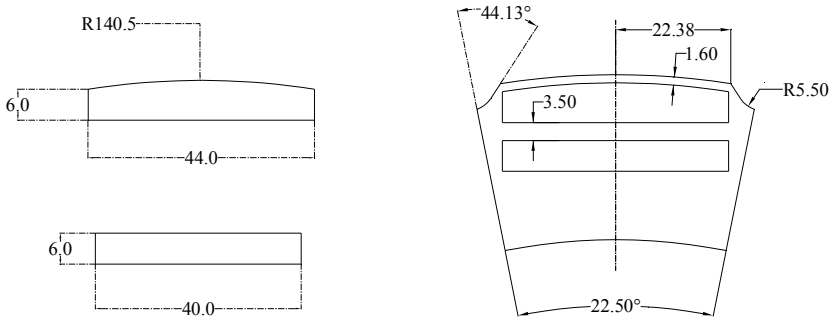

Magnet module (MM) dimensions

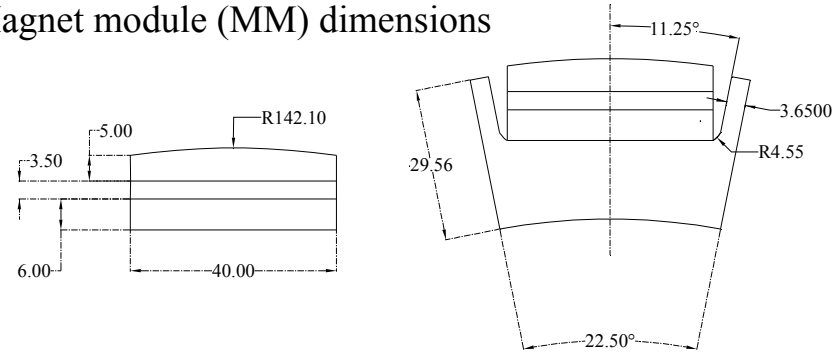

ACTA UNIVERSITATIS LAPPEENRANTAENSIS

455. HUJALA, MAIJA. Structural dynamics in global pulp and paper industry. 2011. Diss.

456. KARVONEN, MATTI. Convergence in industry evolution. 2011. Diss.

457. KINNUNEN, TEEMU .Bag-of-features approach to unsupervised visual object categorisation. 2011. Diss.

458. RUUSKANEN, VESA. Design aspects of megawatt-range direct-driven permanent magnet wind generators. 2011. Diss.

459. WINTER, SUSANNA. Network effects: scale development and implications for new product performance. 2011. Diss.

460. JÄÄSKELÄINEN, ANSSI. Integrating user experience into early phases of software development. 2011. Diss.

461. KÄÄRIÄINEN, TOMMI. Polymer surface modification by atomic layer deposition. 2011. Diss.

462. KOCHURA, ALEKSEY. Growth, magnetic and transport properties of InSb and II-IV-As2 semiconductors doped with manganese. 2011. Diss.

463. PUTKIRANTA, ANTERO. Possibilities and challenges of longitudinal studies in operations management. 2011. Diss.

464. HAPPONEN, ARI. Muuttuvaan kysyntään sopeutuva varastonohjausmalli. 2011. Diss.

465. VASAVA, PARITOSH. Application of computational fluid dynamics in modelling blood flow in human thoracic aorta. 2011. Diss.

466. PURO, LIISA. Identification of extractives and polysaccharides as foulants in membrane filtration of pulp and paper mill effluents. 2011. Diss.

467. LAPPALAINEN, PIA. Socially Competent Leadership – predictors, impacts and skilling in engineering. 2012. Diss.

468. PLAMTHOTTATHIL, ANSHY OONNITTAN. Application of electrokinetic Fenton process for the remediation of soil contaminated with HCB. 2012. Diss.

469. EBRAHIMI, FATEMEH. Synthesis of percarboxylic acids in microreactor. 2012. Diss.

470. JANTUNEN, SAMI. Making sense of software product requirements. 2012. Diss.

471. VILKO, JYRI. Approaches to supply chain risk management: identification, analysis and control. 2012. Diss.

472. TANSKANEN, VESA. CFD modelling of direct contact condensation in suppression pools by applying condensation models of separated flow. 2012. Diss.

473. HUHTANEN MIKKO. Software for design of experiments and response modelling of cake filtration applications. 2012. Diss.

474. PARJANEN, SATU. Creating possibilities for collective creativity
Brokerage functions in practice-based innovation. 2012. Diss.

475. KUKKONEN, SAKU. Generalized differential evolution for global multi-objective optimization with constraints. 2012. Diss.

476. LAAKSONEN, JONNA. Tactile-proprioceptive robotic grasping. 2012. Diss.

477. KALLIO, ANNE. Enhancing absorptive capacity in a non-research and development context An action research approach to converting individual observations into organizational awareness. 2012. Diss.

478. LÄTTILÄ, LAURI. Improving transportation and warehousing efficiency with simulation based decision support systems. 2012. Diss.

479. OYOMNO, WERE. Usable privacy preservation in mobile electronic personality. 2012. Diss.

480. LINNALA, MIKKO. Simulation and optimization tools in paper machine concept design. 2012. Diss.

481. KORPIJÄRVI, JUHA. Aging based maintenance and reinvestment scheduling of electric distribution network. 2012. Diss.

482. KORHONEN, JUHAMATTI. Active inverter output filtering methods. 2012. Diss.

483. KLODOWSKI, ADAM. Flexible multibody approach in bone strain estimation during physical activity: quantifying osteogenic potential. 2012. Diss.

484. VUORENMAA, MARKKU. Osaamisen johtaminen pk-yrityksen kansainvälisen kasvun elinkaarella. 2012. Diss.

485. RAUTIAINEN, MARITA. Dynamic ownership in family business systems – a portfolio business approach. 2012. Diss.

486. LILIUS, REIJO. THE FINNISH IT INDUSTRIES IN TRANSITION Defining and measuring the Finnish software product and IT services industries by applying theoretical frameworks . 2012. Diss.

487. TUOMINEN, PASI. The purpose of consumer co-operation: implications for the management and governance of co-operatives. 2012. Diss.

488. SAARI, ESA. Suurnopeus-turbokoneroottoreiden termodynaaminen ja mekaaninen mallinnus sekä rakenneanalyysi. 2012. Diss.

489. PAANANEN, MIKKO. On innovative search: the use of internal and external sources of innovation among Finnish innovators. 2012. Diss.

490. BELOVA, POLINA. Quasiclassical approach to the vortex state in iron-based superconductors. 2012. Diss.

491. HIETANEN, IIRO. Design and characterization of large area position sensitive radiation detectors. 2012. Diss.

492. PÄSSILÄ, ANNE. A reflexive model of research-based theatre Processing innovation of the cross-road of theatre, reflection and practice-based innovation activities. 2012. Diss.

493. RIIPINEN, TOMI. Modeling and control of the power conversion unit in a solid oxide fuel cell environment. 2012. Diss.

494. RANTALAINEN, TUOMAS. Simulation of structural stress history based on dynamic analysis. 2012. Diss.

495. SALMIMIES, RIINA. Acidic dissolution of iron oxides and regeneration of a ceramic filter medium. 2012. Diss.

496. VAUTERIN, JOHANNA JULIA. The demand for global student talent: Capitalizing on the value of university-industry collaboration. 2012. Diss.